Flow visualization and force measurements on a flapping-wing MAV DelFly II in forward flight configuration

Jerke Eisma B.Sc.

16-05-2012

Faculty of Aerospace Engineering · Delft University of Technology

TUDelft

Flow visualization and force measurements on a flapping-wing MAV DelFly II in forward flight configuration

MASTER OF SCIENCE THESIS

FOR OBTAINING THE DEGREE OF MASTER OF SCIENCE IN AEROSPACE ENGINEERING AT DELFT UNIVERSITY OF TECHNOLOGY

H.E. EISMA

16-05-2012

FACULTY OF AEROSPACE ENGINEERING - DELFT UNIVERSITY OF TECHNOLOGY

TU Delft
Delft
University of
Technology

Delft University Of Technology
Department Of
Aerodynamics

The undersigned hereby certify that they have read and recommend to the Faculty of Aerospace Engineering for acceptance a thesis entitled **"Flow visualization and force measurements on a flapping-wing MAV DelFly II in forward flight configuration"** by **Jerke Eisma** in partial fulfillment of the requirements for the degree of **Master of Science**.

Dated: <u>16-05-2012</u>

Committee chairman:

Prof. dr. F. Scarano

Supervisor 1:

Dr. ir. B.W. van Oudheusden

Supervisor 2 :

M. Percin, MSc.

Reader:

Ir. B.D.W. Remes

Summary

Flapping wing flight has attracted increased interest among aerodynamics researchers recently in view of the recent expansion of design efforts in the field of Micro Aerial Vehicles (MAVs). MAVs are given specific attention because of their potential as mobile platforms capable of reconnaissance and gathering intelligence in hazardous and physically inaccessable areas. To achieve these missions, they should be manoevring with ease, staying aloft and propelling themselves efficiently. Conventional means of aerodynamic force generation are found lacking at this point and the flapping-wing approach becomes an appealing or even necessary solution. In contrast to the conventional (fixed and rotary wing) force generation mechanisms, flapping wing systems take benefit from the unsteady flow effects that are associated to the vortices separating from the wing leading and trailing edges, which create low pressure regions around the wings that lead to the generation of higher lift and thrust.

DelFly II, which is the subject of investigation for the current research, is a bio-inspired flapping wing MAV designed and built at Delft University of Technology. The DelFly has a bi-plane wing configuration with wings which consist of Mylar foil, reinforced with carbon rods. The DelFly has a total wing span of 280 mm, and weighs 17 g. A custom made brushless motor with a motor controller, a gear system and a crank shaft mechanism are used to drive the wings in flapping motion. A conventional cross-tail is used in order to guarantee stability and controllability. It can hover as well as fly in forward and backward direction. An essential part of the DelFly MAV system is that it is equipped with a miniature onboard camera, not only for observational purposes but also for making autonomous flight possible by use of the image analysis software in the ground station.

It is clear that the wake structure of the flapping wings requires a detailed investigation, particularly for the DelFly case which has a tail that is also interacting with the wake structures of the wings. Therefore, additionally to the general characterization of the time-dependent flapping-wing wake structure, the interaction between the flapping-wing wake and the tail for different tail positions and angles of attack is a further particular point of interest in the investigation.

The present research consists of two parts. The wake topology of the DelFly is researched by means of a time resolved stereoscopic Particle Image Velocimetry (PIV) setup. Furthermore, simultaneous force measurements are performed with compact six-component force balance. A full scale DelFly model is placed in the low speed W-tunnel at the Aerodynamics Laboratory of Delft University of Technology. PIV measurements are performed in planes perpendicular to the free stream flow at different downstream locations. The force and PIV measurements are synchronized by means of an additional reference signal that is logged together with the force data. Three-dimensional measurement volumes are reconstructed by taking images from the subsequent measurement plane. Kriging is applied to interpolate between the measurement planes. First of all, the general wake topology of the DelFly is presented. Furthermore, the influence of different experimental parameters is researched. The influence of the flapping frequency, free stream velocity and angle of attack are shown in this research.

Force results are presented at different flight configurations. The reconstructed wake topology of the DelFly shows the generation of tip vortices during both instroke and outstroke. Furthermore, trailing edge vorticity is seen to develop over the span of the wing during the instroke. During instroke, a very clear U-shaped structure consisting of root vortices, trailing edge vortices and tip vortices appears on both wings. To a lesser extent, trailing edge vorticity is generated on the outer parts of the wing during the outstroke. This is a result of the clap-and-fling mechanism.

The frequency is shown to have a big influence on the wake topology especially during the outstroke phase. When flapping at 12 Hz, a vertical vortical connection between the tip vortices from both wings appears during this phase. This is most probably due to the increased strength of the tip vortices. Increasing the free stream velocity shows earlier and faster shedding of the vortical structures compared to the lower free stream velocity case. Furthermore, less coherency in the vortical structures is observed at higher free stream velocities. Varying the angle of attack of the DelFly, leading edge vortices are shed from the top wing. The results suggest that due to an increased geometrical angle of attack of the top wing, vortical structures appear to be stronger on the top wing. In all other cases, no shedding of leading edge vorticity is observed. Most probably, the shed leading edge vortices during stroke reversal are convected downstream outside the measurement volume.

Preface

After six years of study I have completed my study with my Master thesis. It is the final step for obtaining my Master's degree in Aerospace Engineering at Delft University of Technology. The thesis reflects the taught subjects during the last 5 years. I would like the thank a number of people that supported me with great help during my thesis. Without their help I would not have been able to complete the project as it is right now.

First of all I do like to thank Mustafa Percin for his enthusiastic daily support. Throughout my thesis I have worked with him with a great pleasure. We had great discussions during the last few months. You always motivated me to go for the best results possible. Also Bas van Oudheusden ho guided me as supervisor during the project. His valuable comments and advises throughout the project were of great help.

Furthermore, Bart Remes, Christophe de Wagter and Rick Ruijsink provided a lot of help in making the experimental setup working. Their knowledge on very small electronics was of invaluable importance to make this thesis a succes. I also want thank Nico, Frits, Eric and Peter for the helping with practical problems regarding either software or hardware during the complete thesis.

I also want to express my appreciation to Dirk Jan Boon and Jouke de Baar. Their expertise in the field of kriging was of great importance to the succes of this study. Furthermore, the frequent ping-pong moments or the wonderful playings at the organs of the old church in Delft with Dirk Jan were wonderful. I am very grateful to my family. Even without exact knowledge on the subject they always motivated me to bring this thesis to a good end. Finally, I want to express my deep gratitude towards Salome. Without compromising the rest, I must say that with her continuous support I managed to do this project.

Delft, May 16, 2012

Contents

List of Tables

List of Figures

List of Symbols

Acronyms

A	MAV
AR	Aspect Ratio
ASTI	Aerospace Software and Technologies
CCD	Charged Couple Device
CMOS	Complementary Metal Oxide Semiconductor
CR	Contraction Ratio
DUT	Delft University of Technology
FOV	Field of View
GR	Gear Ratio
HSC	High Speed Controller
HSL	High Speed Laboratory
HWA	Hot Wire Anemometry
LDV	Laser Doppler Velocimetry
LEV	Leading Edge Vortex
MAV	Micro Aerial Vehicle
NI	National Instruments
PC	Poly Carbonate
PID	Proportional Integral Derivative
PIV	Particle Image Velocimetry
POM	Polyxymethylene
RMS	Root Mean Square
RPM	Rotations Per Minute $[1/min]$

SNR	Signal to Noise Ratio	
SNR	Signal to Noise Ratio	
TEV	Trailing Edge Vortex	
TTL	Transistor-transistor logic	
TV	Tip Vortex	

Greek Symbols

α	Angle in XZ plane between light ray from particle passing through lens center of a camera and the Z-axis	$[deg]$
α	Angle of attack of DelFly	$[deg]$
δ	Boundary layer thickness	$[mm]$
ϵ	Mean noise	$[-]$
Γ	Circulation	$[m^2/s]$
λ	Wave length	$[nm]$
μ	Viscosity	$[kg/ms]$
ω	Vorticity	$[1/s]$
ω	Wing stroke amplitude	$[deg]$
ϕ	Angle of leading edges of DelFly wings w.r.t. horizontal axis	$[deg]$
ρ	Density	$[kg/m^3]$
ρ	Distance from origin to line in Hough space	$[-]$
σ	Standard deviation	$[-]$
θ	Angle between line and horizontal axis in Hough space	$[deg]$
θ_d	Correlation length	$[-]$

Latin Symbols

$\bar{c}$	mean chord length	$[mm]$
$\bar{u}$	Flow non-uniformity	$[-]$
C_{pe}	Pressure coefficient at exit of contraction	$[-]$
C_{pi}	Pressure coefficient at inlet of contraction	$[-]$
C_p	Pressure coefficient	$[-]$
com	Center of mass	$[-]$
D	Aperture diameter	$[mm]$
d_i	Image size	$[mm]$
d_o	Object size	$[mm]$
d_p	Effective particle diameter	$[\mu m]$
D_X	Particle displacement in x-direction	$[m]$
D_Y	Particle displacement in y-direction	$[m]$

D_Z	Particle displacement in z-direction	$[m]$
d_{diff}	Diffraction diameter	$[\mu m]$
D_{eq}	Equivalent diameter for rectangular cross section	$[m]$
d_{geom}	Geometric particle diameter	$[\mu m]$
f	Focal length of a lens	$[mm]$
$f_\#$	Aperture number	$[-]$
$h_{ij,d}$	Spatial separation between two observed locations	$[-]$
u	Velocity component in x-direction	$[m/s]$
u'	velocity fluctuations	$[m/s]$
v	Velocity component in y-direction	$[m/s]$
w	Velocity component in z-direction	$[m/s]$
X	Ratio of axial coordinate over contraction length	$[-]$
x	Axial coordinate in contraction	$[m]$
x_0	Distance from the last turbulence screen to the inlet of contraction	$[m]$
x_i	Distance from contraction inlet to wall pressure maximum	$[m]$
H	Observation matrix	$[-]$
K	Gain matrix	$[-]$
P	Covariance matrix	$[-]$
R	Observation error covariance matrix	$[-]$
A	Area	$[m^2]$
b	Wing span	$[mm]$
D	Diameter	$[m]$
I	turbulence intensity	$[-]$
J	Advance ratio	$[-]$
k	Reduced frequency	$[-]$
L	Nozzle length	$[m]$
M	Magnification factor	$[-]$
m	Ratio of inlet over exit equivalent diameter of contraction	$[-]$
n	Wing beat frequency	$[Hz]$
R	Semi-wing span	$[mm]$
Re	Reynolds number	$[-]$
S	Wing surface area	$[mm^2]$
s	Distance [-]	
St	Strouhal number	$[-]$

U	Velocity	$[m/s]$
V	Wall velocity	$[m/s]$

Subscripts

1	Camera 1	
1	Inlet plane of contraction	
2	Camera 2	
2	Exit plane of contraction	
∞	Free stream conditions	$[-]$
c	Centerline of contraction	
x	x-component	
y	y-component	
z	z-component	
b	Bottom wing	
e	Point of wall-velocity maximum	
eq	Equivalent	$[-]$
exit	Exit conditions/parameters of contraction	
i	Point of wall-velocity minimum	
in	Instroke	
inlet	Inlet conditions/parameters of contraction	
out	Outstroke	
ref	reference conditions	
t	Top wing	
tip	Tip of the wing	

Introduction

Flapping wing aerodynamics attracts the attention of the researchers recently mainly due to ever-increasing interest on the Micro Aerial Vehicles (MAVs)Micro Aereal Vehicle. MAVs are small unmanned air vehicles with overall dimensions not larger than 15 cm. MAVs are of importance since they are meant to be used for reconnaissance and gathering intelligence in hazardous and physically inaccessible areas. Therefore, they should be capable of maneuvering with ease, staying aloft and propelling themselves efficiently. At this point, conventional means of force generation become insufficient and flapping wing propulsion, which provides flying creatures unique abilities, becomes necessary. Hence, prevailing MAV designs are generally inspired from the flapping wing mechanisms of birds and insects. The DelFly, which is the matter of interest for the current project, is a bio-inspired flapping wing MAV.

The DelFlyproject started as a final project for a team of bachelor students from Delft University of Technology in 2005. During the previous years, three versions of the DelFly have been developed: the DelFly I and II and the DelFly Micro. The DelFly II is used as an experimental benchmark in the present study and from this point on the DelFly II is called as the DelFly. It has a bi-plane wing configuration (see Figure 1) with wings which consist of Mylar foil, reinforced with carbon rods. The wing span of this MAV is 280 mm, the weight is 17 g. A custom made brushless motor with a motor controller, a gear system (gear ratio 1:21.33) and a crank shaft mechanism are used to drive the wings in flapping motion. A conventional cross-tail is used in order to guarantee stability and controllability. Additionally a camera is mounted on the DelFly not only for observational purposes but also for making autonomous flight possible by use of the image analysis software in the ground station.

The flapping wing configuration that is utilized by the DelFly, i.e. clap-and-fling mechanism, has a strong relation with insect flight. The flapping wing configuration is responsible for generating lift and thrust during flight. In order to get a better insight into the clap-and fling mechanism of the DelFly, number of experimental studies were performed [1, 2, 3] and the knowledge gathered was used to improve the aerodynamic performance of the DelFly.

1.1   Project goal

Understanding the aerodynamic behavior of the DelFly is an important aspect to improve the design and performance of the DelFly. Previous researches on the DelFly focused on the aerodynamic mechanisms in the vicinity of the wings for a tailless DelFly model in hover conditions. Up to now, no

experimental investigations have been performed on a DelFly model in forward flight configurations with tail. Experience has shown that the position of the tail with respect to the flapping wings has a significant influence on the stability of the DelFly. As a rule of thumb, the tail is positioned three finger thicknesses downstream the trailing edges of the flapping wings. The current study is dedicated towards these research topics. The goal of this thesis is to:

Perform force measurements and flow visualizations in the wake of the flapping wing MAV 'DelFly II' in forward flight configuration

A stereoscopic Particle Image Velocimetry (PIV) setup is used in combination with a sensitive compact six-component force sensor. The stereoscopic PIV results are used to reconstruct a three-dimensional wake behind the DelFly. Simultaneous force measurements allow to correlate the generated forces with the flow structure in the wake of the DelFly.

1.2   Thesis outline

This report consists of a number of different parts. While the DelFly has a strong relation with insect flight, first of all a theoretical background for flapping wing aerodynamics is given in chapter 2. Different aspects regarding the kinematics and lift production of flapping wings are discussed. Furthermore, researches regarding the flow structures in the wake of a flapping wing are discussed. Finally, attention is given to the interaction between a flapping wing-tail configuration. Chapter 3 presents the subject of the current research: DelFly II. The history and design of the DelFly are discussed in this chapter. Previous researches on the DelFly are also discussed in this chapter. Basic principles behind the experimental PIV technique used in the present research are discussed in chapter 4. An overview and detailed discussion of the experimental setup as used in the current research can be found in chapter 5. Both the force setup and the PIV measurement setup are described in detail. The results of the experiments including an extensive discussion is found in chapter 7. This report finishes with conclusions that are drawn from the experiments including the recommendations for future research (see chapter 8).

Flapping wing aerodynamics

The flapping wing configuration that is utilized by the DelFly, i.e. clap-and-fling mechanism, has a strong relation with insect flight. The flapping wing configuration is responsible for generating lift and thrust during flight. In order to get a better insight into the clap-and-fling mechanism of the DelFly, a number of experimental studies were performed [3, 2, 1] and the knowledge gathered was used to improve the aerodynamic performance of the DelFly. However, these studies focused on the aerodynamic mechanisms in the vicinity of the wings for a tailless DelFly model in hover condition. In this chapter, it is aimed to investigate the wake of the flapping wing in forward flight condition with a tail placed downstream at different configurations. In this chapter, a theoretical background is provided initially. Wing kinematics in insect flight and different unsteady aerodynamic mechanisms that are particular to the insect flight are defined. Next, the aerodynamic characteristics of the clap-and-fling mechanism are presented. Finally, special attention is given to the wake of flapping wings.

2.1 Unsteady aerodynamics in insect flight

In this section,the underlying unsteady aerodynamics of insect flight are analyzed in details. First, kinematics of flapping wing motion of insects is described in general. Later, major aerodynamic mechanisms that are responsible for force generation and maneuverability of insects are discussed.

2.1.1 Kinematics

In general, flapping motion of an insect wing consists of three different phases: sweeping, heaving and pitching. Sweeping is fore and aft motion of the wing, whereas heaving is the up and down motion. During a complete flapping cycle, the wing performs two translations (a downstroke and an upstroke, see figure 2.1), and two rotations. The rotation at the end of the down-stroke is called pronation, whereas the rotation at the end of the up-stroke is called supination. The reason of the rotational motions at the end of the strokes is to have a positive angle of attack which in turn results in lift generation.

It is found that during the up and downstroke, the wings undergo heaving motion but almost no pitching motion is present. The timing of the rotational phase with respect to the translational part is also important for the lift generation according to Dickinson et al. [4]. In case the rotation
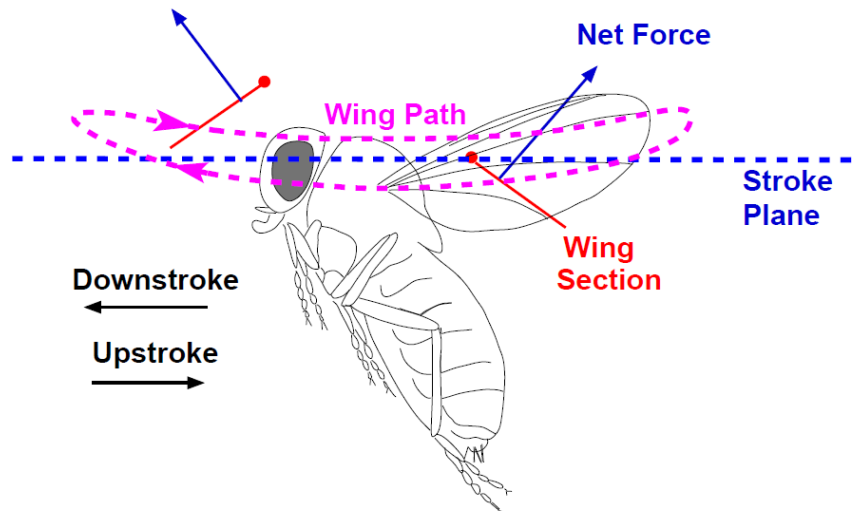
Figure 2.1 – *Kinematics of Insect flight. Adapted from Singh et al. [5]*

occurs before the translation is finished, the rotation is called advanced. When the wing rotation is synchronized with the wing stroke cycle, then the rotation is called symmetric. If the rotation occurs after stroke reversal one speaks of delayed rotation. Different types of rotations are depicted in figure 2.2. Insects are able to actively change the kinematics of the flapping wing, depending on the conditions in which they fly. An insect can for instance change the location of the pitching axes during a maneuver. Yates [6] researched the question of what is the most practical axis about which to implement the rotational motion of a wing during flapping wing propulsion? He suggests that the choice of the pitching axis may enhance performance and control of rapid maneuvers. By doing so, the insect is more capable of dealing with turbulent environmental conditions, danger avoidance, or food capture with ease. Shyy et al. [7] states that the wing kinematics is the primary driver of the unsteady aerodynamics in flapping wing flight. Ansari et al. [8] studied the effects of wing kinematics on the aerodynamics of flapping wings in hover mode operating in the Reynolds number range of the order O(102). Flapping frequency, stroke amplitude and rotation phase were independently changed. Increasing the flapping frequency is beneficial for a higher lift without increasing the lift-to-torque ratio (in case the wing geometry is unchanged). Increasing the stroke amplitude yields a significant increase in both lift and drag. Finally, also the rotational phase was changed. Testing advanced, symmetric and delayed rotation yields that the advanced rotation can be used to enhance the lift generation performance of the wings.

2.1.2   Aerodynamics mechanisms

There are five major mechanisms which are effective in insect flight according to Sane [9]:

1. Wagner effect

2. Clap-and-fling

3. Delayed stall and the leading edge vortex (LEV)

4. Kramer effect (rotational forces)

5. Wing-wake interactions

In the present section each of these mechanism is discussed shortly.
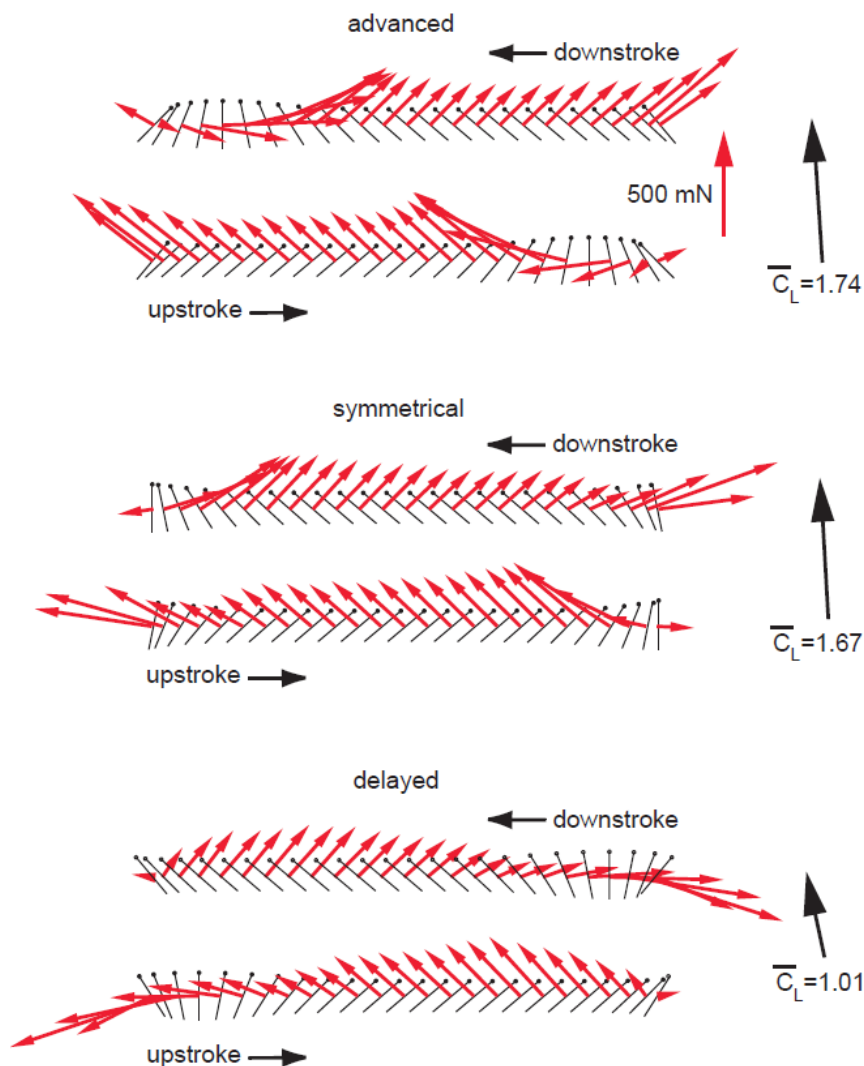
Figure 2.2 – *Advanced, symmetrical and delayed rotation. Adapted from Dickinson et al. [4]*

2.1.3 Effect of flexibility in clap-and-fling motion

So far, flapping wing aerodynamics with rigid wings has been discussed and the most effective aero-dynamic mechanisms have been explained. However, it is known that insect wings have complex stiffness variations and they are definitely flexible [10],[11]. Hence, effect of flexibility in flapping flight has become a popular research topic. Although there is growing evidence that wing deformation is beneficial in terms of lift and thrust production [12], still a lot of aspects regarding flexibility remain relatively unexplored [13]. In this chapter, the effects of flexibility on the flapping wing aerodynamics are discussed. First, effects of chordwise, spanwise, combined chordwise and spanwise flexibility in basic flapping motions are explained, respectively. Then, flexibility effects in the clap-and-fling motion are analyzed due to the inherent flexibility of the DelFly wings.

Wing flexibility has a significant influence on the clap-and-fling motion which is clearly visible in wing deformations during the flapping cycle. With the effect of flexibility, the clap and fling phases do not occur as they do in the rigid wing case. Ellington [**?**] states that the fling phase looks more like a peel. During this phase, the wings first separate from each other at the leading edge. The separation point moves smoothly down while the wings curve as shown in figure 2.3A. This is opposite to the clap-and-fling where the wings rotate about the trailing edge during the fling phase. On the other hand,

clap can be considered as reverse-peel [?]. First the leading edges touch, after that the wing surface below the leading edge starts to move smoothly parallel till the trailing edges touch (figure 2.3C). Due to mentioned differences, clap-and-fling motion with flexible wings is called clap-and-peel. The wing deformation in the clap-and-peel mechanism is often a passive mechanism. The wings deform under influence of inertial, elastic and aerodynamic forces acting on the wing. Lehmann et al[15] suggested that the peel offers a benefit in comparison to the fling. Since the trailing edge gap remains closed during the peel phase, fluid cannot enter from behind the trailing edge. During the fling phase with rigid wings, this condition creates strong trailing edge vorticity which in turn decreases the benefits of leading edge vorticity. Therefore the peel mechanism prevents an upward momentum jet, which works against the generation of lift during the peel phase.
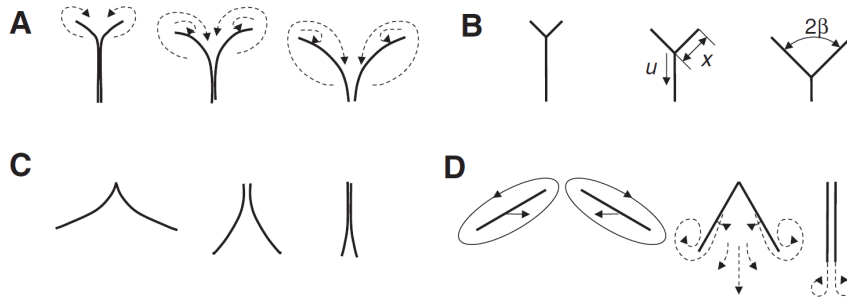
Figure 2.3 – *The clap-and-peel mechanism. Adapted from Miller and Peskin [16]*

Miller and Peskin [16] performed numerical simulations on the clap-and-peel mechanism in tiny insect flight, at the Reynolds number of about 10. They compared the clap-and-peel with clap-and-fling. Based on their simulations, wing flexibility turns out to be an important parameter in reducing drag forces during clap-and-fling. For small insects, as they considered, a drag reduction of 50% is achieved during fling. During both the clap and the peel, the lift over drag ratio is improved with respect to the rigid clap-and-fling. The first experimental research on the DelFly II to reveal the effects of flexibility in flapping flight was carried out by De Clercq [1]. She performed Stereo-PIV and force measurements to capture time dependent flow fields in the vicinity of the wing and to acquire the forces generated during the flapping cycle in hover condition. Based on the experimental results, it was shown that the flexibility of the wings during the peel phase is responsible for the lift enhancement. Furthermore, Bruggeman [2] performed extensive research on the wing design of the DelFly. The goal of this research was to improve the thrust to power ratio of the DelFly flapping wing system. By systematically changing the stiffener location, an optimum thrust-to-power ratio was found. The optimized wing results in an increase of 10% in the thrust-to-power ratio. Groen [3] performed phase-locked stereo-PIV measurements on the original and improved wing. The flow field around the wings, and the deformation of both wings were compared. It was found out that the improved wing is less flexible compared to the original wing shape. Thanks to this increased stiffness, the LEV stays closer to the wing surface due to the increased suction in the peeling phase as shown in figure 2.4.

2.2   On the wake of flapping wings

The phenomena described in the previous sections mainly focus on the flow in close vicinity of the wing. The vorticity that is generated by the wings is convected into the wake. Hedenström et al. [17] states that the vortex wake contains the check sum momentum generated to overcome lift and drag, irrespective of the structures, shape and kinematics that generated it. According to Kelvin's theorem, every change in circulation at the wing is accompanied by the shedding of vorticity of equal and opposite sign into the wake (in a closed section) [18]. This change in circulation in the wake can be used to estimate the forces generated by the flapping wing. Note that wake dissipation and interactions are assumed to be negligible. The so-called vortex-wake method, in which forces are derived from vorticity shed into the wake, is often used in research that involves free-flying animals. By doing so, the animals are disturbed minimally [19]. In this chapter, wake formations of the flapping
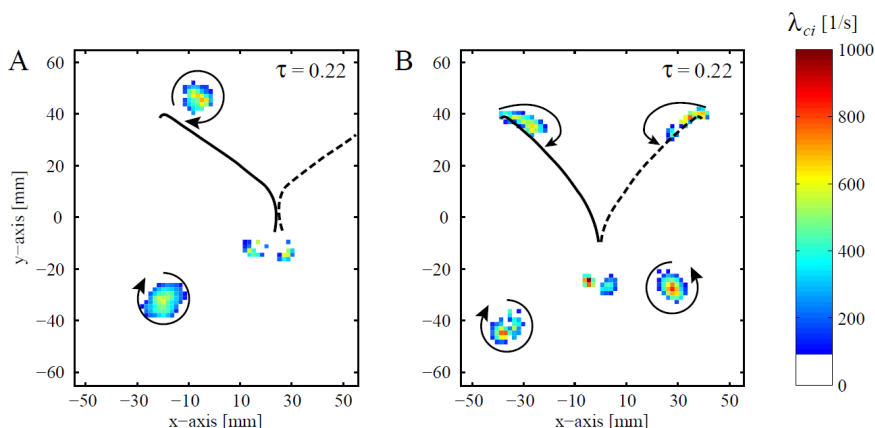
Figure 2.4 – *Swirling strength halfway during the outstroke for the original wing (A) and the improved wing (B) flapping at 13 Hz at spanwise location 0.86R. Adapted from Groen [3]*

wings are discussed in details. First, different wake topologies are described. Then, the interactions in tandem wing configuration are described. This chapter is ended with a small discussion on the flapping wing-tail interaction due to small number of articles about this topic.

2.2.1 Wake topology

The research on the wake topology starts with the research of Burgers and von Kármán [20]. In 1935, they were the first to provide an explanation of the drag or thrust production of a cylinder by looking at the orientation and location of the wake vortices. The wake of a body on which a drag force is exerted consists of a double row of vortices of alternating sign. The well-known pattern they observed is also known as the Kármán vortex street (see figure 2.5). If a drag force is exerted on the body, the top row of vortices rotates clockwise and the bottom row counter-clockwise, resulting in a momentum deficit wake profile (figure 2.5A). In case a thrust force is exerted on the airfoil, the upper row of vortices rotates counter-clockwise and the bottom row rotates clockwise, inducing a momentum surfeit wake profile (see figure 2.5b).
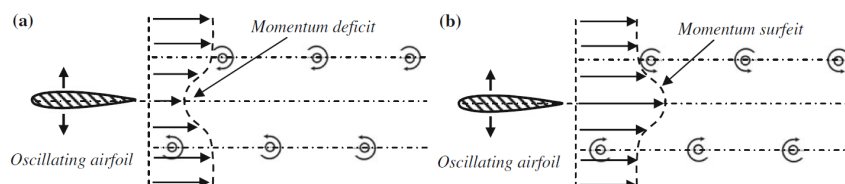
Figure 2.5 – *Typical wake flow patterns in the downstream of 2D oscillating airfoils. (a) Drag-producing wake. (b) Thrust-producing wake. Adapted from Hu et al.[21]*

Similar observations were made when looking at the wake of flapping wing configurations. Lai and Platzer [22] performed water tunnel tests on sinusoidally plunging NACA 0012 airfoil. By means of dye flow visualization, the jet characteristics of this plunging airfoil were visualized. The results, shown in figure 2.6, give the vortex pattern in the wake of the flapping airfoil. It was found that a certain value of kh gives the transition from a drag to thrust producing airfoil, accompanied by a change from normal to reversed Krmn vortex street.

Anderson et al. [23] performed research on the wake topology of a harmonically pitching and plunging rigid NACA 0012 airfoil. By systematically changing the Strouhal number and the maximum angle of attack of the airfoil, they obtained wake patterns of the different flight conditions (see figure 2.7). The generated LEV and TEV are shed into the wake behind the flapping wing. First of all, the shape of this vortex street is strongly dependent on the generation of a LEV. If no LEV is generated because no leading edge separation occurs, the wing has a completely different layout compared to the case
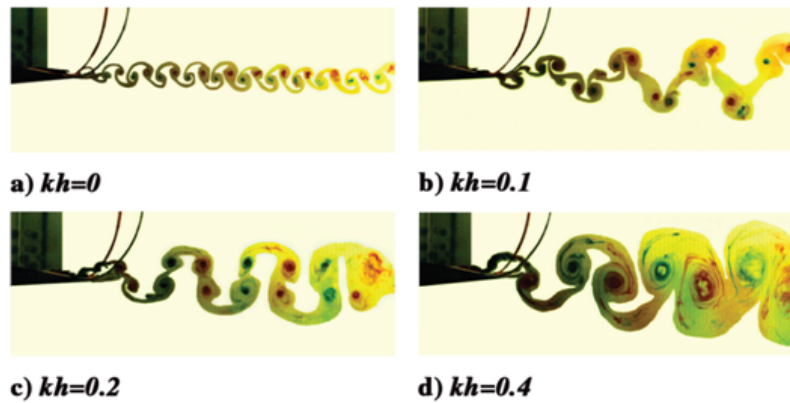
Figure 2.6 – *Transition from normal to reverse Krmn vortex street with increasing kh (Product of reduced frequency and non-dimensional plunge amplitude). Adapted from Platzer et al. [22]*

where a LEV is generated and shed into the wake.
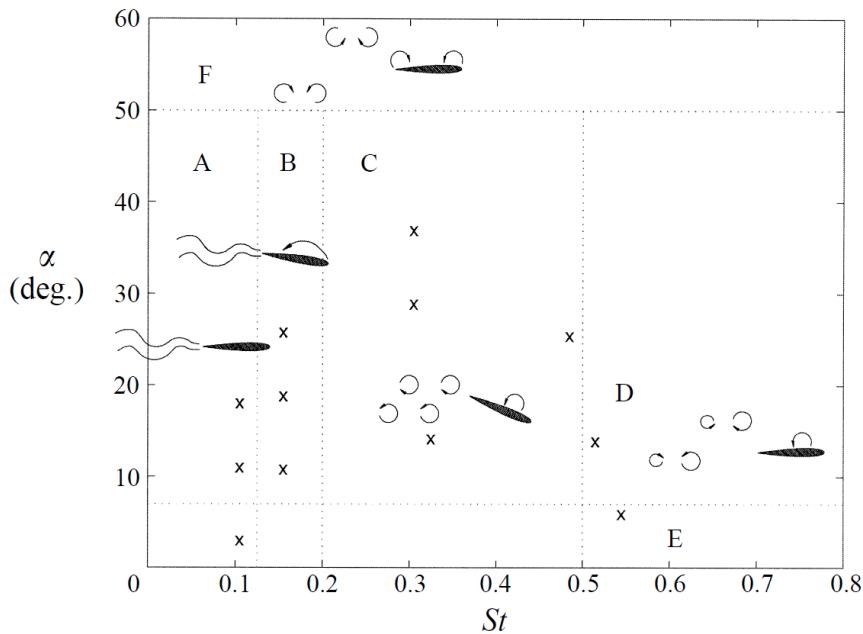
Figure 2.7 – *Wake patterns as functions of the Strouhal number and the maximum effective angle of attack. Adapted from Anderson et al. [23]*

An increasing kh leads to a transition from a vortex wake to a reversed Kármán vortex street. The transition from the normal vortex wake to the reversed Krmn vortex wake is the point at which the force component in streamwise direction changes sign. However, it should be noted that the product kh, and thus the Strouhal number, is not sufficient to characterize whether a flapping airfoil produces thrust or drag. There is no fixed value for kh for which the transition from drag to thrust production. Research by Jones et al. [24] showed that for a fixed value of kh, different wake structures are encountered. One can say that for a fixed value of h or k, one should exceed a certain value of kh in order to produce thrust, see figure 2.8.

Research on the three dimensional wake topology of flapping wings was performed by Guerrero [25]. A numerical study was performed in order to obtain the influence of the Strouhal number on the wake topology and aerodynamic performance of a rigid, finite span flapping wing. Pure heaving, coupled heaving and pitching and rolling motions were simulated. The range of Reynolds number for this study was between 500 and 1100. The so-called Q-criterion was used to identify vortical structures
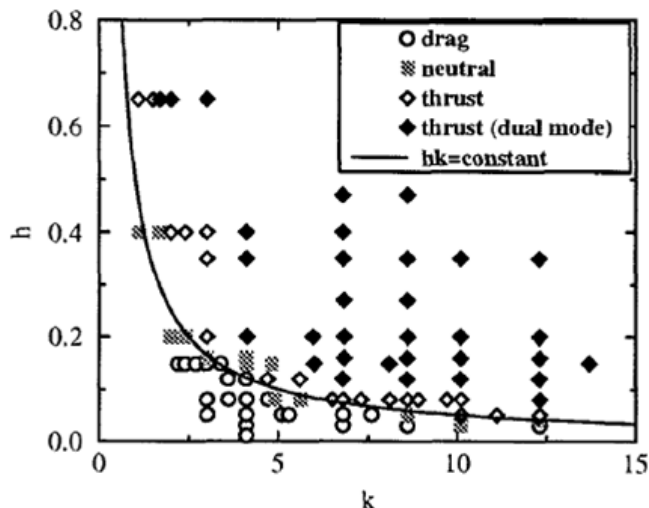
Figure 2.8 – *Drag/thrust as a function of h and k. Adapted from Jones et al. [24]*

in the flow. For the pure heaving motion, the wing produces several vortex rings being shed into the wake. The vortex shedding at the beginning of the upstroke is shown in figure 2.9. From the top view, it is clearly visible that vortex rings are being formed. In contrast to the two dimensional case where a pure von Kármán vortex (or reversed in case of thrust production) is produced, in the three dimensional case, additional features appear in the wake. The two tip vortices that appear at the wing tips connect the leading edge vortex and the trailing edge vortex. As they are being shed into the wake, they are connected in a vortex ring. This is clearly visible in figure 2.9. Additionally the wake topology of a root-flapping wing is simulated(figure 2.10). In contrast to the heaving airfoil, shown in figure 2.9, it is noticed that the connection between leading edge and trailing edge vortices is much weaker. Presumably this has to do with the fact that the average velocity across the span is much lower compared to the heaving motion.
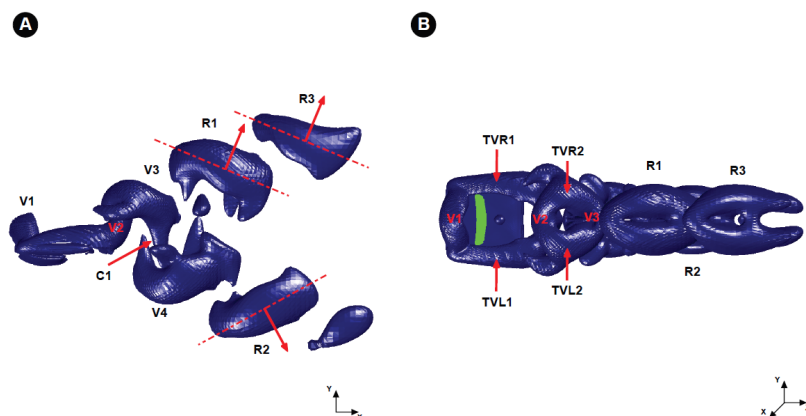
Figure 2.9 – *Vortex topology at the beginning of the upstroke. Flapping parameters: St = 0.5, ha = 0.25, Re = 500. A) Side view, B) Top view. Adapted from Guerrero [25]*

A lot of research on the time resolved wake of bat flight is performed by Hubel et al. [26], Muijres et al. [27], Muijres et al. [28] , Stuiver [29] Hedenström et al. [30]. The goal of studying the wake of the bats is to create an average wake pattern from which the flight performance properties can be deduced. The vortex wake is reconstructed by making transverse PIV measurements at different time instants during the flap cycle. Hedenström et al.[30] performed experiments on a G. soricina bat flying at a Reynolds number range of 4,000 till 18,000. A systematic and quantive study was done at different flight speeds (ranging from 1.5 to 6.5 m/s), to see the effect of flight speed on the formation

Figure 2.10 – *Vortex topology for the rolling wing case (t = 5.0). Flapping parameters: St = 0.25, froll = 1.0, Re = 500. A) Perspective view, B) Top view, In this view right wing-tip corresponds to the hinged extreme. C) Side view. Adapted from Guerrero [25]*

of the wake geometry. Stereoscopic PIV measurements were used in order to construct a wake model of the bat. First, the circulation strength of the strongest starting and stopping vortices decrease with flight speed. This suggests that the wake topology changes continuously with flight speed. Second, the wake topology of a flapping bat is much more complex then assumed by Rayner et al.[31]. In a follow-up study by Hedenström et al. [32], a 3D high speed PIV measurement setup was used in order to reconstruct the wake of flapping G. soricina and L. curasoa bats. The results of this research show good correlation with previous research done by Hedenstrom et al.[30]. Testing two different bat species, which differed in body size, revealed that the vortex wake topology is qualitatively the same for both bats. Interesting results are provided by Muijres et al. [28]. Again time-resolved stereoscopic PIV was used to construct the wake of a G. soricina bat. The reconstructed wake is shown in figure 2.11. The figure has to be read from right to left. The wing starts with a downstroke, then changes direction and performs an upstroke. Basically four different aerodynamics features show up: the starting vortex, the tip vortex, the root vortex and a reversed vortex dipole. From the top right picture shown in figure 2.11, the starting vortex, present along the span of the wing, is connected with the tip vortex and also to the root vortex. During the downstroke, both tip and root vortices are present. During the upstroke, the root vortices are too weak, so they are not shown in the wake representation. Halfway during the upstroke the tip vortices are converted into two distinct vortex loops, the so-called reversed vortex dipole. The result of these reversed vortex loops is the generation of an upwash, resulting in negative lift generation. This is in contrast to what Guerrero [25] showed for a flapping airfoil. In the same area of bat flight, Muijres et al. [27] performed time-resolved PIV experiments on two bat species which allowed them to create an average wake and thus estimating the forces generated throughout a wingbeat. Although minor differences were found in the force production of the two species (i.e. optimum flight condition), still the wake dynamics were found to be quite similar. This was also one of their hypotheses because both species fly at similar Reynolds- and Strouhal numbers. Qualitatively, the wake dynamics was found to be similar to the results given by Hedenstrom et al. [30], but the high speed PIV technique allowed them to make a more detailed wake representation. The reconstruction of the bat wakes in the previous studies was performed based on the data acquired at far-wake location. However, the evolution of wake structures up to that point can result in misinterpretation of wake topology and incorrect force estimations. Johansson et al. [33] carried out near-wake and far-wake measurements to perform a quantitative comparison. They showed that peak vorticity of starting and stopping vortices decreases with increasing downstream location. The main reason for this is the diffusion of vorticity as it moves downstream. However, the total circulation of starting and stopping vortices remains approximately constant. Consequently,

the forces derived from a far-wake analysis are quantitatively consistent with a near-wake analysis. Finally, some particular details of the vortex wake structure were clearly visible in the near wake, whereas in the far wake these details were almost not visible.
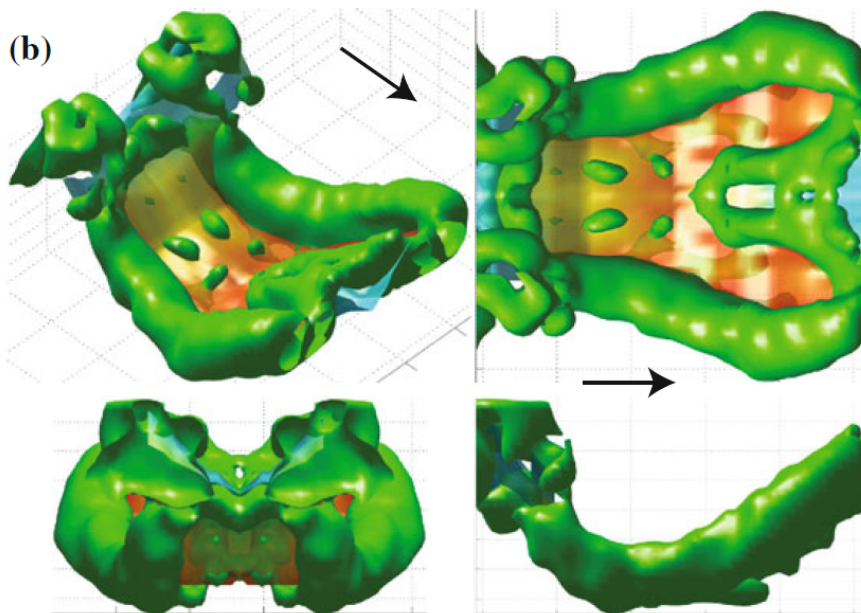
Figure 2.11 – *Vortex-wake and actuator disk surface for a single wingbeat of G. soricina flying at a flight speed of 4 m/s. The vortex wake is visualizedusing green iso-surfaces of constant absolute vorticity. The actuator disk surface encircled by the vortex structures is color coded using the vertical induced velocity w according to the color bar on the bottom of the figure. Adapted from Muijres et al. [28]*

2.2.2   Wing-wing interaction

The wing-tail interaction as found in several flapping MAV designs is not researched very thoroughly. Although a lot of questions remain unanswered, some studies have reported upon this subject. The very complex wake of a flapping wing, as discussed in the previous section is used here to evaluate the interaction of the flapping wing on the tail. It is assumed that tip vortices, starting and stopping vortices that are shed in the wake create a non uniform flow on the tail of the DelFly. In order to evaluate the effect of the wake of a flapping wing on the tail, a comparison is made with the steady wing case. For a steady wing with an elliptical lift distribution, the downwash at a downstream location has the shape as depicted in figure 2.12. From stereoscopic PIV measurements, Muijres et al. [28] obtained the average downwash distribution during different phases of a flap cycle (figure 2.13). It is not surprising to conclude that induced velocity profiles at downstream positions for steady and flapping wings (figure 2.12A and figure 2.12B, respectively) are completely different.

The wake of the wing passes over the tail. In the idealized steady wing case, shown in figure 2.13A, the tail would experience a constant downwash along the span. In contrast to this condition, the flapping wing provides a varying down/up wash along the span of the tail. Therefore, some parts of the tail would experience a negative angle of attack whereas others experience a positive angle of attack. Consequently, the resulting lift distribution varies strongly in spanwise direction. As evident from figure 2.13B, the downwash changes into upwash during the upstroke. As a result, negative lift is generated by the tail of the flapping MAV, possibly leading to a destabilizing pitching moment. The positive influence of a steady wing behind a flapping wing was recognized during the Second World War by Schmidt [34]. The design of a new propulsive method led him to the development of the wave propeller. Wind tunnel analysis showed that when a steady wing is present in the wake of the flapping airfoil, the propulsive efficiency is doubled. It is believed that the vortical energy contained in the wake of the flapping airfoil is converted into additional thrust by the second airfoil. Tuncer and
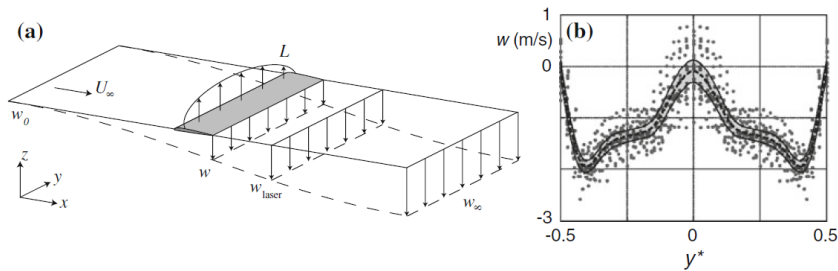
Figure 2.12 – *(a) The vertical induced velocity behind a steady wing with an elliptical lift-distribution L. The downwash increases from 0 far upstream till $w_\infty = 2w$ far downstream in the wake. b) The vertical induced velocity distribution along the non-dimensionalized wake span, at mid downstroke for G. soricina at 4m/s, the dotted line is the smoothing spline through these data, and the shaded area around the dotted line shows the 95% confidence interval. Adapted from Muijres et al. [28]*
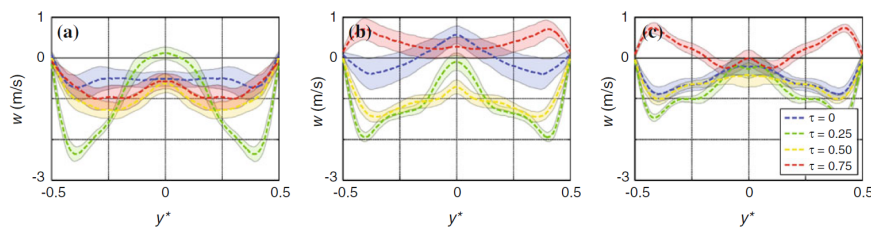
Figure 2.13 – *Average spanwise downwash distributions, with 95% confidence interval, at different moments within the wingbeat. The graphs show the data for G. soricina at 2 m/s (a), 4 m/s (b), 7 m/s (c). Each panel shows the downwash at four points within the wingbeat: start of the downstroke ($\tau = 0$); mid downstroke ($\tau = 0.25$); end of the downstroke ($\tau = 0.5$); mid upstroke ($\tau = 0.75$). Adapted from Muijres et al. [28]*

Platzer [35] used a Navier-Stokes solver to compute the flow field around a single flapping NACA 0012 airfoil and a tandem flapping/stationary NACA 0012 airfoil combination . The shed vorticity from the front airfoil strongly interacts with the boundary layers of the trailing airfoil. Comparison of the single flapping wing with the tandem wing case revealed that although the flapping wings for both cases generate same amount of thrust, the tandem wing configuration creates higher thrust thanks to the force generated by steady trailing airfoil. Physically the vortical wake of the flapping airfoil induces a flow field, as shown in figure 2.14, creating a suction force at the leading edge of trailing airfoil. It is quite important that the airfoils do not have a vertical offset more than the flapping amplitude so that the shed vorticity can still interact with the trailing airfoil. The stronger this interaction, the higher the thrust. Regarding to the horizontal distance between the airfoils, it was found that the highest total thrust is achieved if the distance between the airfoils is 65% of the chord length. However the propulsive efficiency is at this point quite low, possibly due to the blockage effect of the trailing airfoil.

Different research was done by Aziz et al. [36]. Their numerical research showed that in tandem wing configuration, the wings have a dramatic influence on each other. The wings were impulsively set into motion. Comparing the lift, drag and moment generated by a tandem airfoil configuration in comparison with a single airfoil, it was found that all parameters under consideration are affected by the presence of a second wing. From here on the front and back airfoil are mentioned as airfoil A and B, respectively. First of all, the impact of the TEV from the airfoil A on the airfoil B yields some important observations, see figure 2.15. The TEV causes a downwash on airfoil B, resulting in a drop in lift. On the other hand, the downwash generated at airfoil A due to this TEV decreases, resulting in an increase in lift. After the first impact of the TEV from airfoil A on the airfoil B, the downwash generated by airfoil A yields a lower lift at airfoil B (compared to a single airfoil). At the same time however, the bound vorticity of airfoil B generates an up wash at airfoil A, yielding a higher lift compared to a single airfoil. Secondly, the horizontal and vertical distance between the airfoil A and B was changed. Increasing the horizontal distance leads to a diminished interaction between the airfoils. The TEV interaction between two airfoils becomes less severe, leading to lower peaks in lift coefficient. Due to the decreased interaction, the resulting lift of both airfoils approaches
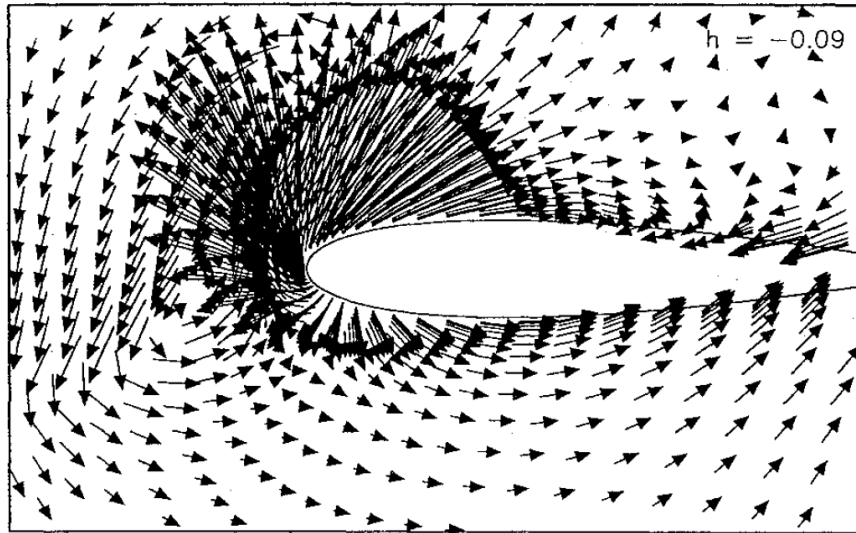
Figure 2.14 – *Disturbance velocity vectors around the leading edge of the trailing airfoil at time when the trust is maximum. Adapted from Tuncer and Platzer [35]*

the lift produced by the single wing. As a consequence of increasing the vertical distance between the airfoils, the TEV from airfoil A does not interact with airfoil B. Although the sharp spikes, present in figure 2.15, disappear for airfoil B, they remain for airfoil A. A possible reason for this behavior is the dominance of the very strong TEV. Finally the angle of attack of airfoil A was changed, resulting in a more pronounced influence of the airfoils on each other (as explained before).
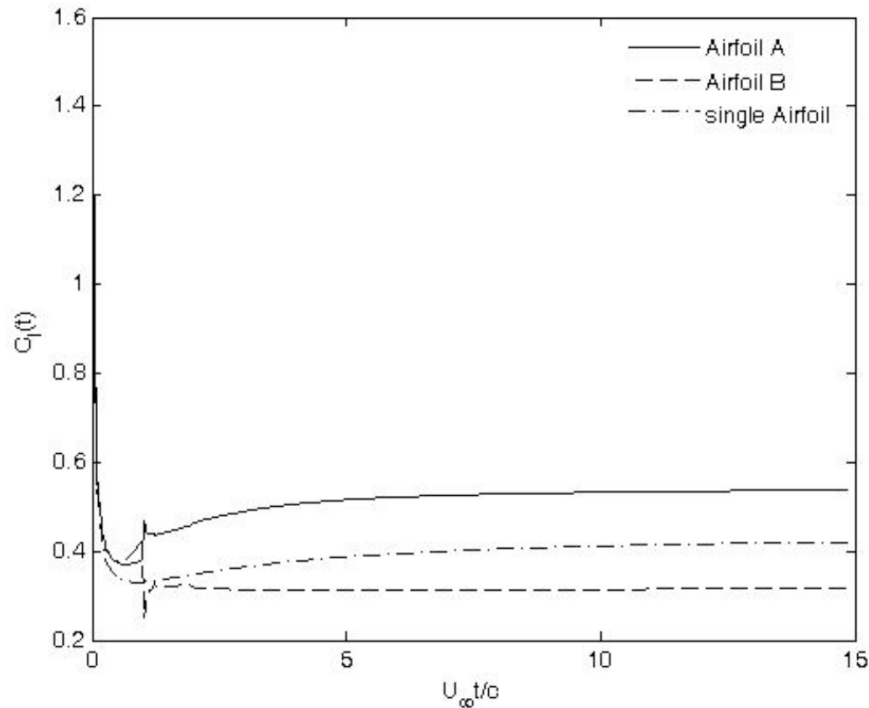
Figure 2.15 – *$C_l(t)$ of an airfoil operating by itself and in configuration. Adapted from Aziz and Mukherjee [36]*

DelFly

The subject of the current research is the DelFly II. This chapter is dedicated to several aspects regarding the DelFly. First of all the history of the DelFly is given in 3.1. The design of DelFly II is discussed in detail in paragraph 3.2. Finally paragraph 3.3 gives an overview of the different researches that have been performed in the previous years.

3.1 History of the DelFly

The DelFly is bio-inspired ornithopter designed and built by the Delft University of Technology. In 2005 a group of bachelor student worked on the design of a vision based flapping wing MAV. Their goal was to *Impress the jury of the first US-European Micro UAV Competition by designing a flapping wing, vision based MAV, using commercially off the shelf products, within a budget of 5000, with eleven students in ten weeks*[?].They succeeded in building a flying flapping MAV. Although they were not the winning team on the EMAV '05 in Germany, The design was regarded as the "Most Exotic Design". From that point on the the interest and research in a flapping wing MAV has increased largely. The first version of the DelFly, the socalled DelFly I (see figure 3.1), has a span of 35 cm, a length of 41 cm and a total weight of 21 grams. This includes an brushed motor to drive the flapping wings, a

Figure 3.1 – *DelFly I in fligth in the alpes*

gear system, micro-actuators to actuate the tail control surfaces, a camera to able to fly autonously, a

receiver to be able to remote control the DelFly, a battery to provide power for 15 minutes and finally a motor controller to control the small electrical motor. The structure consists mainly out of carbon rods, providing a stiff, strong and light construction. The wings are manufactured out of very thin transparent Mylar foil. All the different parts are connected to each other by different types of glues. The DelFly I is capable of flying in forward/backward and hover mode ($V_\infty = -1...7\,m/s$)

The design of the DelFly I is optimized during the subsequent years by the Aerospace Software and Technologies (ASTI). A top down design method is chosen to scale down the DelFly to smaller sizes. This led to the development of the DelFly II. With a wing span of 28 cm and a weight of 17 grams, this design has better properties compared to the DelFly I. The small battery gives energy to sustain hover flight for 8 minutes, whereas 15 minutes of forward flight is possible. Smaller electronics, a smaller and more efficient brushless motor with an efficiency of about 60% and a different wing shape made this smaller size possible. The DelFly II is currently the most stable flying platform that evolved from the DelFly I. It is also the version that is used in the current research. As an abbreviation the DelFly II is mentioned as DelFly from now on. In 2008 the MAVlab was able to scale the DelFly more, yielding the design of DelFly Micro (see figure 3.3). With a weight of 3.07 grams, a span of 10 cm and a length of 10.7 cm, it is the worlds smallest flying ornithopter wit a camera and transmitter onboard [38]. However, the DelFly Micro is not able to hover yet. The thrust delivered in hover conditions is not enough to sustain hover flight. This is mainly due to the overheating of its brushed motor. Current research on the DelFly Micro focusses on the ability to hover this micro MAV.

Figure 3.2 – *DelFly II in flight*

3.2   Design and similarity parameters of the DelFly

The design of the DelFly is based on the dragonfly, a biplane wing design. With a length of 28 cm, a spanwidth of 28 cm and a weight of 17 grams a very stable platform for performing autonoumous vision based flight. The design of the DelFly is discussed in detail in this section. Furthermore, the similarity parameters that are important for the DelFly are discussed.
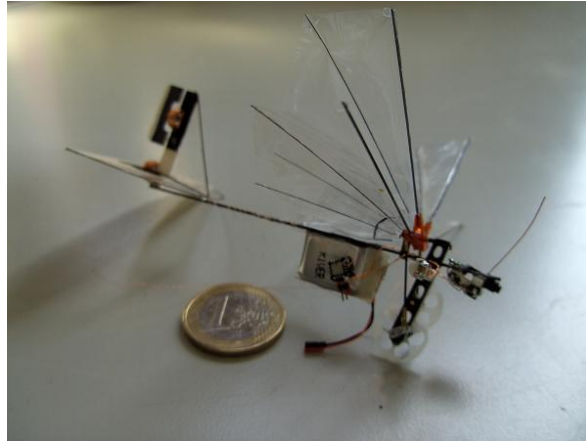
Figure 3.3 – *DelFly Micro in comparison with a 1 euro coin*

3.2.1 Design

Fuselage and wings

The fuselage is a hollow square carbon rod with external dimensions of 2 x 2 mm. All electronics and the battery are glued to this fuselage. The wings are made out of 5 micron thick Mylar foil, reinforced with carbon rods. This Mylar foil is a transparent Biaxially-oriented polyethylene therephthalate polyester film. This foil has a high strength and stiffness inplane. It is used in quite a number of applications[1]. In order to provide out of plane stiffness, D-shaped carbon rods (0.7 x 1.4 mm) function as the leading edges of the wings to provide spanwise stiffness, wheras carbon rods ($\varnothing$0.28 mm) provide chordwise stiffness. A detailed description of the manufacturing process of the wings can be found in the thesis of Bruggeman [2]. The wing layout is shown in figure 3.4
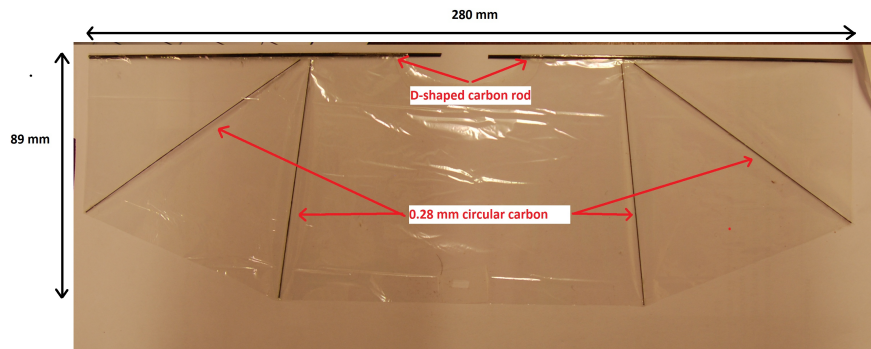
Figure 3.4 – *Layout of the flapping wing of the DelFly*

Tail

During the current research the tail of the DelFly has been further developed. The previous tail was made from Mylar foil reinforced with carbon rods. Due to the curved shape, it was quite difficult to manufacture. Furthermore, the servo motors actuating the horizontal and vertical rudder needed to be fixed to the fuselage, thereby increasing the complexity of the design. Also the crashworthiness of the current tail could be improved. However, the weight of the DelFly is not allowed to increase. A light and strong Extruded Polystyrene Foam was found to fit well these requirements. Depron Foam with a thickness of 2 mm was chosen. This material is very easy to process, leightweight and very

---

[1]http://en.wikipedia.org/wiki/BoPET

strong and stiff. While this material is anisotropic for stiffness and strength, care must be taken which direction is chosen to be spanwise and which the chordwise direction. Since the greatest length is in spanwise direction, the stiffest direction is oriented in this direction to minimize deformations. With help of a simple Stanley knife this material can be cut in the right shape. The hinges of the rudders are simply created by removing most of the material along a small line accross the horizontal and vertical tail. Furthermore, the servo motors can now be included in the tail, yielding a much simpler and cleaner tail. The connection to with the control surfaces is made out of flexible piano steel wire, making mechanical trimming easy. The resulting tail is shown in figure 3.5
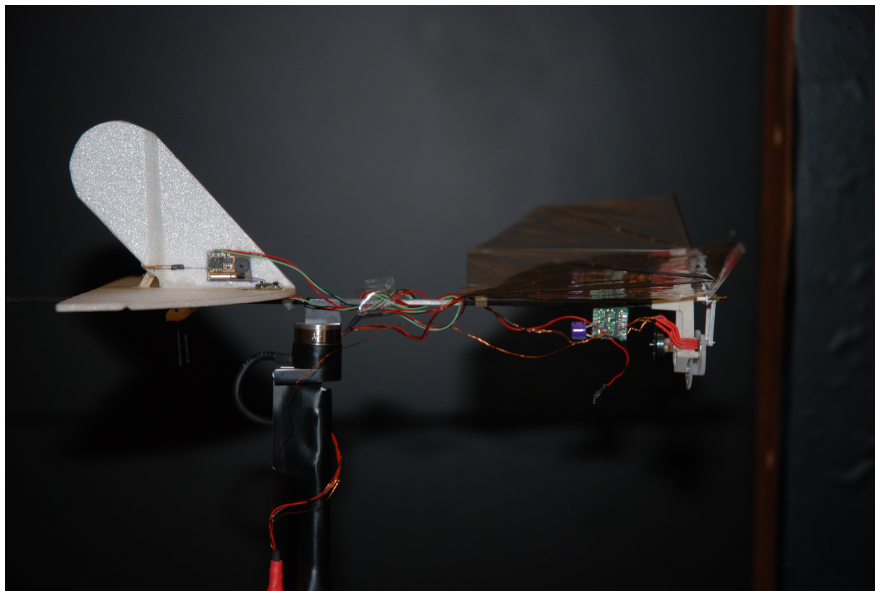
Figure 3.5 – *Layout of the tail of the DelFly*

Gearbox

The gearbox shown in figure 3.2 has been changed by Bruggeman [2]. He performed an optimization study for both wings and the gearbox mechanism. The resulting gearbox, which will be discussed in paragraph 3.3 is shown in figure 3.6. The gear ratio (GR) of the new gearbox (1:21.33) has changed compared to the old one (1:20). This Gear Ratio shows the number of revolutions that the motor turns in order to complete one flapcycle. The specific benefits of the new gearbox over the old one are listed in section 3.3. The gearbox is made from Polyxymethylene (POM) which has better wear properties to Poly Carbonate (PC), which was initially used.

Electronics

The electronics part of the DelFly is based on both commercially available products and custom developed parts. First of all the wings are driven by a brushless motor. It is developed by the MAVlab and DC Enterprises [38] because the brushed motor in the DelFly I suffered from severe wearing, resulting in a lifetime of maximum an hour. Furthermore, the flight time was limited up to a few minutes. Heating and expanding of the rotor inside the motor was a significant problem. The brushless motor can reach much heigher efficiencies (60%). Its position can determined much more accurate, making the pulses coming from the motor very suitable for controlling the flapping frequency of the DelFly. Power supply is deliverd by a small lithium-polymer battery with a capacity of 140 mAh and a discharge rate up to 700 mA, sufficient to fly the DelFly for 8 minutes in hover conditions and 15 minutes in forward flight. Very small micro servos[2] are integrated into the tail of

---

[2]These servos are provided by `www.microflierradio.com`. The mentioned servo is the Super Sub Micro LZ .48 gm. Servo
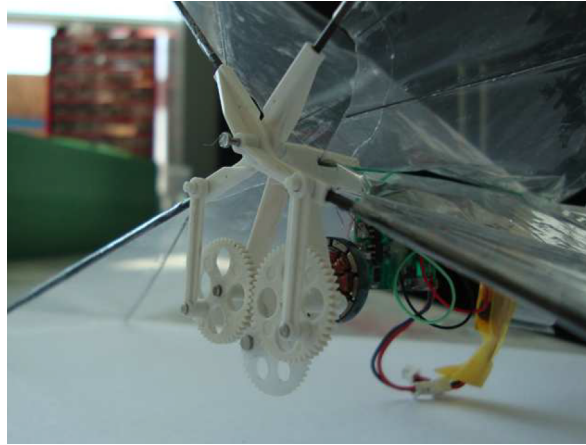
Figure 3.6 – *New crank-shaft mechanism for the DelFly II. Adapted from Bruggeman [2]*

the DelFly. These servos, with a weight of 0.65 gram and dimensions of 11 x 18 x 4 mm, provide a precise thrust of 10 gram with an maximum excitation of 6 mm. These specifications make them perfectly applicable for controlling the rudder and elevator of the DelFly. Finally the motorcontroller VARBL1 provided by Micro Planes Solutions[3] is used to control the brushless motor. For the current measurements no receiver is used. The DelFly is controlled by a custom designed micro controller board (see section 5.6).

3.2.2 Similarity parameters

Similarity parameters are non-dimensional numbers that are crucial in terms of analyzing the characteristics of the system under consideration and enabling the possibility of comparing different systems. In this section, some of the dimensionless numbers that are particular to the flapping wing aerodynamics are defined and discussed for the specific case in which the DelFly operates in forward flight conditions. It should be noted that the conventions and definitions used in this study are similar to that used by Ellington [37] and Shyy et al. [39]. Furthermore, the flapping frequency is fixed at 11 Hz. First of all, the Reynolds number. It is a non-dimensional number that provides a ratio between inertial and viscous forces in the flow. In general form it is defined as:

$$Re = \frac{\rho_f L_{ref} U_{ref}}{\mu} \tag{3.1}$$

For a simple 2D plunging and pitching motion the free-stream velocity is taken as the reference velocity and the chord length is taken as the reference length. For 3D motions, the reference length and velocity are depending upon the flight regime. For hovering motion, the wing tip velocity is taken as reference velocity, whereas in forward flight conditions the free-stream velocity is taken as the reference velocity. In both cases, the reference length is chosen to be the mean chord length. For the current research, in which forward flight conditions are considered, the following form of the Reynolds number is used:

$$Re = \frac{\rho_{air} \bar{c} \bar{U}_\infty}{\mu} \tag{3.2}$$

For the density of air, the density at zero meter in the International Standard Atmosphere is chosen ($1.225\ [kg/m^3]$). The viscosity is taken to be $1.78 \cdot 10^{-5}\ [kg/m \cdot s]$. In equation 3.2 the mean chord length is defined as:

$$\bar{c} = \frac{2R}{AR} = \frac{2RS}{b^2} \tag{3.3}$$

---

[3]http://www.microplanesolution.com/,last visit on 19-01-2012

In equation 3.3, R is the semi-wing span, S is the wing surface and b is the wing-span. Substituting the values which are specific for the DelFly, the Reynolds number in the forward flight regime $(3 - 8 m/s)$ varies between $5,500$ and $22,000$.

The advance ratio provides a non-dimensional measure for the flight speed. It is defined as the ratio between the free stream velocity and the wing tip velocity of the flapping wing:

$$J = \frac{U_\infty}{U_{tip}} \tag{3.4}$$

The advance ratio for the DelFly varies between 0 for the hovering flight case upto 3.4. In this case the average wing tip velocity is taken as a reference. The wingtip velocity is defined as:

$$U_{tip} = 2nR\omega \tag{3.5}$$

In equation 3.5 n is the wing beat frequency and ω is the stroke amplitude. For the DelFly flapping at 11 Hz, the mean wing tip velocity is $2.4 m/s$. With a maximum forward velocity of 8 m/s, the advance ratio varies upto 3.4 in fast forward flight.

The third similarity parameter is the Strouhal number. In flapping flight the Strouhal number gives the relative influence of the forward flights versus the mean wing tip speed. The definition used in this research can be written as:

$$St = \frac{nL_{ref}}{U_{ref}} = \frac{nR\omega}{U_\infty} \tag{3.6}$$

The Strouhal number for the DelFly in forward flight conditions $(3 - 8\,[m/s])$ varies from 0.59 in slow forward flight to 0.15 in fast forward flight.

Finally the reduced frequency is defined. This non-dimensional parameter provides a measure of the unsteadiness associated with a flapping wing. The reduced frequency in general is defined as:

$$k = \frac{\pi c n}{U_{ref}} \tag{3.7}$$

Depending on the flight regime this quantity is defined differently. The reference velocity is taken as the mean wing velocity in hovering case. The flight speed is taken as reference in forward flight conditions,. Because forward flight conditions are considered in this study, the latter convention is chosen. The chord length in the 3D case is taken as the mean chord length of the wing. The reduced frequency can then be defined as:

$$k = \frac{\pi \bar{c} n}{U_\infty} \tag{3.8}$$

The reduced frequency varies between 0.69 for slow forward flight upto 0.17 for fast forward flight. The similarity parameters and the specification are summarized in Appendix B

3.3   Research and development

Since the introduction of the DelFly I in 2005 a lot of research has been dedicated towards the DelFly. Aerodynamic and performance characteristics have been subject of research in a number of studies [1],[3], [2]. In this section researches with respect to aerodynamics and structural aspects of the DelFly are discussed because these are of most interest towards the current research. Research on other topics of the DelFly, like autonomous flight, is also performed by the MAVlab. Algorithms have been developed which make vision based autonomous indoor flight possible. In contrast to

autonomous outdoor flight, autonomous indoor flight cannot rely on GPS based methods. Therefore, camera images are used to control the flight path of the DelFly. An efficient height estimation algorithm based on a *texton* method is developed [38]. Furthermore, a path tracking algorithm has been designed which allows the DelFly to follow a path with visible lines on the ground. In order to be completely independent of the indoor environment, so without relying on specific properties of the room, research is dedicated to development of an appearance based algorithm. This algorithm allows to autonomously fly the DelFly without knowing anything about the specific room in advance [38].

3.3.1 Aerodynamic research

Both De Clercq [1] and Groen [3] have worked on the aerodynamic research of the DelFly. De Clercq [1] performed time resolved PIV and force measurements in hovering flight conditions. A schematic overview of the experimental setups is given in figure 3.7. In this research the measurement plane was taken fixed with respect to the DelFly, yielding a large variation of measurement locations in spanwise direction. Force measurements were performed with two Zemic load cells, measuring both horizontal and vertical forces respectively.

The inflight wing shape is determined with the PIV cameras. It is shown that even before the clap has been finished, the peel already starts. Force peaks during one flap cycle could be correlated with PIV results. It is clearly shown that the generated forces are in close relation with the formation and shedding of vorticity. A downward momentum jet is found during the clap, forming two vortices on each wing. The peel effect is found to significantly enhance the lift, whereas the clap rather attenuates the lift production. The flex phase was also studied. Although no leading edge vortices could be observed due to optical blockage of the wing, no stopping vortex is being shed. This enhances the circulation and thus lift. Downwash of the air between the wings contributes to additional lift generation.

A follow up study was performed by Groen [3]. The previous research by De Clercq [1] showed a number of shortcomings. First of all, substantial reflections from the wing surface prohibited the possibility of flow visualisation in close vicinity of the wings. Furthermore, the radial position at which images are taken varied significantly (a deviation of 38% of the span when measuring at 75% of the span). In order to resolve both shortcomings, a phase locked approach was used in which the image was taken when the wing was perpendicular to the measurement plane. Now measurements are performed with minimum reflections and also at a constant span. Again two force sensors, in thrust and normal direction respectively, are used. The phase-locked approach allowed to visualize the development of the Leading Edge Vortex. It is found that a LEV is generated during the translational phase of the wing. This LEV is shed in chordwise direction and a new LEV is formed. This second LEV is not shed but interacts with the counter-rotating LEV from the mirror wing. This is in contrast to the insect flight, where only one LEV is formed during both in- and outstroke. The LEV shows a conical shape from inboard and outboard locations. At 86% of the span, the LEV is not visible anymore and possibly connected to the tip vortex. PIV measurements during clap and fling revealed the potential benefits of this mechanism. No upward flow is observed while the gap between the wings is closed due to the flexibility of the DelFly wings. Furthermore, the LEV stays closer to the wing. Both phenomena are possible reasons for an increased thrust of 8% of a pair of wings using clap-and-peel and an isolated wing. Wing deformation was studied by Groen [3] and Bruggeman [2]. Tests in normal air conditions and in vacuum conditions revealed the importance of both aerodynamic forces as well as the elastic-inertial forces. Comparing the test results under both conditions, the aerodynamic forces are found to yield heaving motion and chordwise deformation.

3.3.2 Performance improvements

Performance improvements were researched by Bruggeman [2]. His thesis entitled: *Improving flight performance of DelFly II in hover by improving wing design and driving mechanism*, was completely dedicated to performance improvements, specifically for hover conditions. The crank-shaft mechanism was redesigned, see figure 3.6. First of all an increase in thrust-to-power ratio of approximately 20%

(a) PIV setup as used by De Clercq [1]   (b) PIV setup as used by Groen [3]
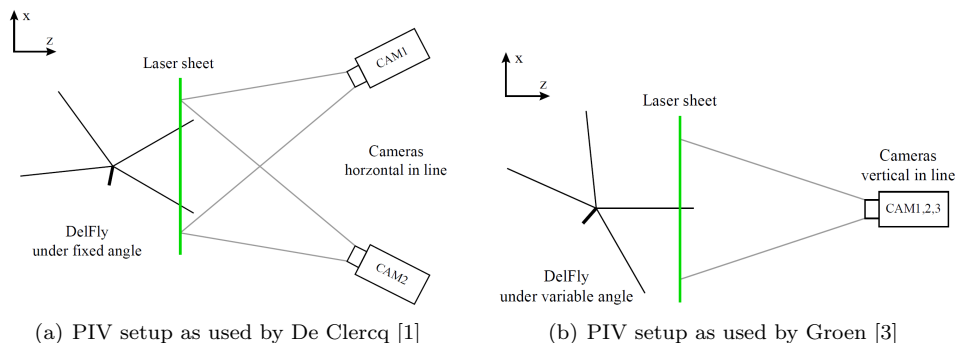
Figure 3.7 – *(a) Top view of the setup as used by De Clercq [1]. The cameras are placed horizontal and the laser illuminates from the bottom, (b) Setup as used by Groen [3]. The cameras are placed vertical and the laser illuminates from the bottom. Adapted from Groen [3]*

was obtained. Secondly, all parts are injection molded, yielding a much better reproducibility and smaller tolerances compared to the previous hand made gearbox. A smart design made it possible to make use of the same components twice (hinge, main gear and pushrod). As a consequence of the design, the total mass of the gear box has decreased with 35%. This means that less power is needed to sustain the flight of the DelFly. A systematic wing shape study was performed. The effect of the location and orientation of the stiffeners on the power consumption and the force generation was investigated. Second, the influence of the thickness of the stiffeners was researched. Carbon rods with a diameter of 0.28 mm were found to yield the best performance. Furthermore, the influence of the area distribution showed that a bat-like wing has a much higher thrust-to-power ratio. Finally, higher aspect ratio wings, with smaller area, show a better thrust generation at higher frequencies compared to the original improved wing. A schematic representation of the old wing with the new wing is given in figure 3.8. Groen [3] researched optimized wing designed by Bruggeman [2]. PIV results indicate a smaller LEV compared to the LEV of the original wing. However it remains unclear what the main reason is for a better thrust-to-power ratio. Similar to De Clercq [1], the inflight wing shape was determined for both wings. It turns out that the improved wing has a higher chordwise stiffness compared to the original wing. The improved wing shown in figure 3.8 increased the thrust-to-power ratio with approximately 5%. This yields in total an increase of 25% in thrust-to-power ratio. A comparison with the old and new wing and the old and new crank-shaft mechanism is shown in figure 3.9.
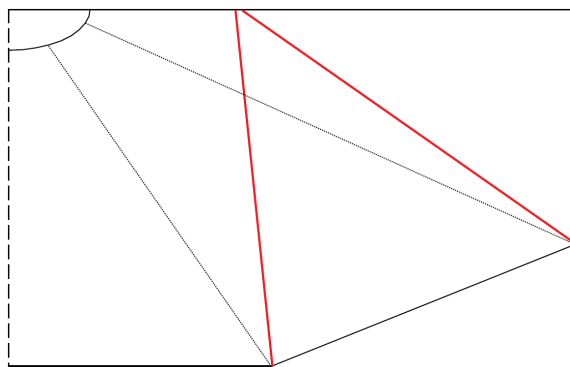
Figure 3.8 – *Schematic representation of the stiffener location and the old (gray) and new wing (red). Adapted from Bruggeman [2]*
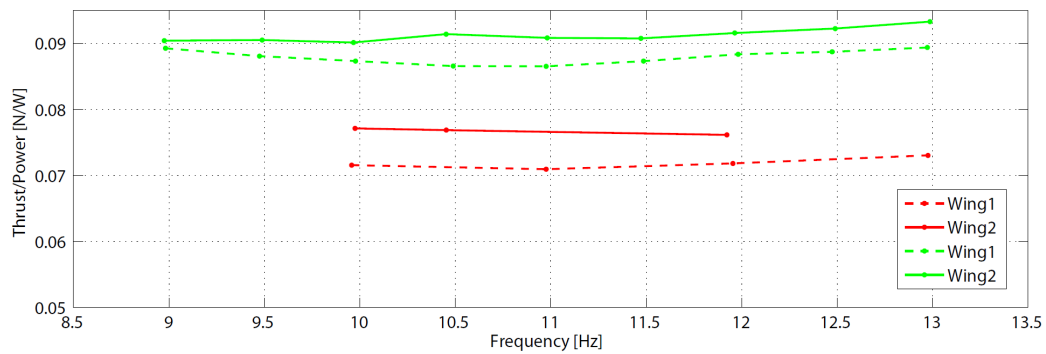
Figure 3.9 – *Thrust-to-power ratio as function of the flapping frequency. The green lines represent the new crank-shaft mechanism, whereas the red lines denote the old mechanism. The dashed line is the new wing and the solid line the old wing. Adapted from Bruggeman [2]*

Particle Image Velocimetry

4.1 Introduction

Particle Image Velocimetry (PIV) is one of the most succesful measurement techniques that has been developed over the last 20 years. Already a century ago Ludwig Prandtl made flow visualization experiments in a water tunnel in which he distributed small mica particles over the surface of the water. At that time only qualitative data could be extracted from the experiments. Today's progress in the fields of optics, lasers, electronics and computertechnologies made it possible to extract also quantitative information from the figures as Prandtl observed. This technique is called PIV. In comparison to other measurement techniques, PIV offers a lot of benefits. Contrary to the flow measurement techniques that have to interfere with the flow, such as Hot Wire Anemometry (HWA) and pressure measurements, PIV is a non-intrusive measurement technique. Moreover, PIV is capable of providing instantaneous flow information in a plane of volume whereas Laser Doppler Velocimetry (LDV) and HWA provide point wise information.Despite the numerous benefits there are also drawbacks regarding this technique. The main drawback compared to the other mentioned techniques is the lower temporal resolution (measurements per second). Whereas HWA and LDV offer a much higher temporal resolution, PIV is limited up to a few kilo Hertz. The temporal resolution is often limited by the camera read out speed and the laser repitition rate. Furthermore, PIV measures the flow velocity indirect. Particles should be able to follow the local flow velocity accurately.

The PIV technique will be the main measurement technique for this research, therefore some basic principles of PIV are discussed in this chapter. First of all the basic principle of PIV is given in 4.2. Furthermore, a short introduction on stereoscopic PIV, which is used in a time resolved mode in this research, is given in section 4.3. For a more complete review of PIV the reader is referred to Raffel et al. [40]. The practical implementation of the PIV technique is given in chapter 5.

4.2 Principles

An overview of a basic setup is given in figure 4.1. Tracer particles are seeded into the flow with a seeding generator. A measurement plane in the flow field is illuminated by a laser generating a circular light bundle in combination with dedicated optics. The scattered light from the tracer particles in this plane is recorded with a camera. Two laser illuminations short after each other (depending on the flow velocity) are recorded by the cameras. After recording, the image is divided in socalled 'interrogation

areas', small subareas in the image. Assuming that the particles in one interogation area have moved homogeneously between two laser pulses, the displacement vector in each interogation window can be determined with a statistical auto/cross-corration method. The local velocity vector can than be calculated by taking into account the time between the two laser pulses and image magnification.
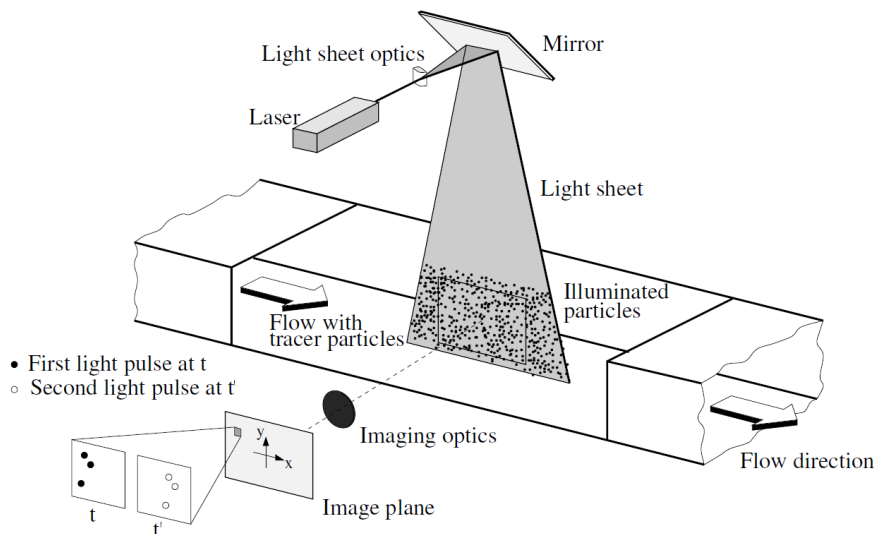
Figure 4.1 – *Basic layout of a PIV setup*

As mentioned earlier, PIV is a non-intrusive measurement technique. In order to satisfy this criterion, the tracer particles should not change the flow properties. In order to guarentee this, the ratio $m_{fluid}/m_{particles}$ should be kept small. For micron size particles, this ratio should not exceed 10^{-3}[41]. It is required that the tracer particles follow the local flow velocity vector accurately. In order to satisfy this condition, ideally the particles should have the same density as the fluid by which they are transported. For liquid flows this easy to obtain, whereas in gas flows it is not possible[41]. Furthermore, the response time of a particle to a change in flow velocity should be lower than the smallest time scale in the flow [41]. This might be challenging or even impossible in turbulent regions or in high speed flows with shocks where high velocity gradients are present. The particle response time to a step-wise variation in the flow velocity can be given as:

$$\tau_p = d_p{}^2 \frac{\rho_p}{18\mu} \tag{4.1}$$

For example, for a $1\mu m$ particle in a highly decelerating flow the response time is in the order of $10\mu s$. Therefore in gas flows, the particles need to be as small as possible in order to follow the flow accurately.

On the other hand, the light scattered by the particles should high enough to be visible in the recorded image. The scattering behavior of such small particles is linearly dependent on the particle diameter (according to Mie's scattering theory). Therefore, in order to record enough light the particles should be as large as possible. This yields a compromise between light scattering and fluid mechanical properties of the tracerparticles. The general rule is to use the largest particles possible, provided that they still follow the flow accurately[41]. The scattered light of a tracer particle also depends on the angle with which the camera is capturing. The scattering behavoir of a small oil particle in air is given in figure 4.2. This plot shows on a logarithmic scale the amount of light that is scattered in different directions. Unfortunately, the cameras in a PIV setup are often used in a side scattering mode, the direction in which least amount of light is being scattered by the particles.

Finally, also health reasons play a role in selecting tracer particles. Typical tracer particles in gas flows are water/oil based smoke particles or solid particles like titanium dioxide. When an open test section is used, as in the current research, titanium dioxide (with very good scattering behavior) is not

an option because it is potentially dangerous to human health when inhealed. These toxic particles might only be used when a closed loop wind tunnel is used.
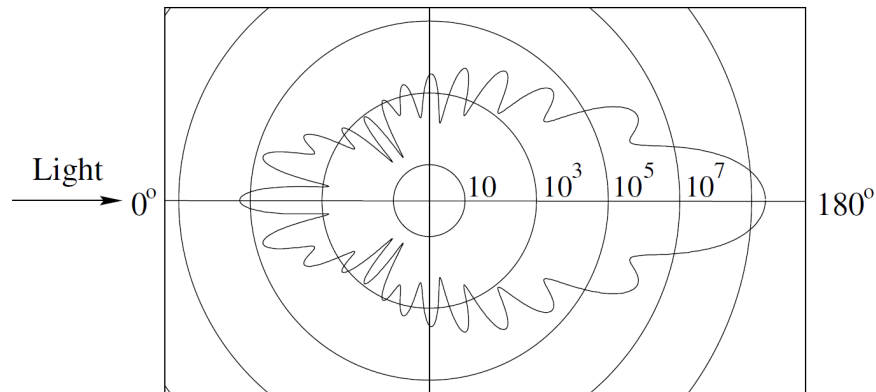
Figure 4.2 – *Scattered light by a 1 μm oil particle in air. Adapted from Raffel et al. [40]*

Settting up a good PIV experiment is a complex procedure, requiring expertise in laser light sheet positioning, seeding concentrations, image analysis[41]. Good optical access is a prerequisite for a PIV experiment. Both laser and camera need optical acces to the test area. PIV relies on the observation of the particle motion. For one velocity vector field, the tracer particles are illuminated twice. For each illumination pulse it is important that the maximum duration is limited. A too long illumination causes the particles to be displayed as streaks. Practically it means that the motion within the duration of the illumination pulse needs to be much smaller than the particle diameter itself. There are several possibilities for light sources. Both continuous and pulsed lasers have been developed. Currently, pulsed lasers are the standard light source in PIV equipment. The main reason being that the illumination pulse can be controlled very accurately. The most commonly used laser system in PIV is the solid-state frequency-doubled Nd:YAG laser. It emits laserlight at a wavelength of 532 nm. The energy in each pulse can range from 10 mJ upto 1 J. The pulse duration for this laser lies between 5 ns and 15 ns. This is sufficiently small enough for practical PIV, even in the hypersonic flow regions. However, the major drawback of the Nd:YAG laser is the relatively low repitition rate (10 to 50 Hz). This limits the possibility to do time-resolved PIV measurements to very low speeds (U¡0.2 m/s). To solve this problem, the diode pumped Nd:YLF laser is introduced. Siginificantly higher repetition rates can be achieved (1 to 5 kHz). However, the major drawback is the lower pulse energy (10 to 30 mJ) and a pulse duration which is ten times higher then the Nd:YAG laser. Despite these disadvantages, the Nd:YLF laser is currently the laser to use in the high speed PIV systems. When there is no need for high speed PIV, it is advised to use the Nd:YAG laser. This laser offers a much better illumination pulse which in turn allows to operate the cameras at a lower aperture number (i.e. less chance of peak locking).

Observation of the particle motion is nowadays done with digital cameras. The two main branches are the Charged Couple Device (CCD) and Complementary Metal Oxide Semiconductor (CMOS) cameras. The benefit of a CCD camera is the high spatial resolution at a relatively low frame recording rate. In turn, CMOS cameras have a much higher frame rate but at the cost of a lower spatial resolution. The latter are suited for high speed PIV application, whereas the CCD cameras are the option when normal PIV is performed. The complete imaging system consist of camera and lenses. There are a number of parameters that are important for the imaging system. The most important ones are the focal length f of the lens system, the aperture number $f_\#$ (focal length divided by the aperture diameter) and finally the image magnification factor (ratio of sensor size to field of view)[41]. Tracer particles are not imaged as spots due to their small size. The light is spread over a small spot as a result of diffraction effects. Due to diffraction effects the light is spread over a small spot. This diffraction effect largely determines the size of the imaged particle. It is known that the diffraction effect is linearly dependent upon the aperture number $f_\#$. Hence, a higher $f_\#$ leads to bigger imaged particles. In contrast with this requirement, the amount of recorded light decreases as the aperture number is increased. An optimum should be found for these two criteria. In order to calculate the velocity vector accurately, a

particle image of 2 pixels is favourable. In case the particle image diameter is much less than the pixel size on the camera, peak locking occurs (i.e. the velocity vector can only be determined in discrete steps).

In order to check whether peak locking occurs the PIV software Davis provides a histogram which shows the decimal values of each velocity component in the measurement data. The software provides a peak lock value, giving a measure of peak locking for a certain data set. It is calculated as:

$$peaklock = 4 \cdot (0.25 - com) \tag{4.2}$$

In equation 4.2, *com* is the center of mass of the histogram shown in figure 4.3. For no peak locking the peak lock value should be 0. A peak lock value of 1 indicates a strong peak locking effect. For the case shown below, the peak lock value is calculated as 0.12. Practically, a value less then 0.1 is an acceptable value.
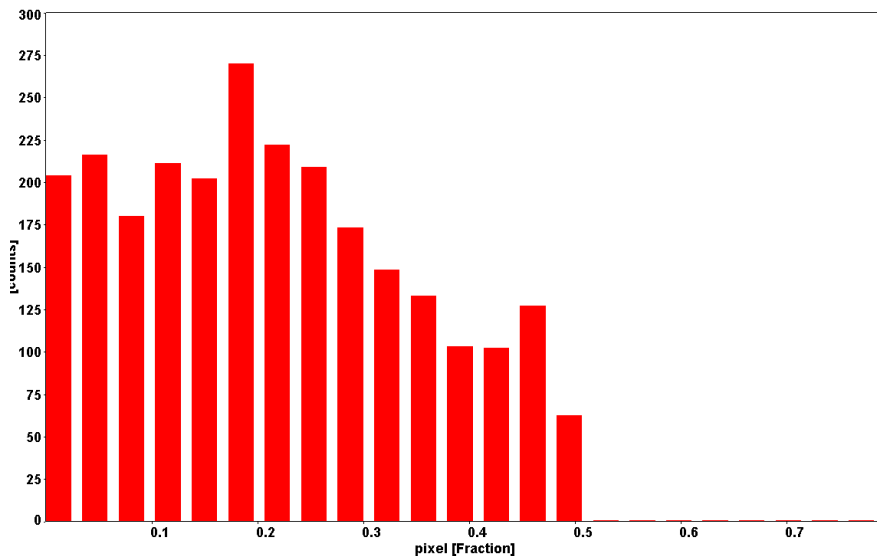
Figure 4.3 – *Histogram showing the decimal part of a particle displacements. The decimal values are presented*

4.3   Stereoscopic PIV

Up to now planar PIV has been discussed. Only the two velocity vectors in plane can determined with this technique. The third component is not only missing, but according to Raffel [40], the lack of this third component also introduces significant errors into the measurement of the in plane vectors, the so-called perspective error. The reason for this error is because the inplane particle displacement is correlated with the out of plane motion. This effect becomes especially dominant in case the flow is three dimensional. Several solutions have been proposed to measure the third component, one of them being stereoscopic PIV. In this research, this latter technique is used. Some basic principles belonging to this technique are discussed in this section. The basic layout of a stereoscopic PIV setup is given in figure 4.4.

To reconstruct the three velocity components basic geometric relations are used. The derivation here is shown for u, w, the v component follows the same derivation. The imaging of a particle in the light sheet on the camera sensor is schematically shown in figure 4.5. The image displacement (x_i to x_i') shown in this figure is related to the particle displacement ($[D_X \ D_Y \ D_Z]$) as:

$$x_i' - x_i = -M(D_X + D_Z \frac{x_i'}{z_0}) \tag{4.3}$$

Additionally, the angle in the XZ plane, between the light ray coming from the particle passing through

the lens center **O** and the Z-axis is given as:

$$\tan \alpha = \frac{x_i'}{z_0} \tag{4.4}$$

The velocity component measured by the left camera is then calculated as:

$$u_1 = \frac{x_i' - x_i}{M \Delta t} \tag{4.5}$$

Applying the above equations for both cameras, the u and w component of the velocity field are reconstructed as:

$$
\begin{aligned}
u &= \frac{u_1 \tan \alpha_2 + u_2 \tan \alpha_1}{\tan \alpha_1 + \tan \alpha_2} \\
w &= \frac{u_1 - u_2}{\tan \alpha_1 + \tan \alpha_2}
\end{aligned}
\tag{4.6}
$$
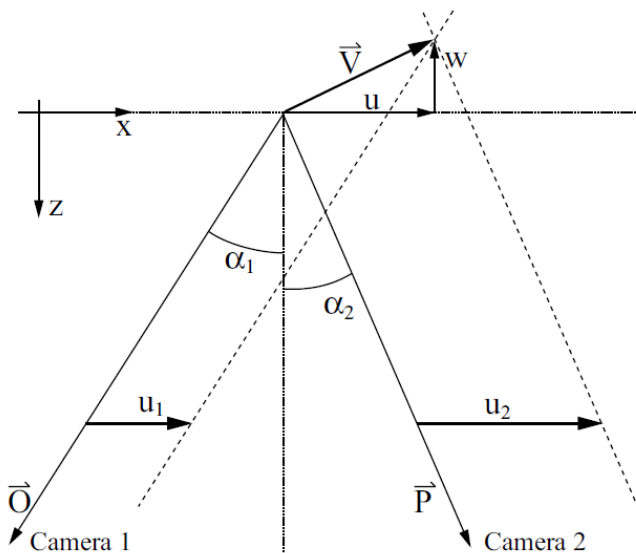
Figure 4.4 – *Stereo viewing geometry in the XZ-plane. Adapted from Raffel et al. [40]*
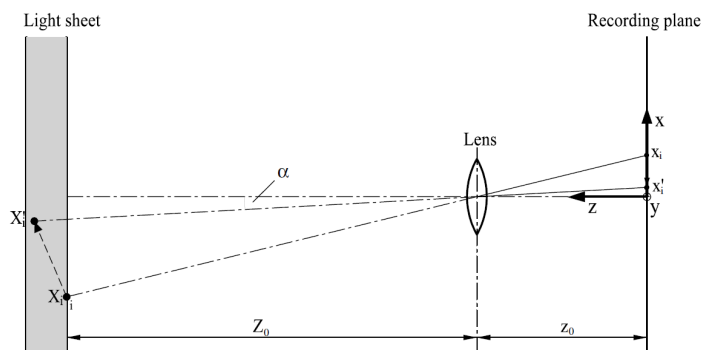
Figure 4.5 – *Imaging of a particle within the light sheet on the recording plane. Adapted from Raffel et al. [40]*

Both cameras are now looking under an angle towards the object plane. This means that the focal plane of the camera and the object plane are under an angle, resulting in a out of focus in part of

the image. The focal depth can be increased till everything is in focus but this decreases the amount of light. A Scheimpflug adapter is used which tilts the focal plane (by tilting the lens) such that the complete image is in focus again (Scheimpflug condition). Due to the oblique angle of the cameras with respect to the image plane, the recorded image will be distorted, the socalled perspective distortion. In order to reconstruct the local velocity vector the viewing direction and magnification factor for each camera must be known at each point in the recorded images[40]. For practical purposes a calibration plate with a very precisely known grid of dots on it is placed at the measurement plane(see figure 4.6). By taking images of this calibration plate the image dimensions can be related to the actual geometrical dimensions. A mapping algorithm is then used to calculate the mappings between image space and object space. By applying a multi-level calibration plate, the camera viewing angles can be determined which allows to reconstruct the three-component velocity vector[40].

The finite thickness of the light sheet poses some limitations on the obtainable spatial resolutions and also has a direct influence on the correlation peaks. Due to the finite sheet thicknes, the cross-correlation peak is smeared out into a ellipsiodal shape. Moreover, the oblique camera positioning causes the effective probe volume to be reduced. In order to increase the spatial resolution, the light sheet thickness should be reduced. However, this comes at the cost of a lower dynamic range for the inplane motion. As a practical rule, Raffel[40] suggests that the size of the interrogation area should be at least the same as the light sheet thickness.
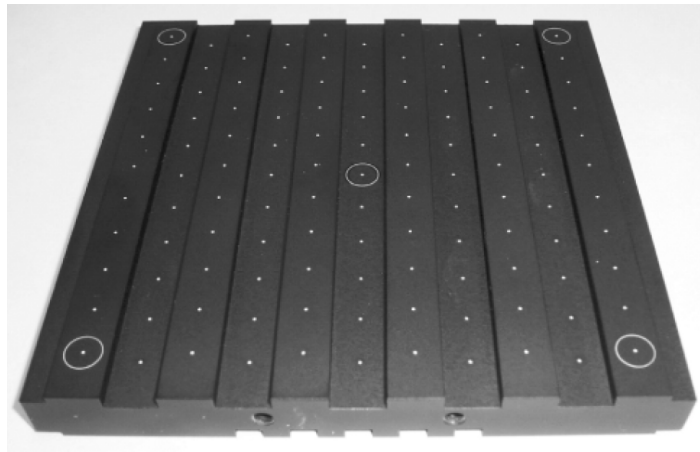
Figure 4.6 – *Precision-machined twin level calibration target with dot pattern for stereo PIV calibration. Levels are separated by 2 mm, dots are equally spaced on a 10 mm grid. Adapted from Raffel et al. [40]*

Although the previous described calibration procedure can be used to reconstruct the velocity vector in three dimensional space, there are limitations to this procedure. The procedure assumes that the calibration plate is perfectly aligned with the light sheet plane, which is practically almost impossible. Furthermore, vibrations or temperature changes during the measurements might cause misalignments during the measurements. Self-calibration or disparity correction is a procedure which can correct for these misalignments. The method is based upon actual PIV recordings. Basically the images of both cameras are dewarped according to the original projection coefficients and a cross-correlation is performed between images of each camera. The displacement data that results can be used to modify the mapping coefficients, thereby improving the alignment between the cameras.

Experimental Setup

The wake topology and the interaction between a flapping wing tail are discussed in chapter 2. Based on the previous discussion, it is shown that spatial reconstruction of the wake of a flapping wing has not been performed before. Furthermore, too little is known about the interaction between a flapping wing and a tail. Therefore, these topics are covered in the content of the current study. These are the two topics which resulted in a new experiment in which both aspects are researched. Both PIV and force measurements are used to investigate the wake topology and the interaction between flapping wings and tail.

The experimental setup is discussed in this chapter. First of all, the layout of the wind tunnel is discussed in section 5.1. Second, the balance system utilized in the experiments is described in section 5.2. Furthermore, the characteristics of the force sensor will be discussed in section 5.3. Details regarding the control of the DelFly are described in section 5.6. Finally, the PIV instrumentation and the relevant PIV settings can be found in section 5.4.

5.1 Wind tunnel

The wind tunnel used is a low speed wind tunnel. It is the W-tunnel at the High Speed Laboratory (HSL) of the Delft University of Technology (DUT). It is an open jet wind tunnel type, with a conventional setup. The flow passes a centrifugal fan ad goes through the plenum into the diffuser. After the diffuser the air enters the settling chamber, in order to decrease the turbulence level. Finally the air is accelerated in the contraction and is blown into the test section. Initially the test section used was a sqaure test section with 0.4m x 0.4m dimensions. However, for the current research a different contraction is designed with a square exit of 0.6m x 0.6m. The reason for this choice is the fact that in the smaller contraction, the free shear layers interact with the wake of the flapping DelFly. The maximum velocities that can be reached in the test section for the original and recently designed contraction are 35 and 15 m/s respectively. A detailed description of the design of this new contraction is given in chapter 6

For PIV measurements, particles are seeded into the flow at the inlet of the cetrifugal fan. A contraction nozzle causes the flow to accelerate and enters the tunnel nozzle, where the open test section is located. Therefore, if PIV is used, external ventilation is needed to filter the particles out of the air. Under certain conditions the turbulence level of the flow in the test section can be decreased to 0.5%. A figure with the general layout of the wind tunnel including the different components discussed before is given in figure 5.1.
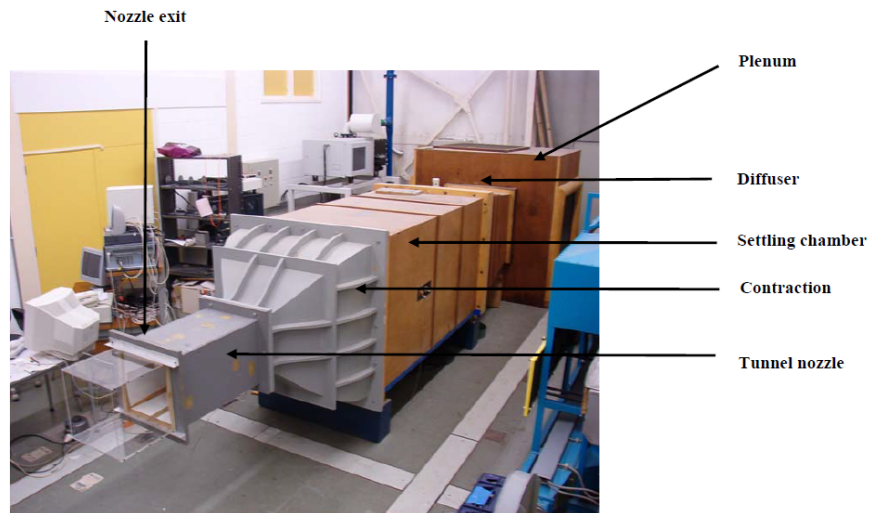
Figure 5.1 *– low speed open jet W-tunnel*

5.2   Support structure

The support used to keep that DelFly in a fixed position is shown in figure 5.2. In the present research forward flight is considered, resulting in the need for a support generating a miminum disturbance. The slender support guarentees a mimimum of flow disturbance and blockage effects are minimized. In previous researches, the mechanical resonance had a significant influence on the force measuremnts, [1, 3, 2]. By using this stiff designed support, it is supposed that the mechanical resonance is sufficiently far apart from the measurement range of interest. This is indeed confirmed by a frequency analysis in CATIA, indicating natural frequencies of a simplified support model of the system of at least 35 kHz.
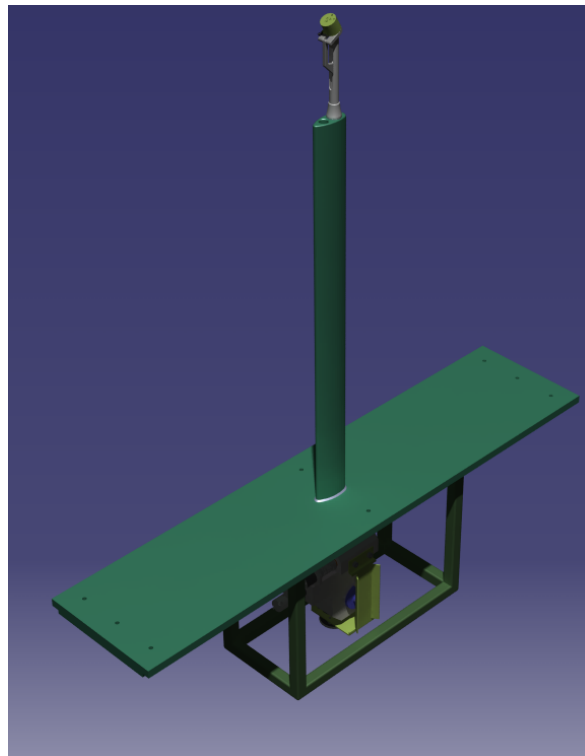
Figure 5.2 *– Balance system*

The balance is designed such that the Nano17 force sensor, see section 5.3, fits perfectly to the balance. The connection between the force sensor and the DelFly is custom designed. It is designed in a way that the x-axis of the force sensor is parallel to the fuselage. Furthermore, two servo motors are used for a pan-tilt mechanism. The force data acquisition software is extended with additional parts such that the yaw and pitch angle of the DelFly can be changed automatically.

5.3 Force sensor

The six component force balance Nano 17, build by ATI Industrial Automation, is put on top of the balance (see figure 5.3). It is chosen to use this sensor based on the very fine resolution and high resonance frequencies in all directions. This should eliminate the problem of resonance which Bruggeman[2] and Groen[3] suffered from. The dimensions, drawings and specifications of this sensor are given in appendix A. The Force sensor is connected to the PC via a Data Acquisition Card (DAQCard) from National Instruments (NI). It is the NI DAQCard-6036E which is a PCMCIA card with a 16-bit input- and output resolution. With this DAQCard the best resolution of the force sensor is obtained, which can be even be increased by use of filtering[1]. Furthermore a connector blok and cable are used in order to make the connection between the sensor and DAQCard. A picture of the force sensor is given in figure 5.3. The force data collection is controlled via a Labview program written by ATI Industrial Automation[2]. The collected data is sampled at a frequency of 25 kHz.

Figure 5.3 – *Nano 17, six component force balance.*

5.4 PIV

The PIV setup and the settings of the cameras and laser are discussed here. First of all the different components of the setup are described. Second, the system settings are given.

5.4.1 Seeding generator

A SAFEX fog generator is used to generate the particles used during the PIV experiments. This fog generator produces a non-toxic water-glycol based fog. The mean diameter of the generated particles is $1\mu m$. It turns out to be impossible to generate a homogeneous particle distribution while seeding the flow during the experiments. The reason for this being that at such low free streem velocities the fog generator does not provide a continuous seeding, but rather 'puffes'. Therefore, it is chosen to fill

---

[1] http://www.ati-ia.com/products/ft/ft_models.aspx?id=Nano17
[2] It can be downloaded from http://www.ati-ia.com/Products/ft/software/daq_software.aspx

the complete wind tunnel room uniformly with smoke before the experiment started. By doing so, it is possible to generate homogeneous seeding throughout the experiments.

5.4.2 Laser

A double pulse Nd:YLF laser of the type Quantronix Darwin Duo 527-80 is used. It is a dual oscillator/single head pumped Nd:YLF laser. Two independent oscillators allow to control the pulse separation and pulse energy completely. This laser emits light at a wavelength of 527 nm. The total energy per pusle is 50 mJ. The repitition rate varies from 0.1 to 10 kHz, making it suitable for high speed PIV applications. The pulse duration is 120 ns. The laser can be externally triggerd via TTL inputs.

5.4.3 Camera

HighSpeedStar6 cameras from LaVision have been used in order to make time resolved PIV possible. This is a highly sensitive 12 bit digital camera with a resolution of 1024 x 1024 pixels at frequencies upto 5400 Hz[3]. The camera uses a CMOS sensor chip with a pixel size of 20μm x 20μm and a total size of 20.48 x 20.48 mm^2. The internal storage capacity is 8 gigabyte. Via a gigabit ethernet connection the recorded data is transferred to the computer. The cameras can be controlled with the High-Speed controller

5.4.4 High speed controller

In order to control the triggering of both laser and cameras a High Speed Controller (HSC) is used. This HSC unit is provided by LaVision. The HSC is controlled by the Davis software. Pulse width and interval between pulses can be controlled accurately with this HSC. An external triggering is obtained from the DelFly micro controller board. When an external pulse of 5 Volts is received, the HSC starts to trigger both laser and cameras.

5.4.5 Software

The Davis 8.0.6 software is used to control the laser and camera setting, perform image analysis, data post processing and data displaying. A cross correlation algorithm is implemented in order to reconstruct the particle displacement between different images. Interrogation window sizes, overlap and number of iterations has to be set in this program. Furthermore custom algorithms written in Matlab are used to select the correct images for interpolation and to interpolate the data between the subsequent planes.

5.5 Laser and camera settings

5.5.1 Field of view, time separation and laser sheet thickness

The different settings of the cameras and laser are discussed here. In order to have wings during one flapcycle completely in the field of view (FOV), the field of view of the cameras has been set to 20 x 20 cm. With a semi-span of the DelFly of 14 cm, a maximum amplitude of 57 degrees of the upper wing and a maximum stroke angle of -28 degrees, a FOV of 20 x 20 cm guarentees that the wings are completely visible during one flapcycle. As a drawback of this size of the FOV, the spatial resolution of the velocity field will decrease.

---

[3]Recording frequencies upto 20 kHz are possible at a reduced resolution of 512 x 512 pixels.

The time separation between double exposure PIV images is chosen such that the majority of particles are observed in the same interrogation area of both images. By doing so, the number of particle pairs is sufficiently high enough to guarentee that the peak in the cross-correlation map corresponds to the actual particle motion. Loosing too much particle pairs dramatically deteroriates the cross-correlation map. It turns out that the height of the correlation peak is directly proportional to the number of particle pairs. Scarano [Reader] suggests a number of rules in order to increase the number of particle pairs. First of all the in-plane displacement should remain below 1/4 of the size of the interrogation area. Furthermore, the maximum out-of-plane motion should remain smaller then 1/4 of the sheet thickness.

In the present research the out-of-plane motion is significantly high compared to the in-plane motion. The reason for this specific setup is because the highest measurement resolution is required in the plane perpendicular to the free-stream velocity. As such the tip vortices can be resolved with enough resolution. To have enough particle pairs, the thickness of the laser sheet has been set to 3-4 mm. Taking the laser sheet thickness too small yields directly a smaller time separation. This has as a direct consequence that the dynamic range, especially for the in-plane motion will be diminished. Increasing the sheet thickness even further will increase the dynamic range. However, the energy intensity reduces proportional to the increased thickness. Particularly, the camera on the horizontal axis, shown in figure 5.6, which operates in side scatter mode will then receive too less light which makes cross-correlation impossible.

Based on the initial results, the time separation is chosen depending on the free-stream velocity and the chosen laser sheet thickness. For a free-stream velocity of $3\ m/s$

5.5.2 Particle image diameter

The optimum particle image diameter is about $2 - 2.5$ pixels. If the particle image diameter is below the size of one pixel, peak locking occurs. The position information can then only be determined in discrete steps. If, on the other hand, the particle image diameter becomes too big, overlap of separate particles might occur, yielding a decreased image contrast. Due to the small size of the tracer particles, the particle image is not given as a clear spot in the image. In fact, the effective particle image diameter is a combination of the geometric and diffraction effect, see section 4.3. The geometric part is described as:

$$d_{geom} = d_p M \tag{5.1}$$

Where d_p is the effective particle diameter (in this case $1\mu m$ particles) and M is the magnification factor given as:

$$M = \frac{d_i}{d_o} \tag{5.2}$$

In equation 5.2, d_i is the image size and d_o is the object size. It is calculated by taking the ratio of the FOV over the CMOS sensor size:

$$M = \frac{200 \cdot 200}{20.48 \cdot 20.48} = 9.77\ [-] \tag{5.3}$$

The diffraction diameter is given by:

$$d_{diff} = 2.44\lambda\left(1 + M\right)f_{\#} \tag{5.4}$$

In equation 5.4, λ is the wave length of the laser and $f_{\#}$ is the aperture number (given as the ratio of the focal length f over the aperture diameter D). Scarano [41] proposes that the effective particle image diameter is given as the Euclidean sum of the geometric and diffraction particle diameter:

$$d_{\tau} = \sqrt{\left(Md_p\right)^2 + \left(2.44\lambda\left(1 + M\right)f_{\#}\right)^2} \tag{5.5}$$

The wavelength λ for the laser is 532 nm. Furthermore, the aperture number is taken to be 2.8 for the camera placed on the horizontal axis and 4 for the camera looking from the top, see figure 5.6. The reason for this small aperture number is because of the amount of received light. Doubling the aperture number decreases the light intensity with a factor four. Substituting all the numbers into equation 5.5 gives:

$$d_\tau = \sqrt{\left(9.77 \cdot 10^{-6}\right)^2 + \left(2.44 \cdot 532 \cdot 10^{-9}\left(1 + 9.77\right) 4\right)^2} = 57 \left[\mu m\right] \tag{5.6}$$

In case the aperture number is 2.8, the effective particle diameter is 40 μm. Comparing the effective particle diameter with the pixel size (20 μ m) it is shown that the particle image size is approximately $2 - 2.5$ pixels.

5.5.3 PIV post processing tools

Image postprocessing is performed with Davis 8.0.2. Before correlation between the images is performed, a number of post processing steps are performed to enhance the particle visibility. First of all self calibration is performed for each measurement set[4]. This procedure corrects for any misalignment between the two cameras and the laser sheet, using actual particle images, see section 4.3. Especially the first planes downstream the trailing edge of the wings suffer from significant reflections caused by the wings. The general way to reduce the reflections is to subtract first a sliding minimum and then to normalize the intensity of the complete image. This sliding minimum filter finds a minimum over a specified scale length and subtracts that from the pixels in the same area. The result of this operation is that areas with substantial reflections are minimized and small particles are less affected. The second step is to normalize the intensity over the image. This procedure is repeated four times. During the third intensity normalization, the image is also Gaussian smoothed[5]. As a result of that, the particle diameter is increased. Measuring the peak lock value given by Davis (see section 4.3) confirms that by repeating the the operation four times with Gaussian smoothing in the third intensity normalization step indeed yields the best results in terms of peak locking.

The cross correlation between the double exposures is performed with a multi pass, multi grid interrogation function. In the first step the image is divided in interrogation areas of 128x 128 pixels with an overlap of 75%. In the subsequent steps the interrogation area is decreased to a 64 x 64 pixel size with 75% overlap. A benefit of this multi pass technique is the increased signal to noise ratio (SNR) due to an increased number of particle pairs in both windows.

The raw vector fields that are the result of the cross correlation still contain spurious vectors. Vector postprocessing is used to eliminate these. This phase consists of a few steps. Universal outlier detection, as described by Westerweel [42] and Westerweel and Scarano [43], is applied to remove the spurious vectors in the velocity fields. Furthermore, the data is Gaussian smoothed after the universal outlier detection is applied. The amount of smoothing is chosen based on a trade off between smoothness of the results and still keeping the small flow features that appear. To measure the effect of smoothing and outlier detection on the flow field, the circulation and peak out-of-plane vorticity of the upper vortex in a typical flow field are calculated (see figure 5.4). A small bounding box is taken around the core of the upper vortex. The circulation is calculated according to:

$$\Gamma = \oint_0^C \mathbf{V} \cdot \mathbf{dS} \tag{5.7}$$

The circulation is a good indication whether or not a vortex has lost strength due to the vector post processing method. Although the vorticity is closely related to the circulation, the peak out-of-plane vorticity still gives a good indication whether or not a vortex has diminished in peak vorticity, i.e. if the result is smeared out due to smoothing. The vorticity is calculated by equation 5.5.3. The vector

---

[4]So, a set of 12-18 planes
[5]With a filter size of 3x3 pixels

postprocessing parameters including the calculated circulation and peak vorticity values are given in table 5.1.

$$\omega = \nabla \times \mathbf{V}$$
$$\omega_z = \left(\frac{\partial v}{\partial x} - \frac{\partial u}{\partial y} \right) \tag{5.8}$$

-	1	2	3	4	5	6	7
Delete vector if peak ratio <	1.5	1.5	1.5	1.5	1.5	1.5	1.5
Fill up all	✓	✓	✓	✓	✓	✓	✓
Smoothing 3x3x3 (Gaussian)	1	1	1	1	1	1	5
			Universal outlier Detection				
Rem. ins. mode(remove and insert)	n/a	1x	2x	3x	3x	3x	3x
Eps [pix]	n/a	0.1	0.1	0.1	0.1	0.1	0.1
Remove treshold	n/a	2	2	2	2	2	2
Insert treshold	n/a	3	3	3	3	3	3
Neighbors	n/a	5x5x5	5x5x5	7x7x7	9x9x9	9x9x9	9x9x9
Minimum number	n/a	6	6	6	6	6	6
circulation $[m^2/s]$	97.22	97.27	97.27	97.27	97.26	97.26	96.37
peak vorticity $[1/s]$	0.186	0.188	0.188	0.188	0.188	0.188	0.135

Table 5.1 – *Post processing parameters for PIV images*
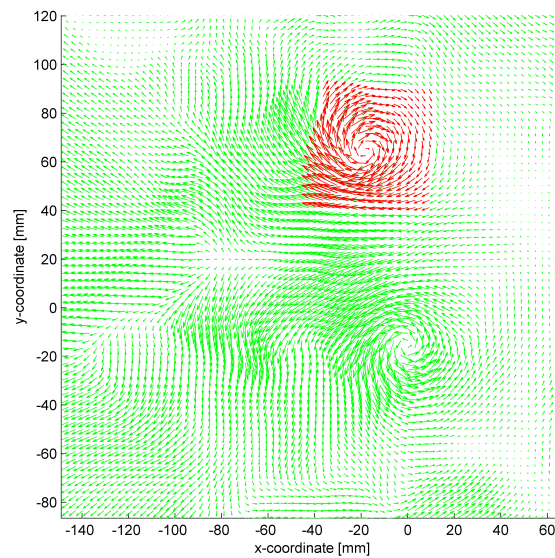
Figure 5.4 – *Example flow field used for post processing tests. Red vectors indicate the vectors that are used for calculating the circulation and the vorticity. The green vectors represent the rest of the flow field*

A complete overview of the different settings for cameras, laser and (post) processing parameters is given in table 5.2

		Camera 1	Camera 2	Camera 3
Camera settings	Resolution [$pixel$]	1024x1024	1024x1024	1024x1024
	Field of view [cm^2]	20x20	20x20	20x20
	Magnification factor	9.7	9.7	9.7
	Lens focal length [mm]	60	60	60
	Aperture number [$-$]	4	4	2.8
Laser settings	Pulse separation [μs]		175-250	
	Wave length [nm]		532	
	Repetition rate [Hz]		125, 250	
	Laser sheet thickness [mm]		3-4	
Post processing	Interrogation area [$pixel$]		64x64	
	Overlap [%]		75	

Table 5.2 – *Settings for cameras, lasers and post processing parameters*

5.6   DelFly control and Laser/Camera triggering

A custom designed micro controller board is used. Two micro processors are used to control the motor controller of the DelFly via a Proportional Integral Derivative (PID) controller and to sample different parameters (motor voltage and current) at a sampling frequency of 1860 Hz. The sampled data is sent to the computer via a serial connection. A separate program is used to control the flapping frequency of the DelFly with a PID controller and to log the data received from the micro controller board. The laser and cameras are externally triggerd with a 5 Volt signal coming from the micro controller board. This pulse is sent from the micro controller after 100 flapping cycles, to guarentee a steady flapping frequency. When receiving this trigger pulse, the PIV system starts to acquire data at a frequency of 250 Hz.

Furthermore, a connection is established between the micro controller board and the DAQ card of the force sensor. Besides logging the force data, additionally a seventh channel is logged. Motor pulses (5 Volts) and Hall sensors signals (-1.5 Volts) are combined in this signal. As long as the cameras and laser are not triggered, no motor pulses are logged. After 100 flapping cycles motor pulses, from which the first ones triggers cameras and laser, are logged. An example of the seventh channel signal, including the points at which a PIV image is taken, is shown in figure 5.5. Recording this seventh channel is important because the signal is used to reconstruct the phase of both wings in each PIV image. This is especially important because the images to reconstruct the 3D wake are taken from independent measurement sets. The determination of the phase is described in section 5.9.

5.7   Overview of the measurement setup

An overview of the camera and laser position is given here. The location and angles of cameras and laser is explained. A picture of the experimental setup is given in figure 5.6, a schematic overview of the setup is given in figure 5.7. Three cameras have been used during the experiments. The top two cameras have been used during tailless measurements. Because of their orientation, they are positioned in a forward scattering mode thereby increasing the light intensity of the particles. The angle between these two cameras is 40 degrees. For measurements with tail, the two left cameras have been used. These cameras are chosen in order to minimize the optical blockage due to the presence of the tail. The drawback of this setup is the fact that the third camera, placed horizontally, is operating in side scattering mode. The amount of received light from the particles is significant less in this position compared to camera two. The angular separation between these two cameras is approximately 40 deg.
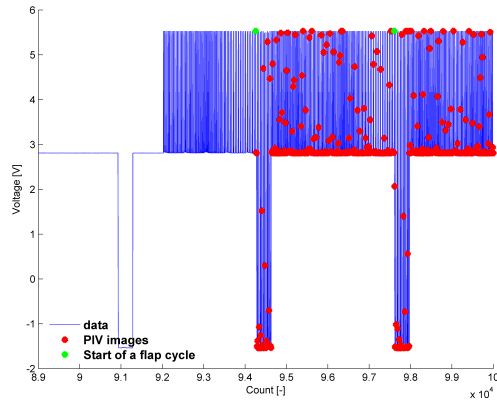
Figure 5.5 – *Example of signal as recorded in the seventh channel of the force DAQ card. The green dots indicate the start of a new flapping cycle, the red dots indicate the instance at which a PIV image is capture.*

(a) Side view   (b) Top view
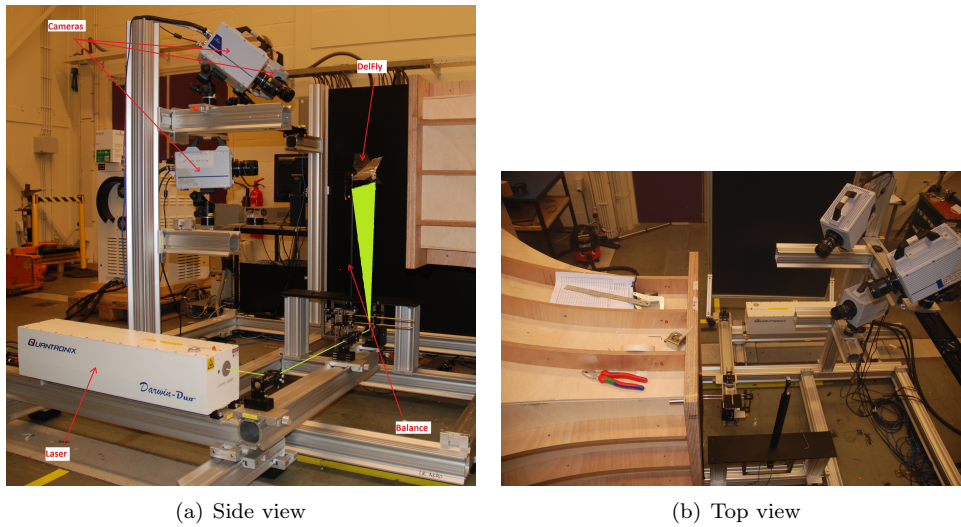
Figure 5.6 – *(a) Side view, (b) Top view of the experimental setup.*
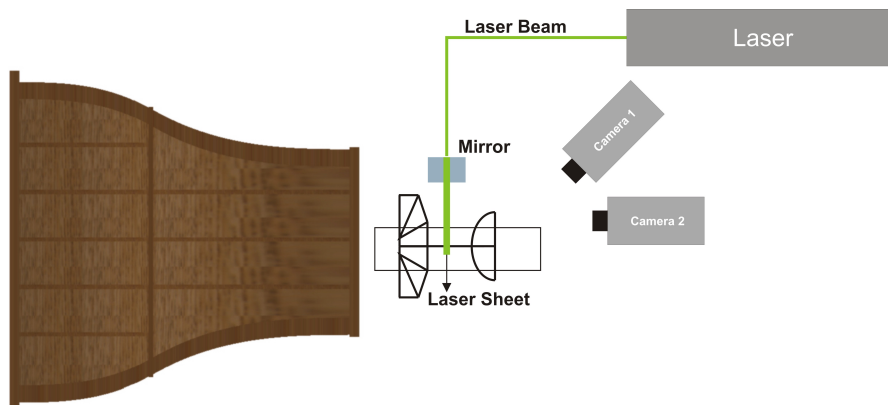
Figure 5.7 – *Sketch of the top view of the experimental setup*

37

5.8   Experimental campaigns

Previous researches focussed on the flow visualization in close vicinity to the wing for a tailless DelFly in hover conditions [1, 3]. In the current research, DelFly is tested in forward flight condition. Measurements are performed with and without tail. Time resolved PIV is used to record the wake of the DelFly. A number of parameters have been varied. These are listed below:

1. With or without tail

2. Forward velocity

3. Flapping frequency

4. Tail position with respect to the wings

5. Angle of attack of the DelFly

Experimental parameters are determined based on the estimated forward-flight regime of the DelFly. In order to assess the influence of a single parameter, it is varied while keeping the others constant. An overview of all tests is given in tables 5.3, 5.4 and 5.5.

Measurement [-]	Flapping frequency [Hz]	Forward velocity [m/s]	α [deg]	No. of planes [-]
1	10	3	0	12
2	10	4	0	12
3	10	5	0	12
4	10	6	0	12
5	7.5	3	0	12
6	12	3	0	12
7	8	3	5	12
8	10	3	5	12
9	12	3	5	12
10	8	3	10	12
11	10	3	10	12
12	12	3	10	12
13	8	3	15	12
14	10	3	15	12
15	12	3	15	12

Table 5.3 – *Measurement parameters for DelFly without tail configuration*

5.9   Phase determination

To determine the phase distribution of the DelFly accurately, a small experiment is performed. The DelFly is put in in front of a high speed camera. 1000 images are taken at an acquisition frequency of 2000 Hz. Furthermore, force data is acquired at a frequency of 25.000 Hz. A Matlab algorithm using functions from the Image Processing Toolbox is used to detect the leading edges in each image. First of all, the contrast is adjusted such that a bright image appears, which makes it easier to detect only the leading edges. As a second step, edge detection is used to detect the edges in the image. This method uses a socalled *Canny* method to detect edges. This method searches for maxima in the intensity gradients in the gray scale image. In general this filter is less sensitive to noise in the

Measurement [-]	Flapping frequency [Hz]	Forward velocity [m/s]	α [deg]	No. of planes [-]
16	4	3	0	12
17	6	3	0	12
18	8	3	0	12
19	10	3	0	24
20	12	3	0	12
21	10	5	0	12
22	10	6	0	12
23	8	2	0	12
24	10	2	0	12
25	6	3	5	12
26	8	3	5	12
27	10	3	5	12
28	6	3	10	12
29	10	3	10	21

Table 5.4 – *Measurement parameters for DelFly with tail at 3 cm behind the trailing edge of the flapping wings*

Measurement [-]	Flapping frequency [Hz]	Forward velocity [m/s]	α [deg]	No. of planes [-]
30	6	3	0	18
31	10	3	0	21
32	6	3	5	17
33	10	3	5	17
34	6	3	10	17
35	10	3	10	3

Table 5.5 – *Measurement parameters for DelFly with tail at 6 cm behind the trailing edge of the flapping wings*

detection of edges compared to the other methods that the Matlab toolbox provides. Furthermore, the Hough transform is applied. This is a method that can be used to detect various kind of shapes. In the present research, straight lines are detected. The Hough transform is a mapping from the image space (x, y) to the parameter space (θ, ρ). A straight line can be parameterized by two values (θ, ρ). θ is the angle with respect to the x-axis and ρ is the distance from the origin (see figure 5.8). The equation of a line can then be given as:

$$\rho = x \cos(\theta) + y \sin(\theta) \tag{5.9}$$

Restricting θ to the interval $[0, \Pi]$, the normal parameters for a line are unique. As such, the lines in the image space correspond to a unique point in the $\theta - \rho$ plane. Hence, this specific point in the $\theta - \rho$ plane defines the line through the colinear points. The complete image is mapped to this $\theta - \rho$ parameter space. A parameter space matrix with the rows corresponding to ρ and columns corresponding to the θ values is generated by Matlab. Peaks in this matrix corresponds to lines in the image space. The function *houghpeaks* identifies these peaks in the matrix. Finally, the line segments that are detected by the Hough transform, are extracted with the help of the function *houghlines*. While the start and end points of a detected line are given, it is easy to calculate the angle of the line
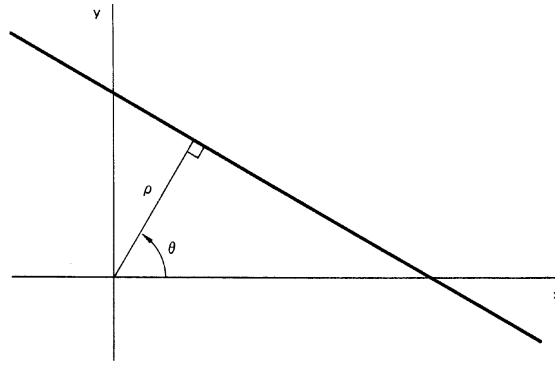
Figure 5.8 – *Polar representation of a line*

with respect to the horizontal axis as:

$$\phi = \tan^{-1}\left(\frac{y_{end} - y_{start}}{x_{end} - x_{start}}\right) \tag{5.10}$$

The algorithm is tuned such that the leading edges of both wings are reckognized. An example of such an image is given in figure 5.9. For most of the images this worked perfectly. In approximately 1% of the images, the wrong edge (one of the chordwise stiffeners) was detected. These specific cases are redone individually. The phase determination is performed for three different frequencies (6,8 and 10 Hz). The resulting phase distribution is shown in figure 5.10.
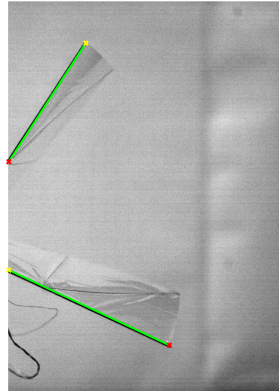
Figure 5.9 – *Example of detected leading edges during downstroke.*

Now the phase distribution over a flap cycle is determined, the phases of each image during the measurements needs to be determined. The data acquisition board of the force sensor has the capability of logging a seventh channel. As explained before in section 5.6, this signal contains the Hall sensor (-1.5 Volts) and the motor pulse signals (5 Volts). After approximately hundred periods of flapping, the first motor pulse is sent thereby triggering the cameras and laser. The data acquisition of the PIV starts when the first motor pulse is received. Afterwards this signal is used to determine the phase of each PIV image. For this a dedicated Matlab script is written in order to determine the exact phase of each PIV image. First of all, the start of each flap cycle is put at the first motor pulse which falls inside the Hall sensor pulse. The start of each pulse is determined based on this criterion. Because the acquisition frequency of the PIV is 100 times lower compared to the force data acquisition, one PIV image is taken every hundred force data samples. This is of course only true when both PIV and force data are acquired at the specified frequencies (which is assumed to be true). Combining the phase distribution determined before with the seventh channel of the force data, the exact phase

40
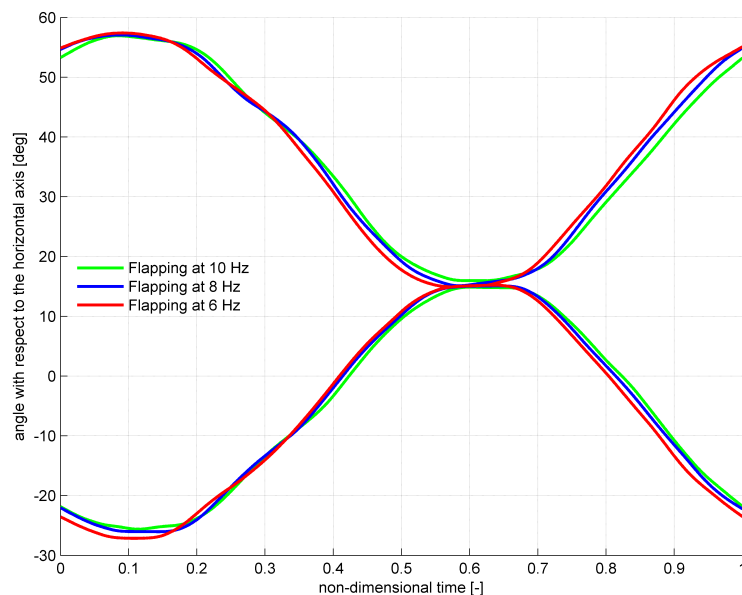
Figure 5.10 – *Phase distribution of the upper and lower wing during flapping for three different frequencies: 6,8 and 10 Hz.*

of each PIV image is determined. An example of the seventh channel signal, including the points at which a PIV image is taken, is shown in figure 5.11.
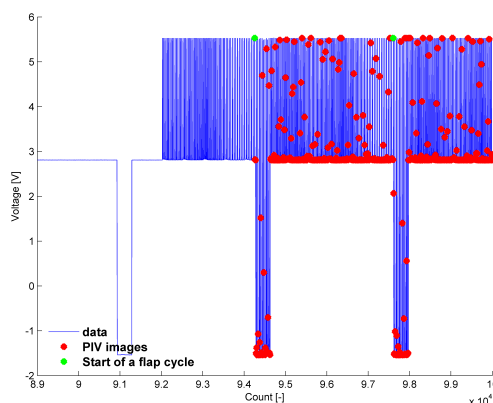
Figure 5.11 – *Example of signal as recorded in the seventh channel of the force DAQ card. The green dots indicate the start of a new flapping cycle, the red dots indicate the instance at which a PIV image is capture.*

5.10   Interpolation techniques

Now the phases of each PIV image are determined, the velocity field can be reconstructed by selecting the images from each measurement plane. The interpolation between the different planes is performed using a number of different methods. First of all, the standard interpolation routine from Matlab is employed. This *interp3* routine has capabilities to do nearest, linear, spline and cubic interpolation. The nearest interpolation takes the value of its nearest neighbour, linear interpolation fits a straight line between adjacent measurement points and returns the value on that line corresponding to the input value. Although cubic spline interpolation is more accurate, it is computational more expensive

compared to the linear and nearest interpolation methods. However, the Matlab intepolation times are in no ratio to the time needed for the kriging algorithm that is employed mainly for the current research. The table 5.6 gives an overview of the total duration one typical interpolation needs.

Interpolation method	Total time [s]	Relative time needed in comparison to *nearest*
Nearest	1.58	100 %
Linear	1.80	114 %
Cubic	8.03	508 %
Kriging	2,009.59	127,089 %

Table 5.6 – *Total interpolation time for different interpolation methods*

A completely different method that is chosen for interpolation is the kriging method. The theory behind this interpolation method is provided here to clarify the reason why kriging is chosen in comparison to the standard Matlab *interp3* algorithm. Kriging is a method that originated from the field of geostatistics. It is named after Daniel Gerhardus Krige who applied this technique first in the field of geostatistics. It is a robust and flexible technique to interpolate. The description given here is assembled from the work of Wikle and Berliner [44]. The description of this method corresponds to the kriging method applied in this research. Assume that there is a proces, an experiment or a simulation, of which we observe a a set of n values $\boldsymbol{y}_1, ..., \boldsymbol{y}_n$, then the kriging estimator of the unkown values $\mathbf{x}$ is given as:

$$E(\boldsymbol{x}|\boldsymbol{y}) = \boldsymbol{\mu} + \boldsymbol{K}(\boldsymbol{y} - \boldsymbol{H}\boldsymbol{\mu}) \tag{5.11}$$

Equation (5.11) predicts the new values $\boldsymbol{x}$ given the observed data $\boldsymbol{y}$. In (5.11) the $\boldsymbol{\mu}$ denotes the mean base term, which will be provided by the statistical mean of the observed values in the following. Furthermore, the matrix $\boldsymbol{K}$ is the gain matrix. It is given as:

$$\boldsymbol{K} = \boldsymbol{P}\boldsymbol{H}^T(\boldsymbol{R} + \boldsymbol{H}\boldsymbol{P}\boldsymbol{H}^T)^{-1} \tag{5.12}$$

This matrix is built up from a few different matrices. The matrix $\boldsymbol{H}$ is the observation matrix. This is a matrix containing zeros or ones. The function of this matrix is to select the observed points. The matrix $\mathbf{P}$ is the covariance matrix of the data:

$$P_{ij} = \sigma^2 \exp\left[-\sum_{d=1}^{3} \frac{h_{ij,d}^2}{2\theta_d^2}\right] \tag{5.13}$$

where σ is the standard deviation of the observed values. The correlation function $\exp[...]$ is a 3-dimensional Gaussian function, where the lag $h_{ij,d}$ is the spatial seperation between two observed values y_i and y_j in the direction of the spatial dimension d, and where the parameters θ_d are the correlation lengths. It is actually this correlation length θ which defines spatial extent of the influence of the neighbouring points on the new estimation. A low θ indicates that that only a few neighbouring points have a significant contribution, values far away from the new predicted point have a minor influence on the estimation. On the other hand, a high value of θ indicates that the impact of points further away is also taken into account. The correlation lengths θ_d can be estimated from the data using a Maximum Likelihood Estimate, however, this estimate comes at very high computational expense. Therefore, the correlation lengths θ_d are estimated from a Frequency-domain Sample Variogram, a new method for large data sets which is based on fitting a 3-dimensional Gaussian to the power spectrum of the data. As a second measure to reduce the computational cost, the Gaussian correlation function in (5.13) is approximated with a spline which is choosen to equal zero for $h > 5\,\theta$, as a result of which the matrices $\boldsymbol{P}$ and $\boldsymbol{K}$ can be stored in sparse form and also (5.11) can be computed by solving a sparse linear system.

The matrix $\boldsymbol{H}'$ is the transpose of $\boldsymbol{H}$ which selects the locations of the unknown values. Finally, the matrix $\boldsymbol{R}$ is the observation error covariance matrix, a diagonal matrix which contains the noise term. For the current appllication a constant error for each velocity component is assumed ($\boldsymbol{R} = \epsilon^2 \boldsymbol{I}$). Presently, the mean noise ϵ is determined from a brute force minimization of the cross validated RMSE. The cross validation is performed on a sub-domain of 5% of the total volume, choosen such that it maximizes the contained signal power. From this sub-domain, 5% of the observations are left out for cross validation, in 8 consecutive random draws.

Contraction design

Preliminary flow visualizations in the open test seciton of the W tunnel with cross-section dimensions of 400x400 mm revealed that there is an interaction between the flapping wings and free shear layers of the wind tunnel. Thus, it is decided to design a new contraction which ends in a test section with dimensions of 600x600 mm. In this chapter, the design process and the characteristics of the new contraction for the W wind tunnel are explained. The detailed drawings of the different parts are given in appendix C.

6.1   Design guidelines

The first parameter to be determined in designing a contraction is the contraction ratio (CR). It is defined as in equation 6.1, where A_{inlet} and A_{exit} denote the inlet- and exit area of the contraction respectively.

$$CR = \frac{A_{inlet}}{A_{exit}} \tag{6.1}$$

The inlet dimensions of the new contraction are $1.15m \times 1.15m$, which are the outlet dimensions of settling chamber of the W tunnel. The exit dimensions of the contraction are determined to be $0.6m \times 0.6m$, which allows to have 16 cm distance between the wing tips of the DelFly and the wall of the exit. Small triangular fillets are placed at the corners of the contraction inlet. These are used in order to lower the interaction between the two perpendicular boundary layers. Taking these fillets also into account, gives a resulting contraction ratio of:

$$CR = \frac{A_{inlet}}{A_{exit}} = \frac{1.15 \cdot 1.15 - 4 \cdot \left(\frac{1}{2} \cdot 0.1 \cdot 0.1\right)}{0.6 \cdot 0.6} = 3.62 \tag{6.2}$$

When the contraction ratio is set, the contraction contour and length are the parameters to be determined. Two design approaches are investigated in this research. Morel [45] provides an explicit approach for the shape of the contraction based on the flow uniformity at the exit and flow separation inside the contraction. Besides that, Mikhail [46] provides a design approach in which additionally the length of the contraction is minimized while keeping the flow uniformity high and flow separation to be absent. For the present case, minimum length is not of primary importance, because there is enough space for the contraction. Furthermore, the low contraction ratio justifies the use of a very simple cubic contraction design. It is therefore chosen to use Morel's method[45]. However, one should bear in mind that the boundary layer thickness is probably higher when using Morel's method compared

to the design approach suggested by Mikhail. This is because the exit boundary layer thickness is closely related to the length of the contraction. Morel's method is an iterative design approach taking into account four criteria:

1. Exit-velocity uniformity

2. Possibility of separation

3. Exit boundary layer thickness

4. Space/cost

The first two criteria are of primary importance in Morel's method. Nevertheless, special attention also should be given to the exit boundary layer thickness, which is a function of the length of the contraction. Excessive long contractions cause unacceptable boundary layer growth whereas short contractions might have thick boundary layers due to separation[45]. The general layout of a contraction proposed by Morel [45] is given in figure 6.1. It should not be forgotten that Morel's method is first of all applicable for axisymmetric contractions. However, Morel states that the method can also be used for rectangular sections for not too high aspect ratios where an equivalent diameter is used. This equivalent diameter is calculated as shown below:

$$D_{eq} = 2\sqrt{\frac{A}{\pi}} \tag{6.3}$$
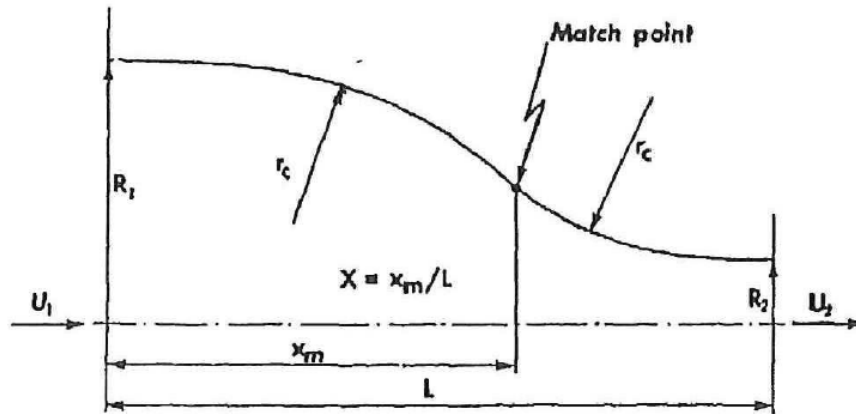
Figure 6.1 – *Wall contour constructed of two matched cubic arcs. Adapted from Morel [45]*

Due to the fact that Morel uses a cubic wall shape, the designer only needs to know two wall pressure coefficients[1]:

$$C_{pe} = 1 - \left(\frac{U_{2,\infty}}{V_e}\right)^2$$
$$C_{pi} = 1 - \left(\frac{V_i}{U_{1,\infty}}\right)^2 \tag{6.4}$$

The subscripts e and i refer to the point of maximum and minimum wall velocity. Choosing the values for these pressure coefficients beforehand and then using the design charts presented in [45] the contraction length and shape is determined. There are several criteria which the pressure coefficients in equation 6.4 have to satisfy.

1. C_{pi} has to be chosen such that separation is avoided near the inlet.

---

[1]For further details about the mathematical details behind this method, the reader is referred to [45]

2. C_{pe} is set such that the exit flow nonuniformity is below two percent.

The value for C_{pi} is based upon the Stratford criterion, which states that a turbulent boundary will separate when the following condition is met:

$$C_p \left(x \frac{dC_p}{dx} \right)^{\frac{1}{2}} = 0.35 \left(\frac{Re_x}{10^6} \right)^{0.1} \tag{6.5}$$

Morel [45] provides a number of approximations in order to calculate this upper bound for C_{pi}

1. Separation occurs at $0.95 C_{pi}$

2. The pressure gradient in equation 6.5 is approximated as the average pressure gradient between the points $C_p = 0.4 C_{pi}$ and $C_p = 0.8 C_{pi}$:

$$\frac{dC_p}{dx} \approx 0.4 \frac{C_{pi}}{s} \tag{6.6}$$

The distance s in equation 6.6 is read from a graph given by Morel (see 6.2).

3. The distance x in equation 6.5 can be given as the sum of two parts: x_0 is the distance from the last turbulence screen which is one meter in the current case. x_i stands for the distance from the contraction inlet to the wall pressure maximum, which is acquired from figure 6.3.

These approximations are used to find an upper limit for C_{pi}. Substituting the approximations into equation 6.5, the upper limit for the C_{pi} at the inlet can be rewritten as follows:

$$C_{pi} = 0.7 \left(\frac{x_0 + 0.9 x_i}{s} \right)^{-\frac{1}{3}} \left(10^{-6} Re_x \right)^{\frac{1}{15}} \tag{6.7}$$

The Reynolds number in equation 6.7 is based on the equivalent inlet diameter and the flow velocity at the inlet.

For the evaluation of Reynolds number, the inlet velocity is calculated by use of continuity equation based on desired test section free stream velocity of 3 [m/s]:

$$Re_{D_{eq}} = \frac{U_s D_{1,eq}}{\mu} = \frac{3 \left(\frac{0.6}{1.15} \right)^2 2 \sqrt{\frac{1.15^2}{\pi}}}{1.78 \cdot 10^{-5}} = 60,000 \, [-] \tag{6.8}$$

Assuming that the cubic matching point is located at approximately 40% of the total length ($X = 0.4$), the value for $x_i/D_{1,\,eq}$ can be determined from figure 6.3 to be approximately 0.16. From figure 6.2 the value for s/D_1 is taken as 0.09. Finally, x_0 can be non-dimensionalized as $x_0/D_{1,eq}$:

$$\frac{x_0}{D_{1,eq}} = \frac{x_0}{2\sqrt{\frac{A}{\pi}}} = \frac{1}{2\sqrt{\frac{1.15^2}{\pi}}} = 0.77 \, [-] \tag{6.9}$$

ll parameters in equation 6.7 are now known. Substituting all values into equation 6.7 yields the following upperbound for C_{pi}:

$$C_{pi} = 0.27 \, [-] \tag{6.10}$$

he pressure coefficient C_{pe} is easier to evaluate. According to Morel[45] this pressure coefficient mainly determines the flow nonuniformity. A relation between the flow non-uniformity and the pressure coefficient C_{pe} can be given as:

$$C_{pe} = 3\bar{u}_2 = 3 \cdot \frac{(V - U_c)_2}{U_{2,\infty}} \tag{6.11}$$

In equation 6.11 the flow non-uniformity is calculated as the difference between the wall velocity (V) and the velocity at the centerline (U_c), both at the exit, over the freestream velocity ($U_{2,\infty}$). For
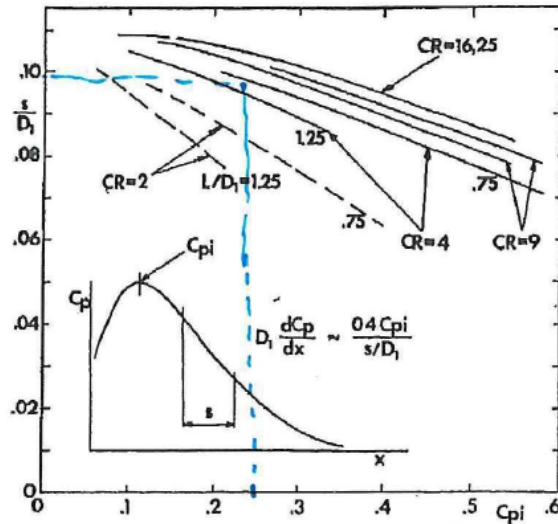
Figure 6.2 – *Wall pressure gradient. Adapted from Morel [45]*
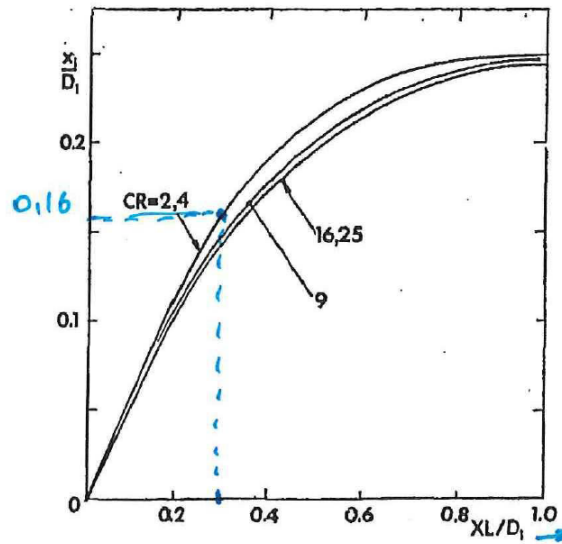
Figure 6.3 – *The distance from the contraction beginning to the wall pressure maximum versus the distance from the contraction beginning to the cubic match point. Adapted from Morel [45]*

practical purposes it is required that the non-uniformity remains below two percent of the free stream flow velocity. Hence, the value for C_{pe} should remain below 0.06

Now both values for pressure coefficients are chosen. Therefore the design chart from Morel[45] is used to determine the length and shape of the contraction. The contraction is presented in figure 6.4. The $L/D_{1,eq}$ ratio was chosen to be 1.1. The lines for this $L/D_{1,eq}$ have been drawn in blue in figure 6.4. In order to limit the chance of separation in the contraction, the inflexion point of the contraction is set at 40% of the total length. The total length of the contraction and the inflection point in meters from the inlet of the contraction is then:

$$L = 1.1 \cdot 1.30 = 1.43 \, [m]$$
$$X = 0.4 \cdot 1.1 \cdot 1.30 = 0.57 \, [m]$$

(6.12)

So the contraction contour is then described by the following equation:

$$f = 1 - \frac{1}{X^3}\frac{x^3}{L}, \; \frac{x}{L} \leq 0.57$$

$$f = \frac{1}{(1-X)^2}\left(1 - \frac{x^3}{L}\right), \; \frac{x}{L} > 0.57$$

(6.13)
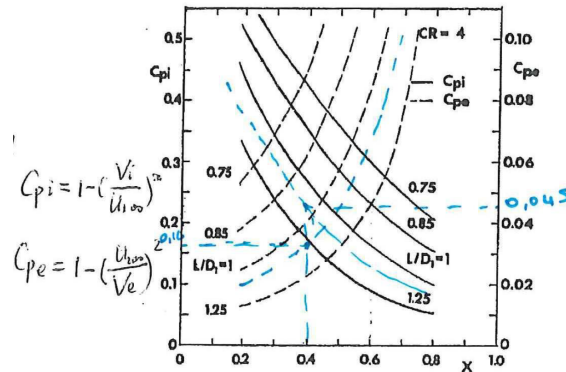
Figure 6.4 – *Design chart for CR = 4. Adapted from Morel [45]*

6.2 Final design

After completion of new contraction design based on Morel's method [45] and getting geometrical parameters, the technical drawings are prepared in Catia V5 for the manufacturing process. The layout of the designed contraction is shown in figure6.5. The contraction consists of three main frames and number of ribs in between them. Two frames at both ends of the contraction are manufactured from plywood with 40 mm thickness, whereas the frame placed at the inflection point to provide additional stiffness is manufactured from 18 mm thickness plywood. Ribs between the frames are CNC machined from plywood with a thickness of 18 mm. Flexible plywood with a thickness of 6 mm is bended inside the main frame of the contraction. Fillets are placed inside the contraction at the corners in order to prevent the interaction of boundary layers of the wall [4].

Figure 6.5 – *Layout of the contraction nozzle.*

The contraction is built in the workshop of Aerospace Engineering Faculty. It should be noted that due to time limitation with testing in the wind tunnel, the painting and sandpapering process of the contraction was not finished completely and will be completed after the measurements. Furthermore, small misalignments in the connection between the contraction and the settling chamber need to be corrected for in order to prevent early separation of the boundary layer.

6.3   Contraction characteristics

After putting the contraction in place, the characteristics of the contraction were tested. A hot wire setup was used in order to get free stream characteristics as well as the boundary layer profile. Hot wire measurements were acquired at a data acquisition frequency of 10 kHz. For the free stream characteristics the rotations per minute (RPM) of the fan is varied systematically, and the resulting velocity is measured with the hot wire setup, located approximately in the middle of the test section. Simple linear interpolation in Matlab provides the relation between the RPM and the free stream velocity (see figure 6.6).
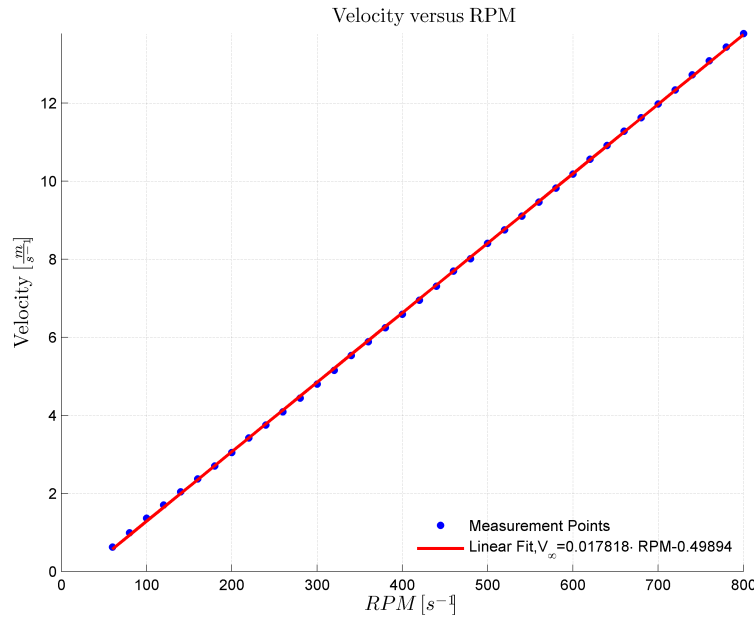
Figure 6.6 – *Free stream velocity versus RPM.*

The linear fit shows very good correlation with all measurement points. Hence this linear fit can be used as a relation between the RPM of the fan and the free stream mean velocity. Furthermore, the free stream turbulence intensity (I) can be determined from the hot wire results. The turbulence intensity is defined as the root mean square (RMS) of the velocity fluctuations u' over the average free stream velocity U_∞. The velocity fluctuations in 6.14 are calculated according to equation 6.14.

$$I = \frac{u'}{U_\infty} = \frac{\left(\frac{1}{n-1}\sum_{i=0}^{n}(u_i - U_\infty)^2\right)^{\frac{1}{2}}}{U_\infty} \tag{6.14}$$

The resulting free stream turbulence intensity for different flow velocities is given in figure 6.7. Low RPM however show a very high turbulence intensity. Most probably these can be dedicated to the fluctuations created by the fan. It can be seen that for RPM above 100 (U = 1 m/s) the turbulence intensity is measured to be typically 0.3%.

For a well-designed contraction, the exit flow velocity should be as uniform as possible. In other words, the velocity profile should be as flat as possible, i.e. the velocity reaches its free stream value just at the edge of the contraction. In order to test whether this conditions are also met in our design, the velocity profile over half of the test section is measured for two different velocities. The hotwire probe is placed initially one millimeter above the lower wall at the exit of the contraction. Furthermore, the boundary layer is measured. Because the boundary layer is relatively thin, the height of the hotwire probe above the lower wall is increased with half a millimeter each measurement. This allows to get a very accurate measurement of the boundary layer.
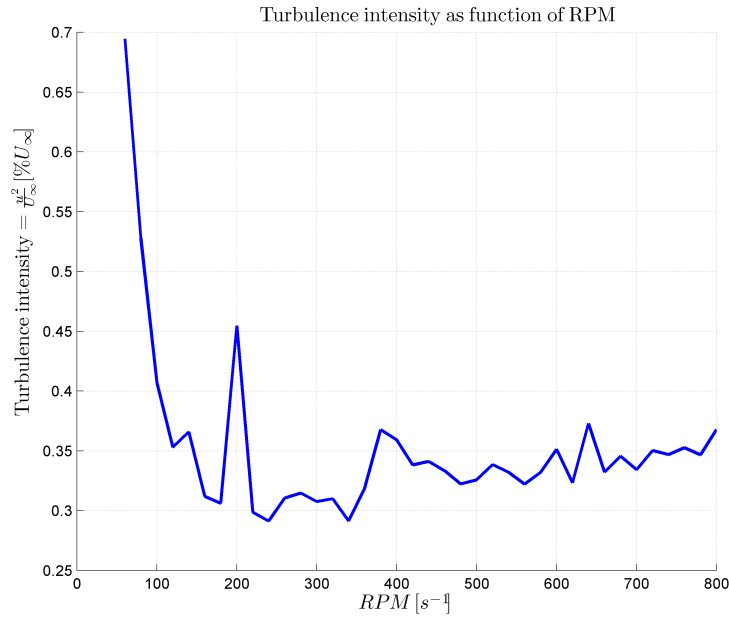
Figure 6.7 – *Free stream turbulence intensity versus free stream velocity.*

As a measure for the flow non-uniformity of the velocity profiles, equation 6.15 is used [2]:

$$\bar{u} = \frac{U_{min} - U_{max}}{U_{max}} \tag{6.15}$$

For 3 and 10 m/s cases, the non-uniformity is calculated to be 0.05 and 0.03 respectively. These values are a bit higher compared to the criterion of 2%, still they are in the same order of magnitude and found to be acceptable for the current type of research.

The boundary layer profiles for 3,5 and 10 m/s are presented in figure 6.8. The boundary layer thickness is evaluated by calculating 6.16:

$$\delta = \frac{u}{U_\infty} = 0.99 \tag{6.16}$$

The height at which this condition is met, is denoted as the boundary layer thickness. The resulting boundary layer thickness is also shown in figure 6.8. For the different free stream velocities the following boundary layer thickness is obtained:

$$\begin{aligned} \delta_3 &= 18\,[mm] \\ \delta_5 &= 14\,[mm] \\ \delta_{10} &= 6\,[mm] \end{aligned} \tag{6.17}$$

From figure 6.9 the turbulence intensities across the boundary layer have been calculated. For the 5 and 10 m/s case, it is clearly seen that inside the boundary layer the turbulence intensity is much higher compared to the free stream values. This phenomenon denotes the fact that the boundary layer is turbulent. Nevertheless, the 3 m/s case seems to be laminar.

---

[2]Note that this definition is slightly different compared to what Morel [45] uses
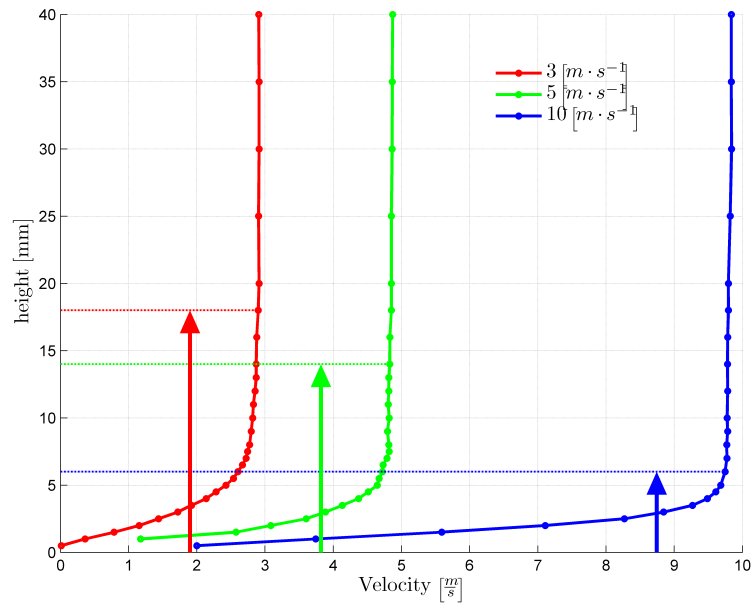
Figure 6.8 – *Boundary layer profiles at 3, 5 and $10\frac{m}{s}$.*
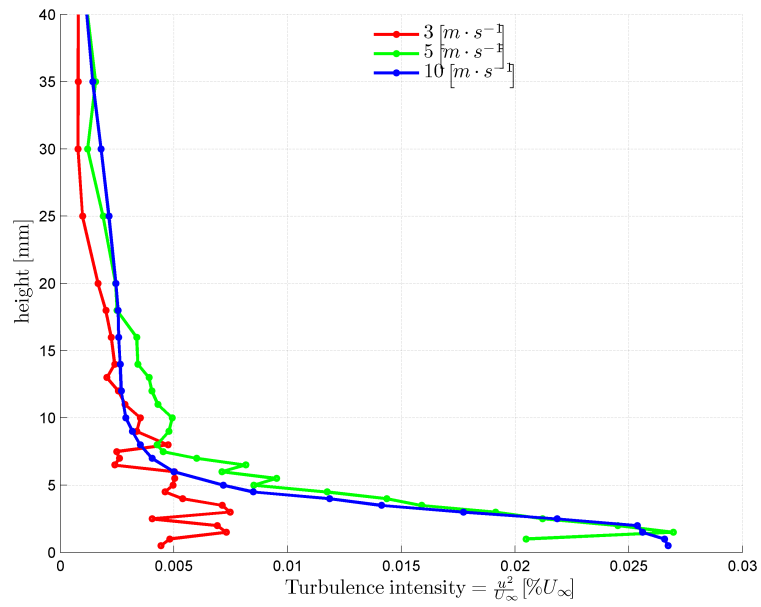
Figure 6.9 – *Turbulence intensity in the boundary layer profiles at 3, 5 and $10\frac{m}{s}$.*

51

Results

The results from the measurement campaigns described in chapter 5 are given in this chapter. First of all the results of the force measurements are discussed in section 7.1. Second, section 7.2 discusses the results of the interpolation techniques employed in the current research. Finally, time series reconstructions an spatial reconstruction are used to show the wake topology of the DelFly in section 7.3.

7.1 Force measurements on a forward flying DelFly

Simultaneous force measurements were performed with Stereo-PIV measurements. Analyzing the frequency spectrum of the force data reveals that there are still mechanical vibrations present in the signals. Additional force tests are done in order to discover the sources of these vibrations. It turns out that resonance frequencies of the DelFly itself are a significant problem. To get rid of these unwanted frequencies in the force signals, the results are filtered. A low-pass Chebyshev Type II filter is designed in the Filter Design & Analysis Tool of Matlab. The reason for this specific filter is that the signal is least affected up to the cut-off frequency and the attenuation of the signal after the cut-off frequency is strong compared to other filters. As a cut-off frequency 50 Hz is taken. The filter coefficients are optimized in order to preserve the power spectral energy contained in the frequecies below the cut-off frequency. For the current research, the lift force is defined positive upwards and the thrust force is positive in forward direction. An important problem with the force measurements captured simultaneously with the PIV measurements is that the captured force signals are biased. Based on these results, no conclusions can be drawn on the absolute force generation. To resolve this problem, different force measurements are performed which are correctly unbiased. The forces presented in this section are not correlated with the PIV results anymore. However they give a clear idea of the influence of different experimental parameters.

7.1.1 Influence tail on force generation

The influence of the tail on the lift and thrust production is shown in figure 7.1. First of all note that both thrust and lift for the tailed case show qualitatively the same behavior as in the tailless case. It is clear that both lift and thrust benefit from the presence of tail. For 0 degree angle of attack the tailless measurement should yields approximately 0 lift. This is as expected while the angle of attack of the DelFly remains zero. Hence the vertical forces generated on both wings cancel each

other. The average lift generated in the tailed case shows however the generation of positive lift. The reason for this is possibly because of the induced flow field by the flapping wings on the horizontal wing. As a result of that, the angle of attack of the horizontal tail is different from zero. Hence, lift will be produced by the horizontal tail. The results presented here are from the measurements done simultaneously with the PIV measurements. While the offset values of these measurements are not obtained in a proper way, the uncertainty in the absolute forces might be high.

(a) Lift force	(b) Thrust force
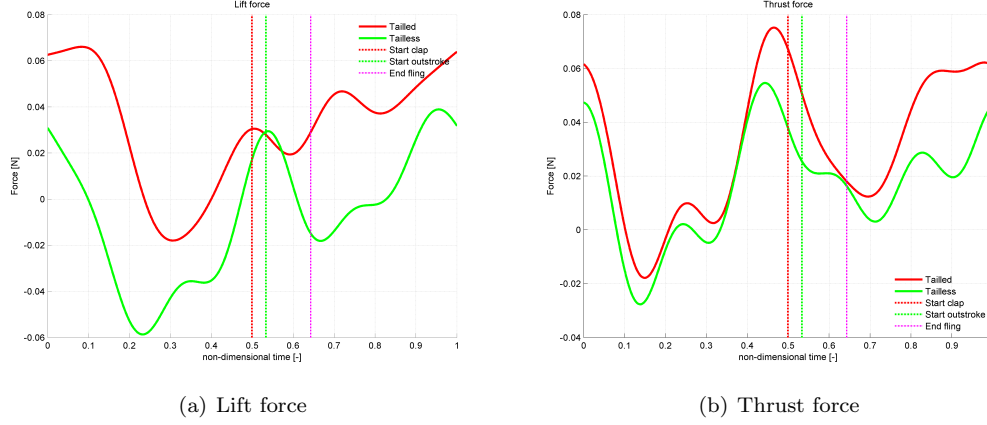
Figure 7.1 – *Lift and thrust force distributions for a DelFly flapping at 10 Hz. The forward velocity is 3 m/s and the angle of attack is 0 degree. The vertical lines denote the start of clap, start of outstroke and the end of fling respectively.*

7.1.2 Influence of flapping frequency

The results for a tailless DelFly flapping at different frequencies are shown in figure 7.2. Looking at the lift force results the lift is marginally increased when increasing the flapping frequency. Calculating the lift production over one flapping it is shown that the average lift production remains relatively constant, close to zero. This is because the angle of attack remains zero, yielding zero lift.

From the thrust force distributions a siginificant impact of the flapping frequency can be observed. Increasing the flapping frequency, the thrust production is significantly increased. By calculating the average generated thrust over the flapping cycle, it turns out that the 8 Hz case provides just enough thrust to sustain forward flight under this conditions. Increasing the flapping frequency yields a positive thrust generated under this condition. On the other hand, the generated lift is insufficient to keep the DelFly flying. Furthermore note that at higher flapping frequencies, the peak in generated thrust force increases in strength and shifts with respect to the lower flapping frequencies. It remains unclear upto now what the exact reason is for this phase shift.

7.1.3 Influence of angle of attack

When changing the angle of attack to non-zero values, the lift and thrust force do not coincide anymore with the f_x and f_z values as recorded by the force sensor. For an angle of attack (α) different from zero, the lift and thrust forces are calculated from the f_x and f_z as follows:

$$L = f_x \sin \alpha + f_z \cos \alpha$$
$$T = f_x \cos \alpha - f_z \sin \alpha$$

(7.1)

The lift and thrust distributions for an angle of attack variation of a tailless case are presented in figure 7.3. A general trend observed in the lift force is that the lift force increases significantly when the angle of attack is increased. The average lift increases from 0.02 ($\alpha = 0$ degree) to 0.16 N ($\alpha = 16$ degree). Note that the maximum lift generation occurs at the same time instance in the flap cycle. The reason for this increased lift at higher α's is that the wings not only generate thrust but

(a) Lift force
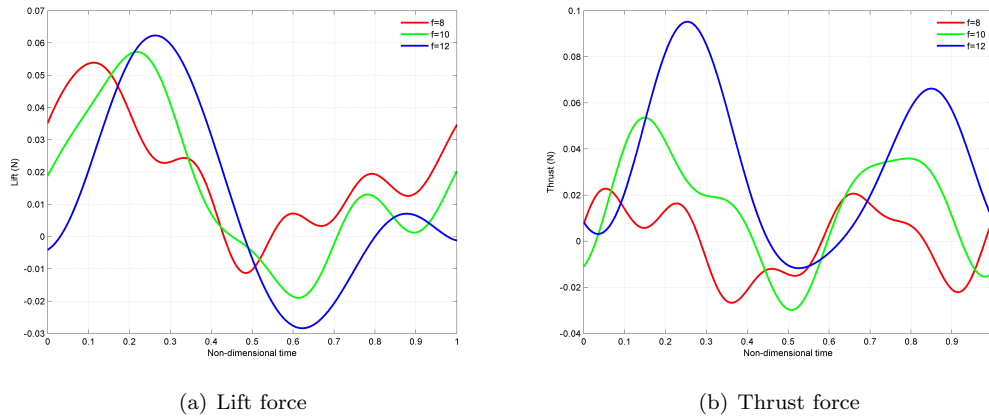
(b) Thrust force

Figure 7.2 – *Lift and thrust force distributions for a DelFly flapping at 8, 10 and 12 Hz. The forward velocity is 3 m/s and the angle of attack is 0 degree. The vertical lines denote the start of clap, start of outstroke and the end of fling respectively.*

additionally the inclination of the wings with respect to the free stream causes the generation of lift. Additionally, the force compomonent in forward direction attributes to the lift generation. At the same time however, the thrust force decreases with increasing angle of attack. This is mainly caused by the fact that the force component in direction of the free stream flow is lowered due to the increased angle of attack.

(a) Lift force
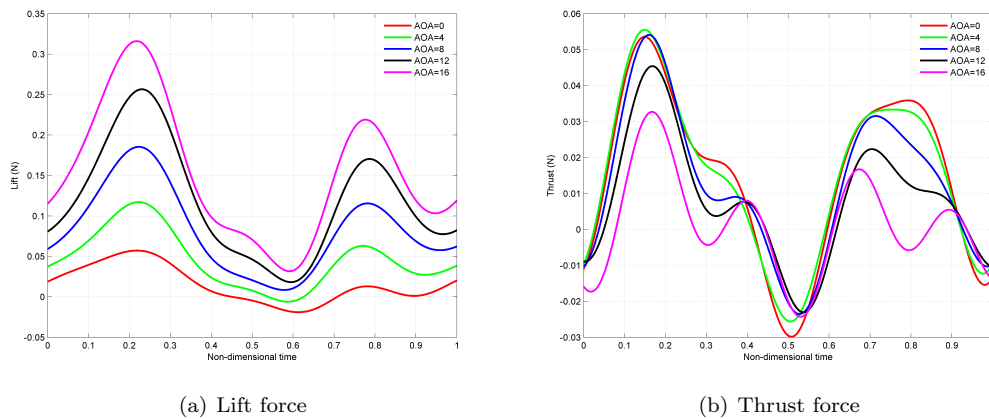
(b) Thrust force

Figure 7.3 – *Lift and thrust force distributions for a tailless DelFly flapping at 10 Hz. The forward velocity is 3 m/s. The angle of attack varies from 0 to 16 degree. The vertical lines denote the start of clap, start of outstroke and the end of fling respectively.*

7.1.4 Influence of forward velocity

The lift and thrust variation for different forward velocities are shown in figure 7.4. It is expected that almost no lift is generated when the angle of attack is kept 0. There are slight variations observed in the lift force distributions. The thrust force results indicate that an increasing free stream velocity decreases the produced thrust. For the 4-6 m/s cases, the thrust produced by the wings is just insufficient to overcome the generated drag on the complete DelFly. When increasing the forward velocity, the reduced frequency is lowered. As a result of the higher forward velocity, the effective angle of attack of the wings decreases. As shown in section 7.3, the vortical wake structures at higher free stream velocities are weaker. As such, the force produced by the wings will be lower. The oscillatory behavior of the thrust at higher forward velocities might be attributed to the higher vibrations of the

components of the DelFly.

(a) Lift force
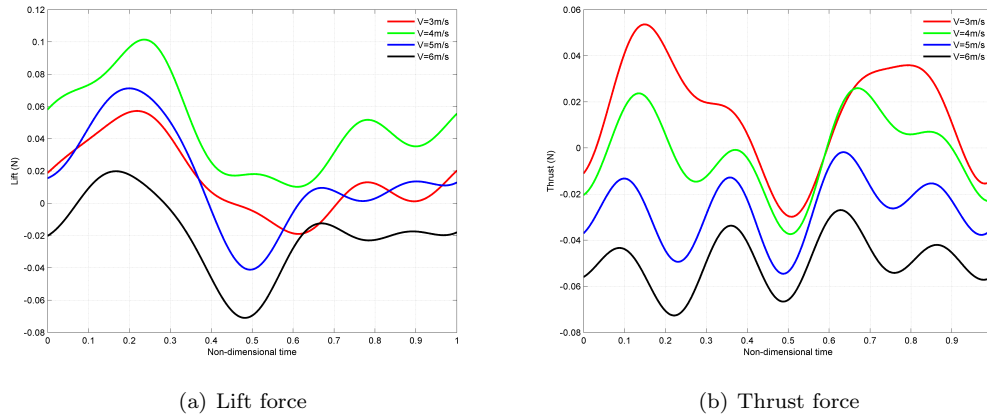
(b) Thrust force

Figure 7.4 – *Lift and thrust force distributions for a tailless DelFly flapping at 10 Hz. The angle of attack is 0 degrees. The forward velocity is changes from 3 to 6 m/s. The vertical lines denote the start of clap, start of outstroke and the end of fling respectively.*

7.2 PIV results

The PIV results are interpolated using the methods explained in section 5.10. The result of the different interpolation techniques is discussed here. Initially, the Matlab *interp3* algorithm is used to interpolate the results. As a main drawback however, an additional spurious vorticity layer is present in the vorticity magnitude at the edges of the flow field (see figure 7.5). The contribution comes mainly from the x and y component of the vorticity vector. Looking at the vorticity vector it is seen that the contributions arise from the velocity gradients in the z-direction ($\partial v/\partial z$, $\partial u/\partial z$), because of the velocity discontinuities from one plane to the other. On the other hand, kriging does not show these spurious vorticity layers because it provides a smoothed velocity field.

To decrease the noise level in the flow field, phase averiging is performed. Up to four images in each measurement plane are averaged and used for the spatial reconstruction. These results are compared with a kriging interpolation in which no phase averiging is applied, i.e. one image is used in each measurement plane. The results are shown in figurea 7.6-7.8. First of all, the tip vortices (TV)A in the phase averaged case are cleaner compared to the case without phase averaging. However, the noise is not significantly decreased. When comparing figures 7.6(a) and 7.7(a) with figure 7.8(a), it is clear that the kriging method provides a much cleaner picture of the tip vortices. The results show that the path of the TVs is consistent for the different interpolation methods. Because of the absence of the spurious vorticity layers and the smoothness of the results, kriging is be applied for the spatial reconstructions in section 7.3.

7.3 Wake reconstruction of a forward flying DelFly

The reconstructed wakes of DelFly, based on the kriging method explained in paragraph 5.10 are given here. Due to the limited time and space only a number of cases are presented. To see the influence of different parameters, a representative set of measurement sets is chosen. First of all the general wake topology is presented in section 7.3.1. Second of all, the effect of the flapping frequency is investigated in section 7.3.2. Third, the free stream velocity is changed for a DelFly with tail (see section 7.3.3). Finally, the influence of the angle of attack is researched in section 7.3.4.
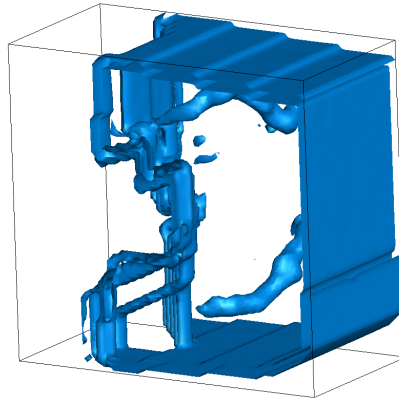
Figure 7.5 – *Vorticity magnitude for a times series representation. The spurious vorticity layers are clearly visible at the edges of the flow field.*

(a) Perspective view   (b) Side view   (c) Top view
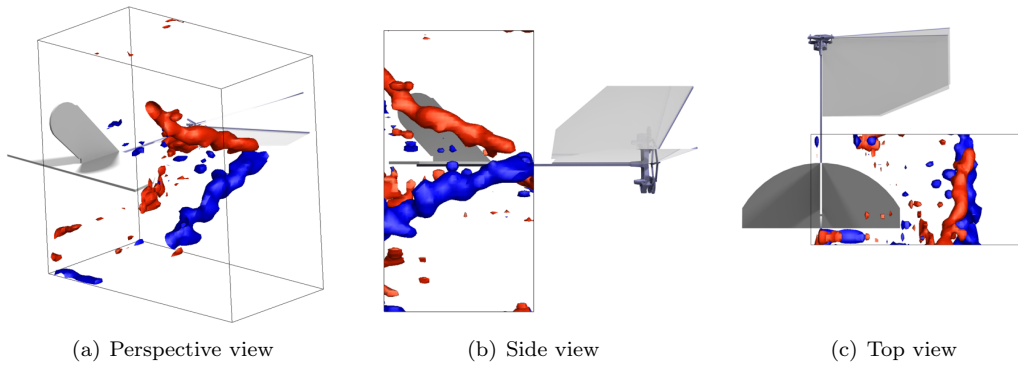
Figure 7.6 – *Spatial reconstruction of the DelFly wake using cubic interpolation. One image per measurement plane is used. The red and blue color indicate clock-wise and anti-clockwise vorticity respectively.*

(a) Perspective view   (b) Side view   (c) Top view
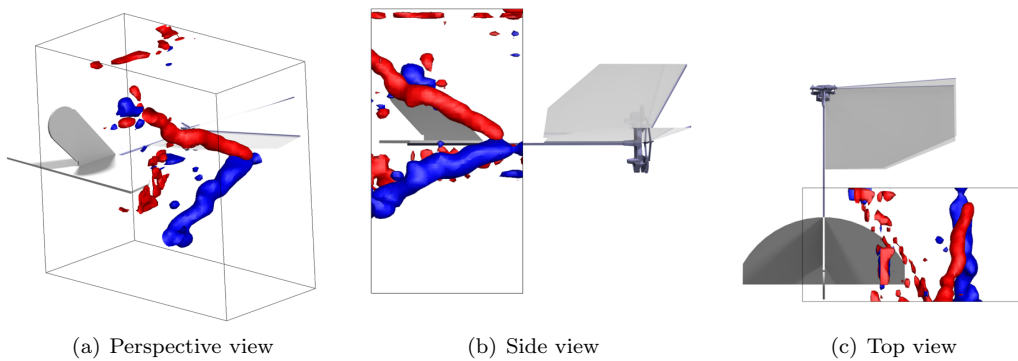
Figure 7.7 – *Spatial reconstruction of the DelFly wake using cubic interpolation. Phase averaging is applied with four images per measurement plane. The red and blue color indicate clock-wise and anti-clockwise vorticity respectively.*

7.3.1   Wake topology

As a first step, the wake topology is researched. What kind of vortical structures are present in the wake of the flapping DelFly? To answer this question, a spatial reconstruction of the DelFly wake is presented at 9 instances in the flap cycle. Furthermore, a time series reconstruction is used to verify the results obtained by the spatial reconstructions. In this case, the DelFly is flapping at 8 Hz, the

(a) Perspective view   (b) Side view   (c) Top view
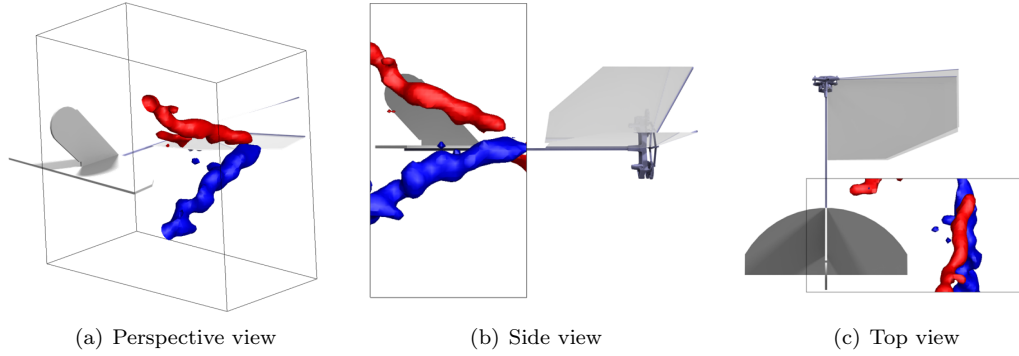
Figure 7.8 – *The DelFly is flapping at 8 Hz, the angle of attack is 0 deg and the free stream velocity is 3 m/s. The vortex wake is visualized by iso surfaces of absolute vorticity $\omega = \pm 0.11 s^{-1}$. The red and blue color indicate clock-wise and anti-clockwise vorticity respectively.*

free stream velocity is 3 m/s, the angle of attack is 0 degree and the tail is located 3 cm downstream the trailing edges. It should be noted that the region in the vicinity of the tail is masked during PIV processing due to intensive reflection underneath and lack of illumination above the tail. The lift and thrust forces which are generated during one flapping cycle including the points at which a visualization of the wake is reproduced is shown in figure 7.9.

(a) Lift force   (b) Thrust force
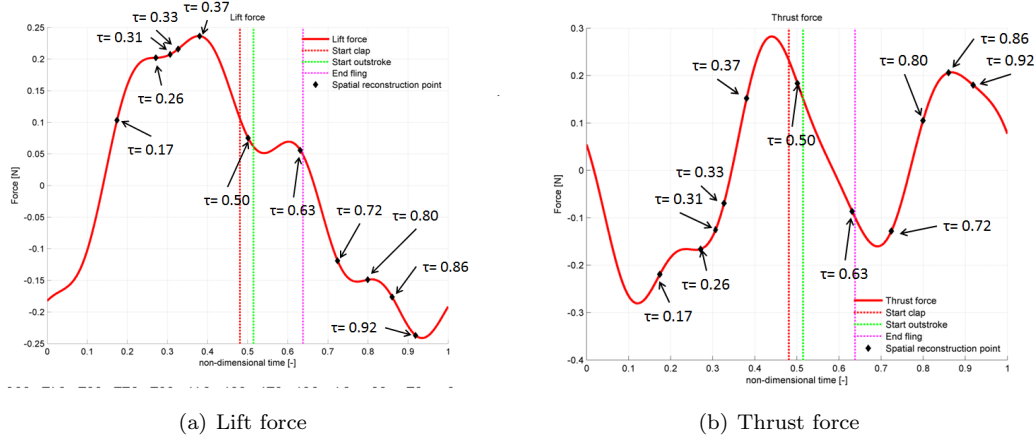
Figure 7.9 – *Lift and thrust force distributions for a tailed DelFly flapping at 8 Hz. The forward velocity is 3 m/s. The angle of attack is 0 degree. The vertical lines denote the start of clap, start of outstroke and the end of fling respectively. The instances at which a spatial reconstruction is given are denoted by blue dots.*

Furthermore, the direction and place of the vortices during the flap cycle are shown in figures 7.10, 7.11. For the rest of the discussion, the vortices have been labelled according to the labels assigned in the aforementioned figures. So the leading edge vortex that is developed during the instroke on the bottom wing is denoted as $LEV_{b,in}$, whereas the tip vortex generated during the outstroke on the top wing is denoted as $TV_{t,out}$. Similar notation is used for the other vortices generated during a flap cycle. Note that the definition of circulation states that counter-clockwise vorticity is defined positive. Additionally, it should be noted that the DelFly wings in the images are represented as rigid bodies as an indication of flapping phase but in reality there is a significant amount of deformation on the wings during the flapping motion (maximum trailing edge deformation with respect to rigid leading edge is 60% of the mean chord length [50]). Therefore, the position of vortical structures might seem to be uncorrelated with the position of the wings. In order to get an idea for the deformation of the wing, images from DelFly flapping in front of the camera are shown in appendix D. It is clearly seen that the wing deformation is significant, especially in during the translational motion of both instroke and outstroke. The start of the clap phase is shown at non-dimensional time instance $\tau = 0.50$, whereas

the end of the fling phase is shown at the non-dimensional time instance $\tau = 0.63$.

(a) Side view   (b) Back view
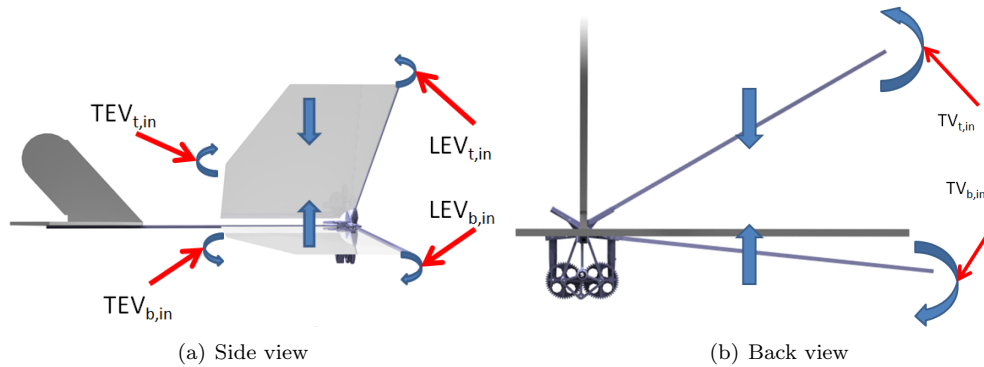
Figure 7.10 – *Vortex topology of the DelFly during instroke. Counterclockwise vorticity is defined as positive*

(a) Side view   (b) Back view
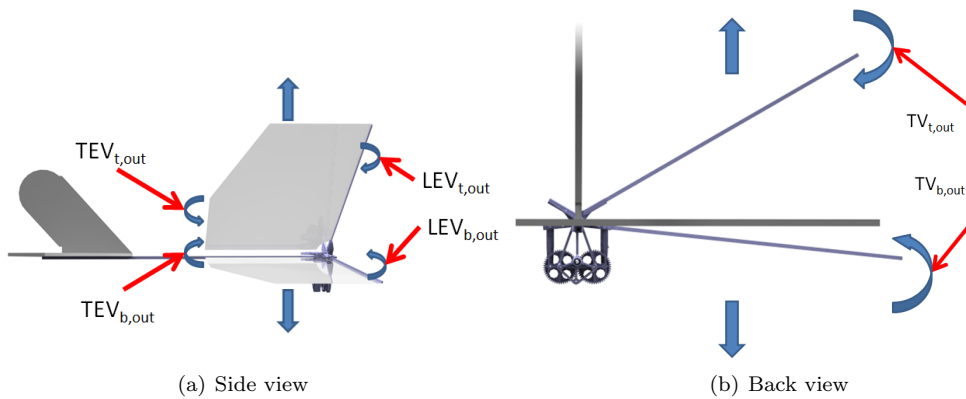
Figure 7.11 – *Vortex topology of the DelFly during outstroke. Counterclockwise vorticity is defined as positive*

The spatial reconstructions shown in the current section are compared with a time serie representation. In these time serie representation, the PIV images of one measurement plane are put in chronological order behind each other. The distance between the different planes is determined by the taking the average out of plane velocity in one plane multiplied with the known time separation between each PIV image. The first plane downstream the trailing edge is used to reconstruct this time serie representation. The presented times series shows the z component of the vorticity vector. The reason for this choice is because a shear layer (which is comparable to the one shown in figure 7.5) would make the results even more unclear in case the vorticity magnitude is presented. The evolution of the TVs during one flapping cycle is presented in figure 7.12. When looking at this figure, the following observations are made. It is clearly visible that the TVs generated during outstroke are less strong compared to the TVs generated during instroke. Moreover, the $TV_{t,out}$ is less coherent compared to the $TV_{b,out}$. While the $TV_{b,out}$ still continues, the $TV_{t,out}$ is already shed. At the end of instroke, there is an interaction between the TVs from both wings. Both TVs diminish each other in strength. While the $TV_{b,in1}$ is stronger compared to the $TV_{t,in1}$, the latter one is completely dissipated whereas the first one continues to be shed even when the outstroke phase already starts. The results indicate that there is a connection between the $TV_b, in1$ and the TV_t, out. Observe furthermore that root vorticity is shed at the start of instroke on both wings. No root vorticity seems to be developing during the outstroke phase. The reason for this behavior is because the wings are closely together during the start of outstroke.

From the spatial reconstructions shown in this section one can make the following observations. First of all note that the start of the flapping motion is defined as the start of instroke. As the reconstructed

volume starts 10 mm downstream of the trailing edge, it takes time to observe stroke reversal structures inside the measurement volume. The iso-surfaces of vorticity magnitude at the non-dimensional time of 0.17 are shown in figure 7.13. Two tip vortices generated during the previous outstroke are present in the reconstructed volume at this time instant. The $TV_{t,out}$ is already shed while the $TV_{b,out}$ is still visible throughout the flow field (see figure 7.13(b)). It is clear that the lower tip vortex ($TV_{b,out}$) is stronger and more coherent than the upper tip vortex ($TV_{t,out}$) which has a swirling shape. It is possible to state that the vortical structures are asymmetric which can be attributed to the dihedral angle of the wings. The results suggest that at this time instance a vortex pair is developing at the trailing edge of the top wing (see figure 7.13(a)). This feature is also visible in figure 7.14(a). A close inspection of the flow field in this region reveals that these features arise from severe reflections of the laser light at the wing trailing edge. Moving to the next time step the TEVs become visible on both wings (see figure 7.15). At $\tau = 0.33$, the connection between the TVs and TEVs on both wings is clearly observed. Moving to the next time instance ($\tau = 0.37$), U-shaped vortical structures appear on both wings (see figure 7.17). These vortical structure are formed by TVs, TEVs and RVs. When the clap phase starts ($\tau = 0.50$, figure 7.18), these U-shaped vortical structures disappear again. The RVs ($RV_{t,in}, RV_{b,in}$) observed in figure 7.17(a) are relatively weak and are most probably dissipated when convected downstream. The next time instance $\tau = 0.50$, the clap phase starts. The connection between both TVs and corresponding TEVs remains clear (figure 7.18(a)). An additional vortical structure is visible in figure 7.18(a) ($TEV_{t,in2}, TEV_{b,in2}$). The rotational direction of these structures is the same as the TEVs of both wings. Therefore, these are most probably secondary TEVs shed during the instroke. In the following figures, the outstroke phase of the flapping motion is examined. In the first time step ($\tau = 0.63$), which is the end of fling phase for the wings, upper and lower tip vortices of the previous instroke are being convected downstream (see figure 7.19). Contrary to the start of instroke, a trailing edge vortex is generated only at the outer part of the wing as the inner parts (closer to root) are still attached to each other (see appendix D). Moreover, there is only one trailing edge vortex emanating from the top wing ($TV_{t,out}$). Ideally, no starting vortex is expected to be generated in the clap-and-fling type flapping motion as the bound vorticity of each wing acts as the starting vortex for the other.

While the LEV is still growing, trailing edge vorticity is generated. Moving to the next time instance (see figure 7.20), the TVs from the instroke are convected downstream and the $TEV_{t,out}$ further develops. No TEV is visible yet on the bottom wing. This changes when the wings are at 2/3 of the outstroke (figure 7.21). On both wings, trailing edge vorticity is shed into the wake ($TEV_{t,out}, TEV_{b,out}$). Both of them are tightly connected with the TVs generated during outstroke. Furthermore, the $TEV_{b,out}, TEV_{t,out}$ are connected to weak RVs, $RV_{t,out}, RV_{b,out}$ (see figure 7.21(c)). When looking at the wing deformation at this time instance (see appendix D) it becomes clear that these RVs are formed at the start of the tapered parts of the wings. Moving towards the end of the outstroke (figure 7.22), the TVs of both wings are fully developed. There is still a connection between TV_b, in and the $TV_{t,out}$. This observation is consistent with the behavior of the time series results as shown in figure 7.12. Moving to the last time instance (see figure 7.23), both $TEV_{t,out}, TEV_{b,out}$ are connected to both $TV_{t,out}, TV_{b,out}$ respectively. From figure 7.23(b) it is observed that the $TV_{t,out}$ is less strong compared to the $TV_{b,out}$.

(a) Perspective view   (b) Side view
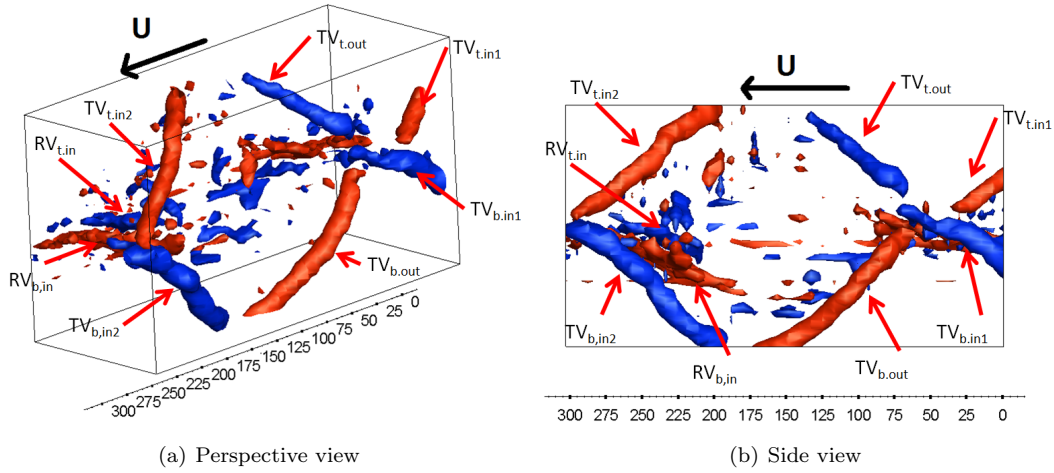
Figure 7.12 – *Time series representation of the DelFly wake flapping at a reduced frequency of 0.34. The iso values for the z-vorticity are chosen as: $\omega_z = \pm 0.10$. The blue color indicates clockwise z-vorticity whereas red surfaces indicate counterclockwise z-vorticity.*

(a) Perspective view   (b) Side view   (c) Top view
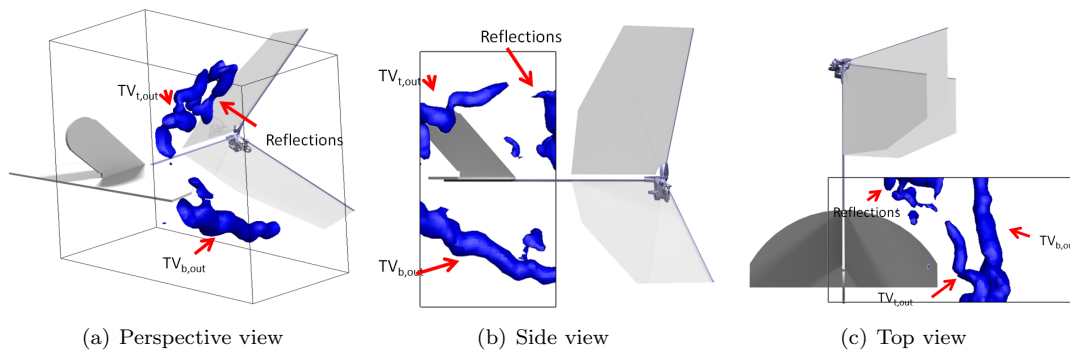
Figure 7.13 – *Vorticity magnitude plots at $\tau = 0.17$, isovalue: $|\omega| = 0.125 s^{-1}$.*

(a) Perspective view   (b) Side view   (c) Top view
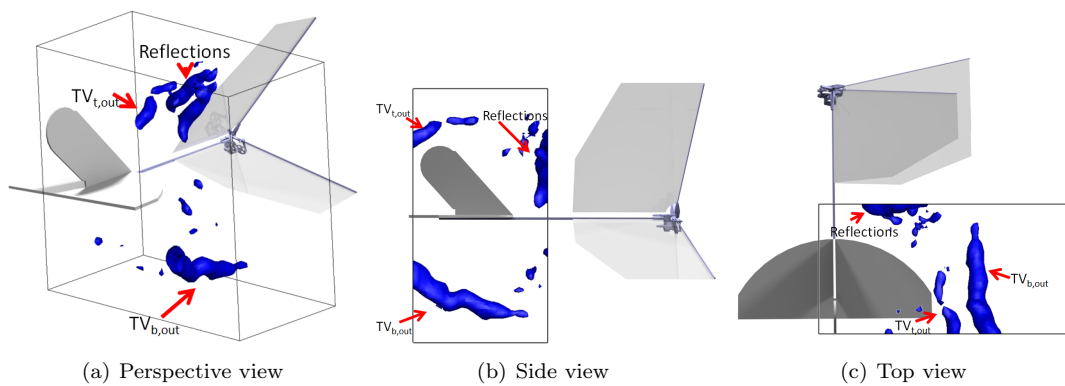
Figure 7.14 – *Vorticity magnitude plots at $\tau = 0.26$, isovalue: $|\omega| = 0.125 s^{-1}$.*

60

(a) Perspective view   (b) Side view   (c) Top view
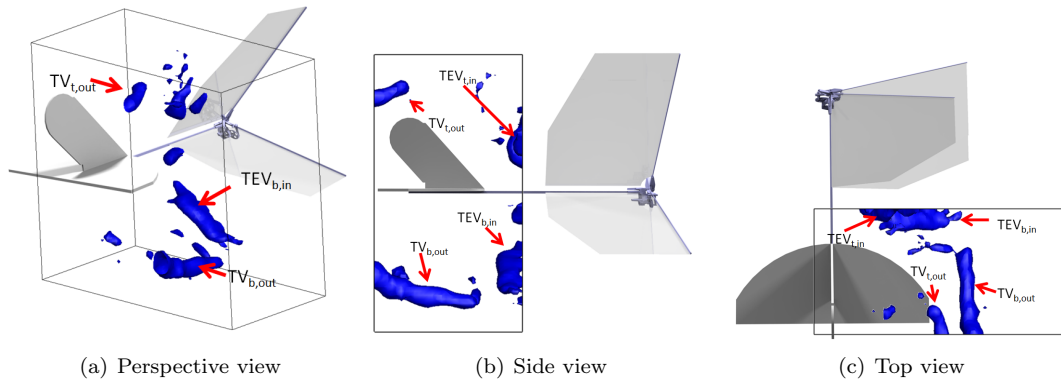
Figure 7.15 – *Vorticity magnitude plots at $\tau = 0.31$, isovalue: $|\omega| = 0.125s^{-1}$.*

(a) Perspective view   (b) Side view   (c) Top view
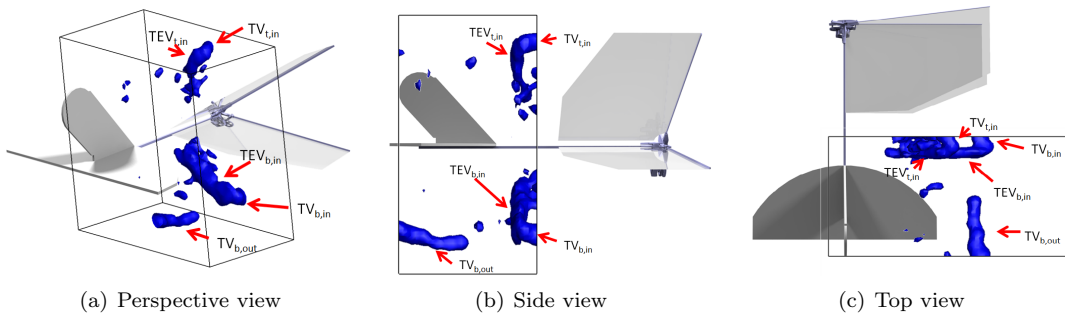
Figure 7.16 – *Vorticity magnitude plots at $\tau = 0.33$, isovalue: $|\omega| = 0.125s^{-1}$.*

(a) Perspective view   (b) Side view   (c) Top view
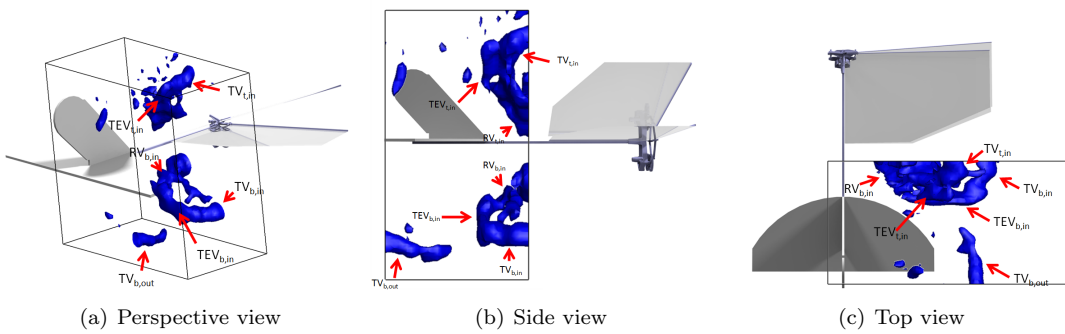
Figure 7.17 – *Vorticity magnitude plots at $\tau = 0.37$, isovalue: $|\omega| = 0.125s^{-1}$.*

(a) Perspective view   (b) Side view   (c) Top view
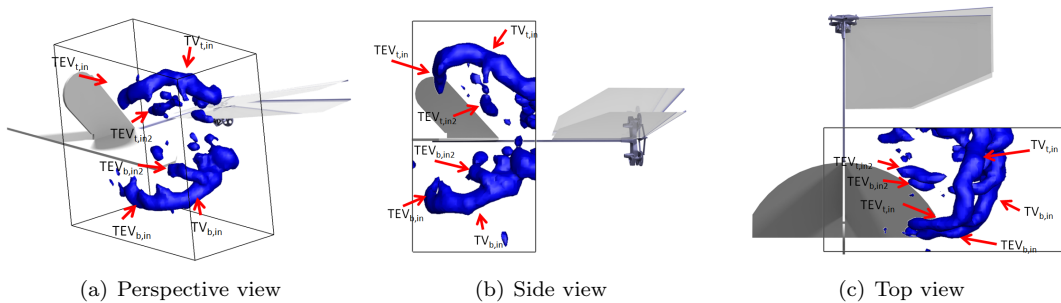
Figure 7.18 – *Vorticity magnitude plots at $\tau = 0.50$, isovalue: $|\omega| = 0.125s^{-1}$.*

(a) Perspective view   (b) Side view   (c) Top view
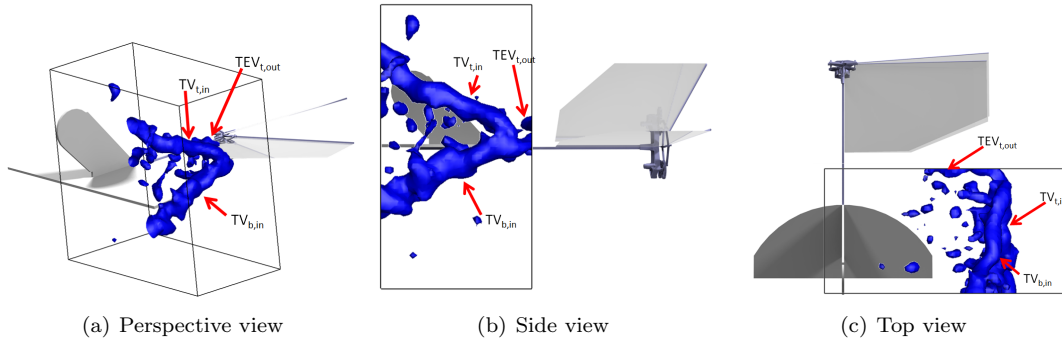
Figure 7.19 – *Vorticity magnitude plots at $\tau = 0.63$, isovalue: $|\omega| = 0.125s^{-1}$.*

(a) Perspective view   (b) Side view   (c) Top view
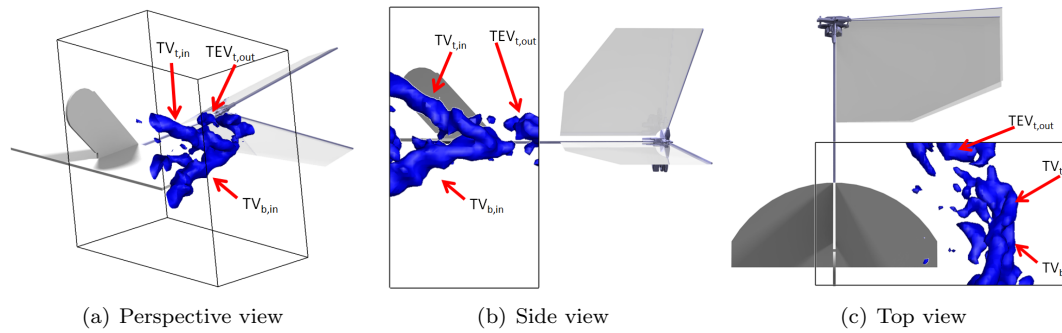
Figure 7.20 – *Vorticity magnitude plots at $\tau = 0.72$, isovalue: $|\omega| = 0.125s^{-1}$.*

(a) Perspective view   (b) Side view   (c) Top view
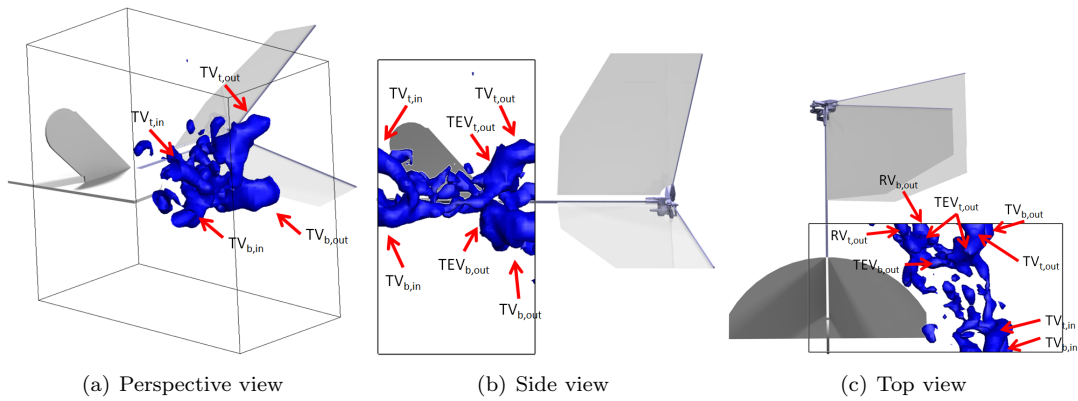
Figure 7.21 – *Vorticity magnitude plots at $\tau = 0.80$, isovalue: $|\omega| = 0.125s^{-1}$.*

(a) Perspective view   (b) Side view   (c) Top view
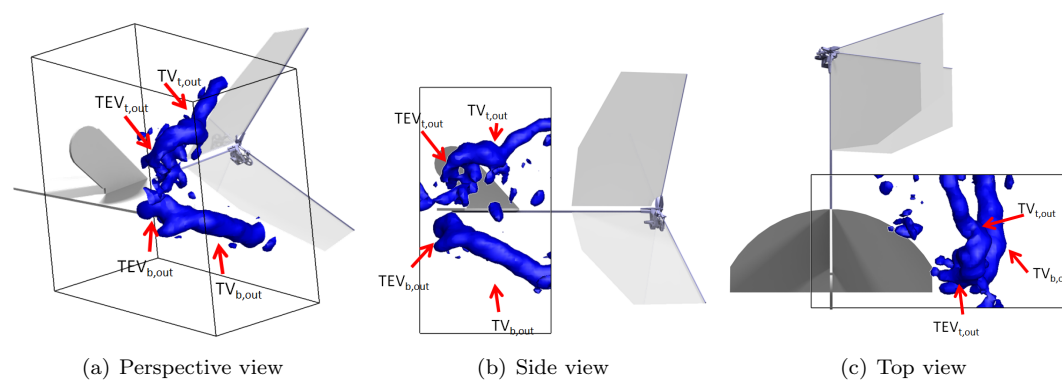
Figure 7.23 – *Vorticity magnitude plots at $\tau = 0.92$, isovalue: $|\omega| = 0.125s^{-1}$.*

| (a) Perspective view | (b) Side view | (c) Top view |
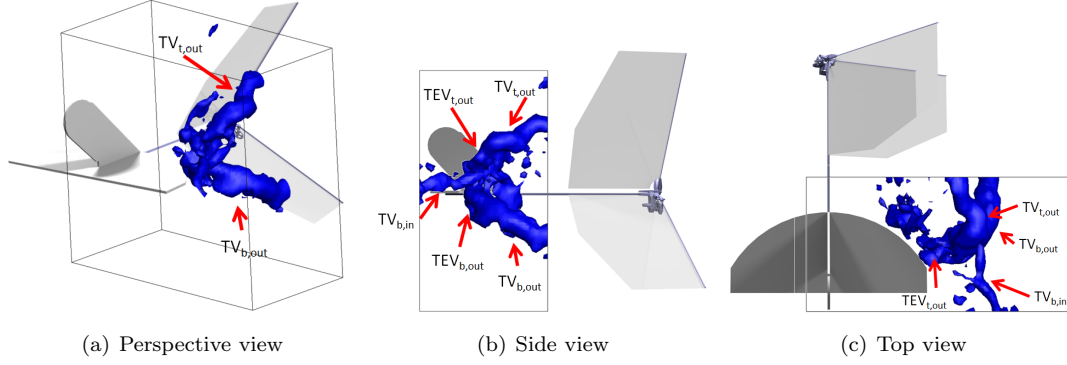
Figure 7.22 – *Vorticity magnitude plots at $\tau = 0.86$, isovalue: $|\omega| = 0.125s^{-1}$.*

7.3.2   Influence of flapping frequency

Increasing the flapping frequency of the DelFly changes the wake topology. To see the effect of the flapping frequency on the wake topology, the reduced frequency is increased to 0.50. The results are compared with reduced frequency case of 0.34. The forward flight velocity is set to 3 m/s and the angle of attack is set to 0 degree. The resulting wake topology is compared for two instances in the flap cycle: halfway the instroke (figures 7.24,7.25) and the end of the outstroke (figures 7.26-7.27).

In general it can be said that for an increasing reduced frequency, the vortical strength increases. Moreover, the vortical structure in general are closer to the tail for the higher reduced frequency. While the vortical structure are convected downstream relatively parallel to the freestream for the lower reduced frequency (see figure 7.25), an increasing reduced frequency introduces a path of the vortical structure that is more attracted to the tail. The possibility of vortices interacting with the tail increases. First of all observe that at time instance $\tau = 0.33$, the two starting vortices for the instroke $(TEV_{t,in}, TEV_{b,in})$ of highest reduced frequency (k=0.5, see figure 7.24(c)) are already completely shed into the wake and convected downstream. A closed U-shaped vortical structure appears, which is build up from RVs, TEVs and TVs (see figure 7.24(b)). In contrast to that only two TEVs and TVs are generated in the k=0.34 case (see figure 7.25(b)). Additionally, the results show that the finite gap between the vortical structure from outstroke and instroke is smaller in the k=0.50 case. The reason for this behavior is because the convection speed of both cases is equal while reduced frequency increases. In physical time it would mean that there is more shedding of vorticity per second. It is interesting to see in the k=0.50 case that the TV_t, out is already shed while the $TV_{b,out}$ is still connected to the $TEV_{b,in}$. Although the shedding bevahior of the TVs is found similar in the k=0.34 case, no connection between the $TV_{b,out}$ and the $TEV_{b,in}$ is observed.

Another interesting case is found at the end of outstroke ($\tau = 0.92$). Because the vorticity magnitude does not provide a very clear picture of the flow field, the vorticity magnitude consisting of the x- and y-component of the vorticity and separately the z-vorticity are plotted in one figure. The adjusted vorticity magnitude is given as:

$$|\omega_{xy}| = \sqrt{\omega_x^2 + \omega_y^2} \qquad (7.2)$$

The results of the two different cases are plotted in figure 7.23. Smaller iso-surface values are utilized for k=0.50 with respect to k=0.34 case in order to clearly visualize three-dimensional vortical structures. First of all note that in case k=0.34, both $TV_{t,out}, TV_{b,out}$ are both fully developed and convected downstream (see figure 7.27(b)). At the same instance however, the wake topology in the k=0.50 case is notably different. The two TVs generated during outstroke $(TV_{t,out}, TV_{b,out})$ are strongly connected via a vortex rotating mainly around the vertical axis. As noted before an increase in reduced frequency increases significantly the strength of the shed vortices. It is speculated that this is the main reason why these TVs during outstroke are observed to be connected. A close inspection of figure 7.27(c) reveals the same tendency. Both $TEV_{t,out}, TEV_{b,out}$ tend to move to each other. However, probably

due to the fact that the vortices are weaker in strength, they are convected downstream out of the volume before any interaction can be observed. Following the U-shaped votrtical structure observed in the k=0.50 case, it is seen that the U-shaped structure is still present at the end of outstroke ($\tau = 0.99$, see figure 7.28). When convected downstream, it moves towards the DelFly root. A short time interval after stroke reversal ($\tau = 0.17$), both $TV_{t,out}, TV_{b,out}$ are completely developed and convected downstream (see figure 7.29). However, the U-shaped structure is disconnected resulting in a similar structure as observed in the k=0.34 case at $\tau = 0.92$ (see figure 7.27). When scaling and positioning the DelFly with respect to the flow field the U-shaped vortical structure come very close towards the horizontal part of the tail (figure 7.29). It is suggested that there might be an interaction between the tail and the vortices that are shed from the flapping wings.

(a) Perspective view   (b) Side view   (c) Top view
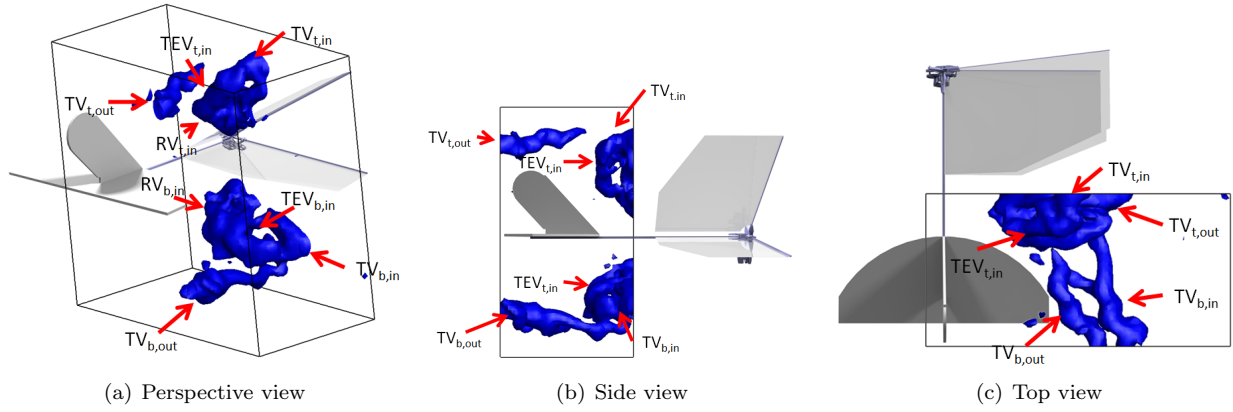
Figure 7.24 – *Vorticity magnitude plots at non-dimensional time $\tau = 0.31$. The reduced frequency for this case is 0.50. Isovalue contours: $|\omega| = 0.15s^{-1}$.*

(a) Perspective view   (b) Side view   (c) Top view
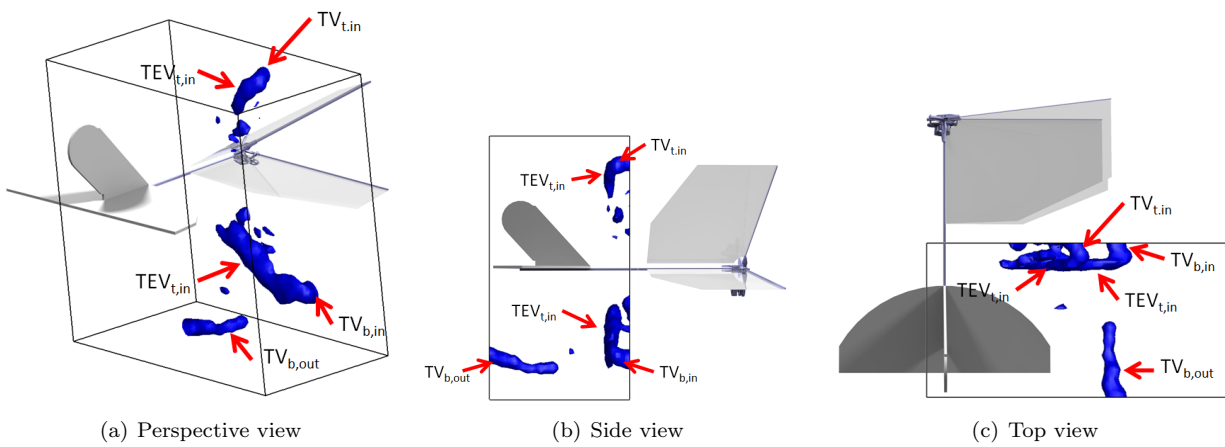
Figure 7.25 – *Vorticity magnitude plots at non-dimensional time $\tau = 0.31$. The reduced frequency for this case is 0.34. Isovalue contours: $|\omega| = 0.15s^{-1}$.*

(a) Perspective view   (b) Side view   (c) Front view
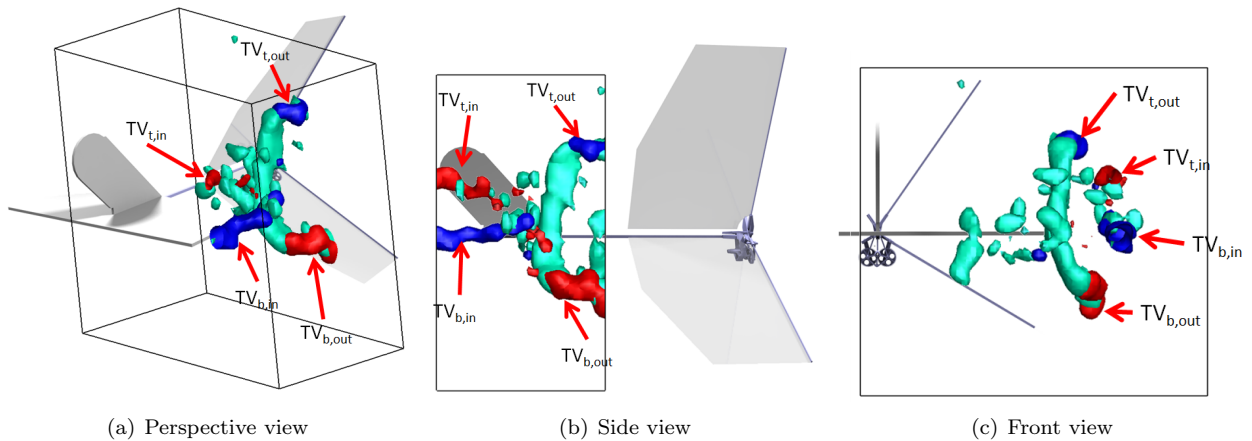
Figure 7.26 – *Vorticity magnitude ($|\omega_{xy}|$) combined with z-vorticity plots at $\tau = 0.92$ for a reduced frequency of 0.50. The isovalue for the vorticity magnitude surface is taken as: $|\omega_{xy}| = 0.2s^{-1}$. For the z-vorticity the iso values are chosen as: $\omega_z = \pm 0.20$. The blue color indicates clockwise z-vorticity whereas red surfaces indicate counterclockwise z-vorticity. The green colored surfaces are the vorticity magnitude ω_{xy} isosurfaces.*

65

(a) Perspective view   (b) Side view   (c) Front view
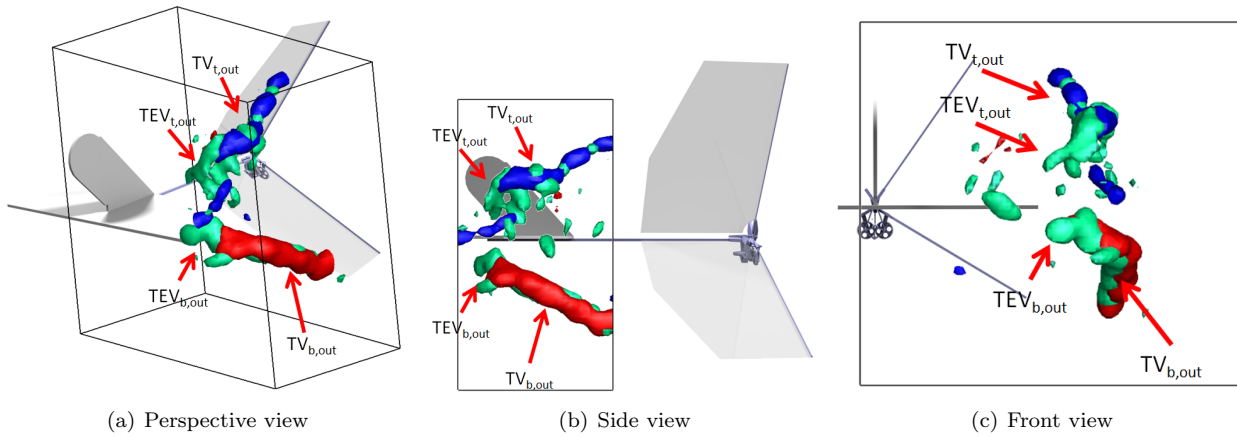
Figure 7.27 – *Vorticity magnitude ($|\omega_{xy}|$) combined with z-vorticity plots at $\tau = 0.92$ for a reduced frequency of 0.34. The isovalue for the vorticity magnitude surface is taken as: $|\omega_{xy}| = 0.15s^{-1}$. For the z-vorticity the iso values are chosen as: $\omega_z = \pm 0.125$. The blue color indicates clockwise z-vorticity whereas red surfaces indicate counterclockwise z-vorticity. The green colored surfaces are the vorticity magnitude ω_{xy} isosurfaces.*

(a) Perspective view   (b) Side view   (c) Front view
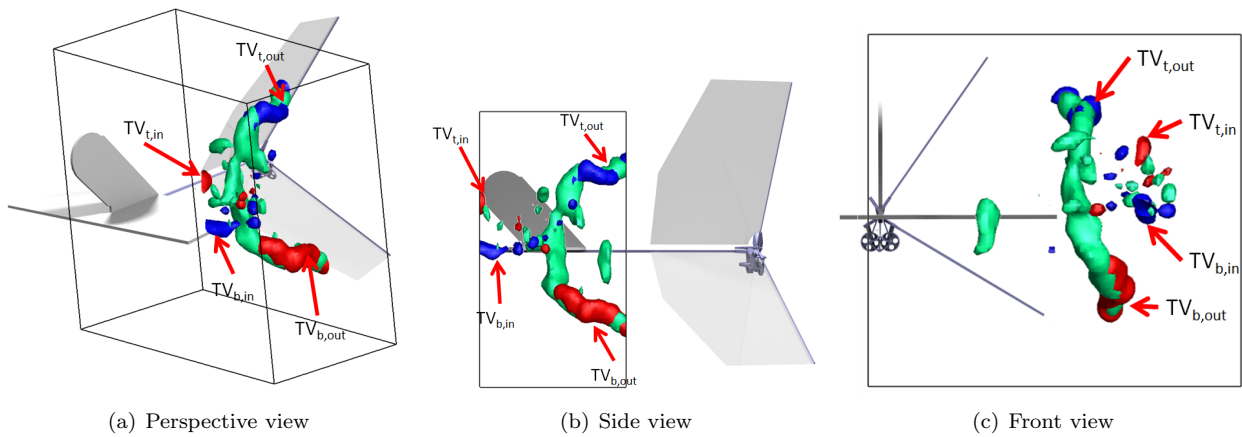
Figure 7.28 – *Vorticity magnitude ($|\omega_{xy}|$) combined with z-vorticity plots at $\tau = 0.99$ for a reduced frequency of 0.50. The isovalue for the vorticity magnitude surface is taken as: $|\omega_{xy}| = 0.2s^{-1}$. For the z-vorticity the iso values are chosen as: $\omega_z = \pm 0.20$. The blue color indicates clockwise z-vorticity whereas red surfaces indicate counterclockwise z-vorticity. The green colored surfaces are the vorticity magnitude ω_{xy} isosurfaces.*

(a) Perspective view   (b) Side view   (c) Front view
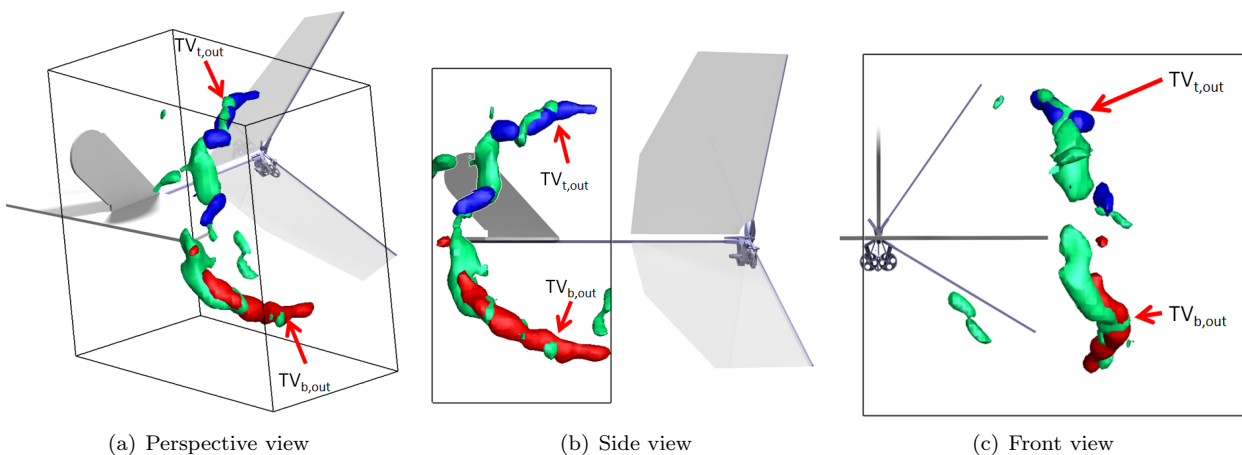
Figure 7.29 – *Vorticity magnitude ($|\omega_{xy}|$) combined with z-vorticity plots at $\tau = 0.17$ for a reduced frequency of 0.50. The isovalue for the vorticity magnitude surface is taken as: $|\omega_{xy}| = 0.2s^{-1}$. For the z-vorticity the iso values are chosen as: $\omega_z = \pm 0.20$. The blue color indicates clockwise z-vorticity whereas red surfaces indicate counterclockwise z-vorticity. The green colored surfaces are the vorticity magnitude ω_{xy} isosurfaces.*

7.3.3　Influence of free stream velocity

The reduced frequency values for 3 and 6 m/s free stream velocities are 0.42 and 0.21, respectively. For clarity, two phases of the flapping motion (the start of clap and the end of fling) are compared in terms of coherent vortical structures. The reconstructed flow volumes are shown in figures 7.30-7.33. Comparison of vorticity magnitude at the start of clap (figures 7.30,7.31) shows that flow structures for the case of lower free stream velocity have greater coherency than that in the case of higher free stream case. It is not surprising as the free stream velocity increases, the vorticity generated in the vicinity of the wing is being convected faster downstream. It is also clear that the generation of flow structures also occurs with a phase difference between two cases. Tip vortices are already shed downstream for the case of k=0.21 (Figure 7.31(b)) whereas for the case of k=0.42, they are still connected throughout the measurement volume (Figure 7.30(b)). Moreover, another consequence of halving the reduced frequency manifests itself in the generation of trailing edge vortices. It is observed that the TEVs present for the k=0.42 are not being formed in the lower reduced frequency case. It is possible to indicate that the shed vorticity from the trailing edge cannot roll up into discrete vortices as the free stream flow dominates. Moreover, it can be speculated that the effective angle of attack of the wings (vertical velocity of the wing over free stream velocity) decreases with increasing free-stream velocity and weaker vortical structures are generated.

(a) Perspective view　　　　　(b) Side view　　　　　(c) Front view
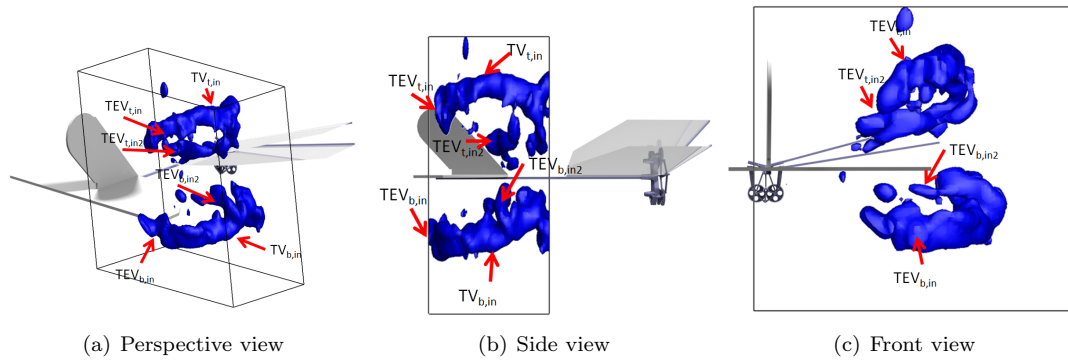
Figure 7.30 – *DelFly flying at a forward velocity of 3 m/s. Vorticity magnitude plots at $\tau = 0.50$, isovalue: $|\omega| = 0.15s^{-1}$.*

(a) Perspective view　　　　　(b) Side view　　　　　(c) Front view
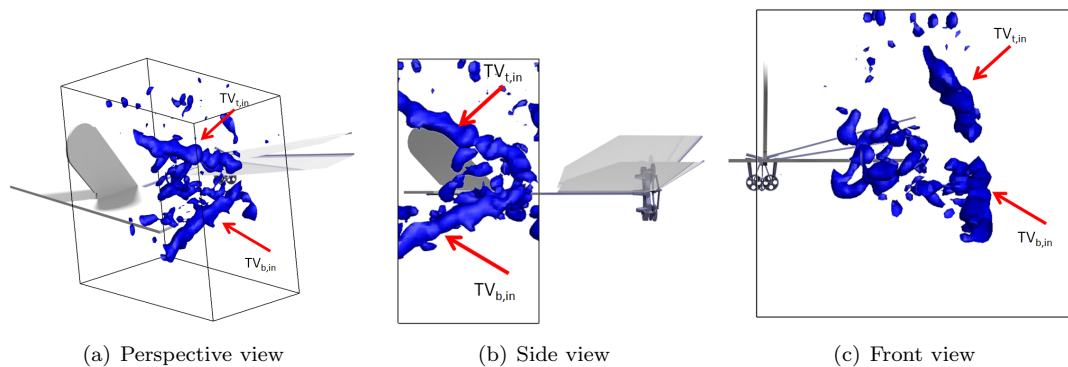
Figure 7.31 – *DelFly flying at a forward velocity of 6 m/s. Vorticity magnitude plots at $\tau = 0.50$, isovalue: $|\omega| = 0.15s^{-1}$.*

67

(a) Perspective view   (b) Side view   (c) Front view
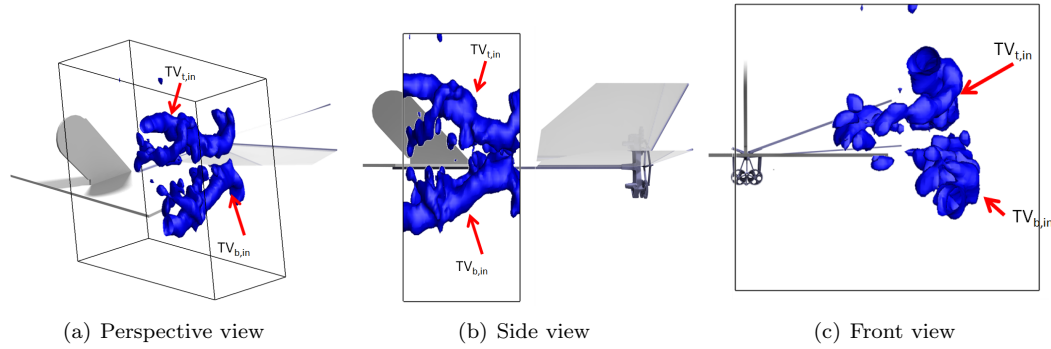
Figure 7.32 – *DelFly flying at a forward velocity of 3 m/s. Vorticity magnitude plots at $\tau = 0.63$, isovalue: $|\omega| = 0.15s^{-1}$.*

(a) Perspective view   (b) Side view   (c) Front view
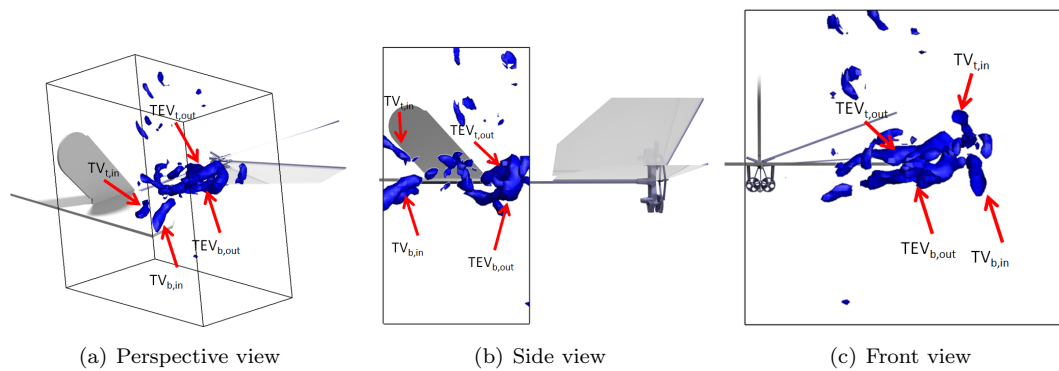
Figure 7.33 – *DelFly flying at a forward velocity of 6 m/s. Vorticity magnitude plots at $\tau = 0.63$, isovalue: $|\omega| = 0.15s^{-1}$.*

7.3.4 Influence of angle of attack

During forward flight, the DelFly flies under a range of angles of attack. During slow forward flight, the DelFly flies almost vertically whereas during fast forward flight, the DelFly flies almost horizontally. While the pitch angle of the balance support can only be varied upto 30 degree, realastic flight conditions cannot be obtained during the measurements, especially at the lower forward velocities. However, to see the influence of the angle of attack on the wake topology, two different angles of attack are researched: 0 and 10 degrees. The tail is positioned at 3 cm downstream the TE, the forward velocity is set to 3 m/s and the reduced frequency is set to 0.42. The reconstructed measurement volume is shown at two instances in the flap cycle: $\tau = 0.50$ and $\tau = 0.92$. The 5 degree angle of attack case is also researched. However, the results suggest no significant difference compared to the 0 degree case. Therefore, this case is omitted in the present discussion.

The first difference observed is the increased strength of the upper TV ($TV_{t,out}$) with respect to the $TV_{b,out}$ (see figure 7.35). In contrast to the 0 degree case, at the high angle of attack the strength of the upper TV ($TV_{t,out}$) is higher during instroke. In the 10 degree case, the TVs and TEVs are closer towards the tail of the DelFly. Furthermore, observe the presence of a vortical pair shed at the top wing in the 10 degree case (see figure 7.35). This feature is not observed in the 0 degree case (see figure 7.34). Checking the sign of this vortex pair, it turns out that this is most probably build up by a TEV as well as a LEV. Due to the lower geometrical angle of attack of the lower wing, this vortex pair is not present at the bottom wing.

Moving to the end of outstroke (see figures 7.36,7.37) it is observed that the qualitative behavior of the wake topology does not change while changing the angle of attack of the DelFly. The connection

between the TVs as observed in figure 7.28 is also present in the current cases. In contrast to the instroke phase no clear LEV shedding is observed during outstroke. Observe furthermore, that the $TV_{b,out}$ is much higher in strength compared to the $TV_{t,out}$ in case the angle is 10 degrees. Looking at the wake topology in figure 7.37 it is most probable that while the LEV on the bottom wing is still attached to the wing surface(and thus feeding the $TV_{b,out}$), the LEV on the top wing is unstable and shed. In both cases presented below, no clear and distinct TEV is formed on both wings. This is an expected consequence of the clap-and-peel mechanism.

(a) Perspective view   (b) Side view   (c) Front view
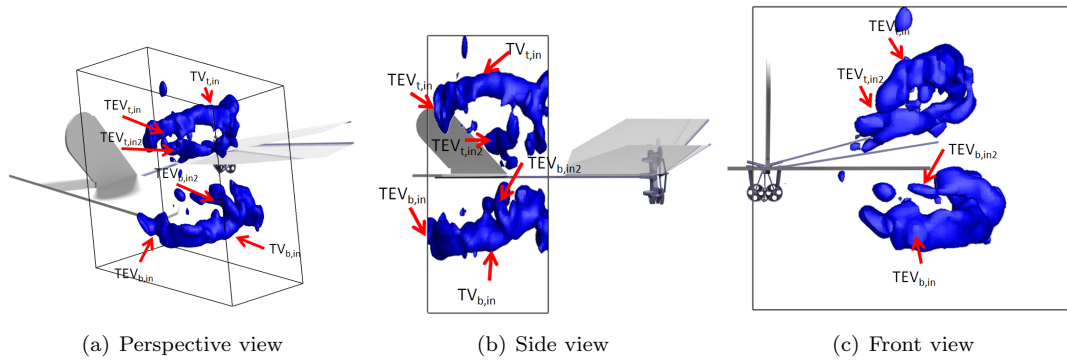
Figure 7.34 – *DelFly at an angle of attack of 0 degree. Vorticity magnitude plots at $\tau = 0.50$, isovalue: $|\omega| = 0.15s^{-1}$.*

(a) Perspective view   (b) Side view   (c) Front view
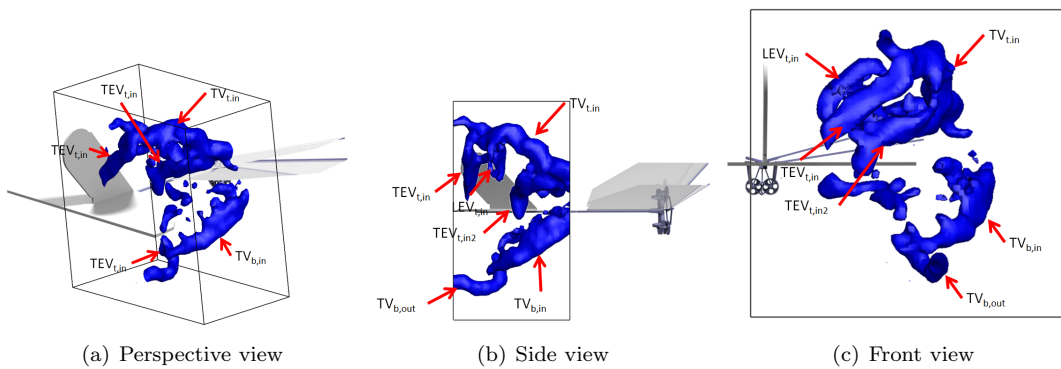
Figure 7.35 – *DelFly at an angle of attack of 10 degree. Vorticity magnitude plots at $\tau = 0.50$, isovalue: $|\omega| = 0.15s^{-1}$.*

(a) Perspective view   (b) Side view   (c) Front view
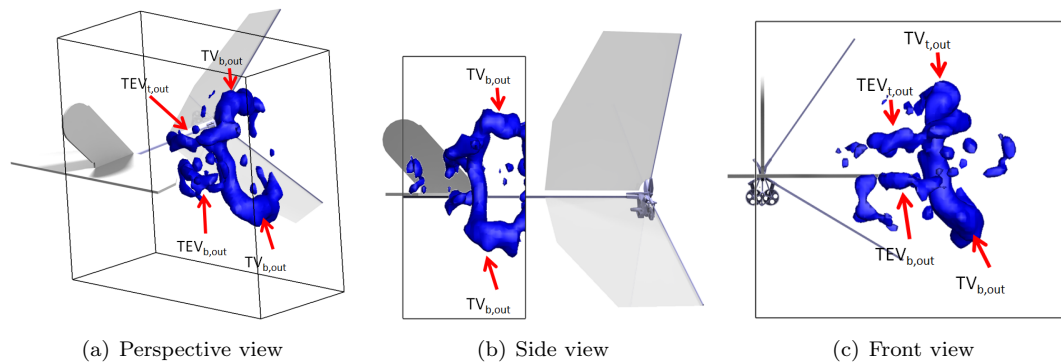
Figure 7.36 – *DelFly at an angle of attack of 0 degree. Vorticity magnitude plots at $\tau = 0.92$, isovalue: $|\omega| = 0.15s^{-1}$.*

(a) Perspective view   (b) Side view   (c) Front view
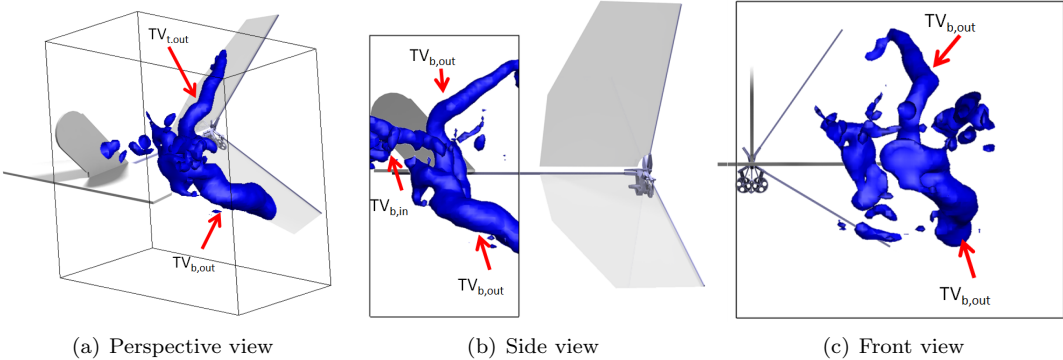
Figure 7.37 – *DelFly at an angle of attack of 10 degree. Vorticity magnitude plots at $\tau = 0.92$, isovalue: $|\omega| = 0.15s^{-1}$.*

Conclusions and recommendations

This chapter summarizes the most important conclusions of the current research. Furthermore, recommendations are presented for future research. The goal of this research, as stated in the introduction is given as:

Perform force measurements and flow visualizations in the wake of the flapping wing MAV 'DelFly II' in forward flight configuration

This project goal is split into two experimental parts: force measurements and PIV measurements. As both parts are succesfully completed, it can be stated that the project goal is achieved. The main conclusions that are drawn from both force and PIV measurements are given in section 8.1. Furthermore, recommendations regarding future research are given in section 8.2.

8.1   Conclusions

From the phase determination of the DelFly wings it is shown that the phase distribution is almost equal for different flapping frequencies. No phase difference or maximum stroke difference exists between the different flapping frequencies. Furthermore, kriging interpolation is succesfully applied on the reconstruction of the three dimensional measurement flow. Force measurements are subject to severe mechanical resonance. As a consequence, a low pass filter is applied to remove these resonance frequencies. Because of the absence of the accurate offset values for the force measurements performed simulatanously with the PIV experiments, additional force measuremnts are performed. These measurements are however uncorrelated with the PIV results. The force results obtained during these measurements show the positive contribution of the horizontal tail on both lift and thrust production. This increased thrust is most probably due to the induced flow field by the flapping wings on the horizontal tail. An increasing flapping frequency shows a higher thrust force. The lift force remains relatively constant over the different flapping frequencies at zero degrees angle of attack. Increasing the angle of attack of the DelFly, yields a significantly higher lift. The main reason for this is because the DelFly wings are under a positive angle of attack, thereby generating an additional upward lift force. Additionally, the streamwise generated force contributes to the generated lift. On the other hand, thrust force decreases considerably when the free stream velocity increases. At the same time, the average generated lift force remains approximately zero. This is mainly attributed to a reduced effective angle of attack on the wings.

The wake topology shows the presence of two very clear TVs on both wings of opposite sign. Both

time series and spatial reconstrucions show similar behavior in the evolution of the TVs during a flapping cycle. Furthermore, the spatial reconstruction show that the TVs on both wings are strongly connected to a possible starting trailing edge vortex which is shed during stroke reversal. Due to the spatial distance between trailing edges of the wings and the reconstructed measurement volume the characteristic flow structures from the new stroke are by delayed 30% of the non-dimensional time.

A U-shaped vortical structure appears during the instroke on both wings, consisting of TVs, TEVs and RVs. The RVs appear to be relatively weak in strength and dissappear at the end of instroke. At the end of instroke, the wake reconstructions show the shedding of an additional TEV. As a result of the clap-and-fling mechanism only a small TEV is generated at the outer parts on both wings during this phase. Still two very clear TVs are generated during outstroke. At the start of the tapered parts, a small RV develops on both. These RVs form together with TEVs and the TVs a U-shaped structure on the outer part of the wings. Furthermore, the TV generated during outstroke on the top wing is a less coherent structure and shed earlier into the wake compared to the TV generated on the bottom wing. No shed leading edge vorticity is observed in the reconstructed volume at all time instances in the wake topology. It is suggested that the LEV is shed and convected downstream outside the measurement volume.

Increasing the reduced frequency yields a different wake topology. The amount of vortex shedding increases significantly. The vortices have a higher strenght when the reduced frequency increases. Furthermore, the finite gap between the flow structures from outstroke and instroke reduces. During the instroke phase, the qualitative behavior of the different cases is equal. During the outstroke phase of the highest reduced frequency case, a very clear connection exists between the TVs on both wings. The reaons for this connection is most probably due to the relative high strength of the TVs generated during outstroke. After stroke reversal, the connection between both TVs is broken, suggesting a possible interaction with the horizontal part of the tail.

An increasing free stream velocity, thereby lowering the reduced frequency,decreases the coherency of the vortical structures. Furthermore, the increased free stream velocity causes the vortical structures to be shed faster and earlier into the wake. Moreover, the shed vorticity cannot roll up into discrete vortices in case of a higher free stream velocity.

Increasing the angle of attack of the DelFly leads to stronger and more distinct vortical structures on the top wing during the instroke. This is due to the higher geometrical angle of attack of the top wing. The most important observation to made for these cases is the shedding of leading edge vorticity during the instroke. Each shed TEV is followed by a LEV. During the outstroke, no shedding of leading edge vorticity is observed.

8.2 Recommendations

The current research has openend a new area in the resarch of the aerodynamic performance of the DelFly. As a pioneer in this field of research, it is realized that there are ways to improve the results even more. Because of the limited time, the wake topology and the force results are only examined for a few cases. Furture research is recommended to focus on different measurement configuration of the DelFly. Second of all, correct force measurements are still difficult to perform. The relative low resonance frequencies of the complete system make it impossible to obtain accurate force measurements. Future research might give attention to this topic. The force results indicate that the thrust production is enhanced by the presence of the tail. Further research is necessary to research how the wake of the flapping wings interacts with the horizontal tial.

Operating at the edges of what is currently possible, the experimental setup turned out to be extremely sensitive to small changes. As such, the quality of the measurements varied from day to day. With the knowledge obtained during the experiments, it is advisable to redo (parts) of the experiments and obtain cleaner results. Furthermore, reflections from tail and fuselage prohibited the flow field visualizations close to the fuselage root. No clear interaction is observed between the wake and the horizontal tail. Due to the limited amount of experimental data, only a number of different cases could be researched. Still a lot of parameters are not completely researched. Future research might

focuss on a study in which all different experimental parameters are varied in a more complete way.

The employed kriging interpolation routine has proven to be reliable, flexible and robust in use. However, vector outliers at the edges of the flow field have a significant influence on the flow field. Donut shaped structures appear in the flow field in case the outliers are not completely removed. To limit the influence of these outliers future research might include the Signal to Noise Ratio (SNR). According to the research of Westerweel [?], this ratio gives a measure for the reliability that the found displacement corresponds to a valid displacement. In general, the SNR is low for vector outliers, whereas a higher value is obtained for normal vectors. This might diminish the effect of the vector outliers.

Bibliography

[1] De Clercq, K.M.E., "Flow visualization and force measurements on a hovering flapping-wing MAV DelFly", *Delft University of Technology M.Sc. thesis*, (2009)

[2] Bruggeman, B. "Improving flight performance of DelFly II in hover by improving wind design and driving mechanism", *Delft University of Technology M.Sc. thesis*, (2010)

[3] Groen, M.A. "PIV and force measurements on the flapping-wing MAV DelFly II", *Delft University of Technology M.Sc. thesis*, (2010)

[4] Dickinson, M.H.; Gtz, K.G. "Unsteady Aerodynamic Performance of Model Wings at Low Reynolds Numbers", *J. exp. Biol.*, vol. 174, pp. 45-64, (1993)

[5] Singh, B.; Ramasamy, M.; Chopra, I.; Leishman, J.G. "Experimental Studies on Insect-Based Flapping Wings for Micro Hovering Air Vehicles", *46th AIAA/ASME/ASCE/AHS/AHS Structures, Structural Dynamics & Materials Conference*, Austin, Texas, AIAA 2005-2293, (2005)

[6] Yates, G.T. "Optimum Pitching Axes in Flapping Wing Propulsion", *J. theor. Biol.*, vol. 120, pp 255-276, (1986)

[7] Shyy, W.; Liu, H. "Flapping Wings and Aerodynamic Lift: The Role of Leading-Edge Vortices", *AIAA Journal*, vol. 45, pp. 2817-2819, (2007)

[8] Ansari, S.A.; Knowles, K.; Zbikowski, R. "Insect Flapping Wings in the Hover Part 1: Effect of Wing Kinematics", *Journal of Aircraft*, vol. 45, pp. 1945-1954, (2008)

[9] Sane, S.P. "The aerodynamics of insect flight", *The Journal of Experimental Biology*, vol. 206, pp. 4191-4208, (2003)

[10] Wootton, R.J. "Support and deformability in insect wings", *Journal of Zoology: Proceedings of the Zoological Society of London*, vol. 193, pp. 447-468, (1981)

[11] Combes, S.A.; Daniel, T.L. "Flexural stiffness in insect wings I.Scaling and influence of wing venation", *The Journal of Experimental Biology*, vol. 206, pp. 2979-2987, (2003)

[12] Gopalakrishnan, P.; Tafti, D.K. "Effect of Wing Flexibility on Lift and Thrust Production in Flapping Flight, *AIAA Journal*, vol. 48, pp. 865-877, (2010)

[13] Heathcote, S.; Gursul, I. "Flexible Flapping Airfoil Propulsion at Low Reynolds Numbers", *AIAA Journal*, vol. 45, pp. 1066-1079, (2007)

[14] Elligton, C.P. "The Novel Aerodynamics of Insect Flight: Applications to Micro-Air Vehicles", *The Journal of Experimental Biology*, vol. 202, pp. 3439-3448, (1999)

[15] Lehmann, F.O. "The mechanisms of lift enhancement in insect flight",*Naturwissenschaften*, vol. 91, pp. 101-122, (2004)

[16] Miller, L.A.; Peskin, C.S. "Flexible clap and fling in tiny insect flight",*The Journal of Experimental Biology*, vol. 212, pp. 3076-3090, (2009)

[17] Hedenstrm, A.; Johansson, L.C.; Wolf, M.; von Busse, R.; Winter, Y.; Spedding, G.R. "Supporting online material for: Bat Flight Generates Complex Aerodynamic Tracks", *Science*, www.sciencemag.org/cgi/content/full/316/5826/894/DC1, (2007)

[18] Cebeci, C.; Platzer, M.; Chen, H.; Chang, K.C.; Shao, J.P. "Analysis of Low-Speed Unsteady Airfoil Flows", *Springer*, New York, (2005)

[19] Henningson, P.; Muijres, F.T.; Hedenstrm, A. "Time-resolved vortex wake of a common swift flying over a range of flight speeds", *J. R. Soc. Interface*, DOI:10.1098, (03-12-2010)

[20] Von Kármán, T.; Burgers, J.M. "General Aerodynamic Theory - Perfect Fluids", *Aerodynamic Theory*, vol. 2, pp 308, (1934)

[21] Hu, H.; Clemons, L.; Igarashi, H. "An experimental study of the unsteady vortex structures in the wake of a root-fixed flapping wing, *Exp. Fluids*, (2011)

[22] Platzer, M.F.; Jones, K.D.; Young, J.; Lai, J.C.S. "Flapping-Wing Aerodynamics: Progress and Challenges", *AIAA Journal*, vol. 46, pp. 2136-2149, (2008)

[23] Anderson, J.M.; Streitlien, K.; Barrett, D.S.; Triantafllou, M.S. "Oscillating foils of high propulsive efficiency, *J. Fluid Mech.*, vol. 360, pp. 41-72, (1998)

[24] Jones, K.D.; Dohring, C.M.; Platzer, M.F. Wake structures behind plunging airfoils - A comparison of numerical and experimental results, *34th AIAA Aerospace Sciences Meeting and Exhibit*, AIAA-96-0078, (1996)

[25] Guerrero, J. "Numerical Simulation of the Unsteady Aerodynamics in Flapping Flight, *University of Genoa, doctoral dissertation*, (2009)

[26] Hubel, T.Y.; Hristov, N.I.; Swartz, S.M.; Breuer, K.S. "Time-resolved wake structure and kinematics of bat flight", *Exp. Fluids*, vol. 46, pp. 933-943, (2009)

[27] Muijres, F.T.; Johansson, L.C.; Winter, Y.; Hedenstrm, A. "Comparative aerodynamic performance of flapping flight in two bat species using time-resolved wake visualization", *J.R. Soc. Interface*, DOI: 10.1098, (02-03-2011)

[28] Muijres, F.T.; Spedding, G.R.; Winter, Y.; Hedenstrm, A. "Actuator disk model and span efficiency of flapping flight in bats based on time-resolved PIV measurements", *Exp. Fluids*, DOI: 10.1007, (23-03-2011)

[29] Stuiver, M. "Bats in Gliding Flight, A comparative wind tunnel investigation of the aerodynamics of gliding bats and a bat inspired gliding wing model", *Delft University of Technology/ Lund University M.Sc. thesis*, (2011)

[30] Hedenström, A.; Johansson, L.C.; Wolf, M.; von Busse, R.; Winter, Y.; Spedding, G.R. "Bat Flight Generates Complex Aerodynamic Tracks", *Science*, vol. 316, pp. 894-897, (2007)

[31] Rayner, J.M.V.; Jones, G.; Thomas, A. "Vortex flow visualizations reveal change in upstroke function with flight speed in bats", *Nature*, vol. 321, pp. 162-164, (1986)

[32] Hedenstrm, A.; Muijres, F.T.;von Busse, R.; Johansson, L. C.; Winter, Y.; Spedding, G.R. "High-speed stereo DPIV measurement of wakes of two bat species flying freely in a wind tunnel", *Exp. Fluids*, vol. 46, pp. 923-932, (2009)

[33] Johansson, L.C.; Wolf, M.; von Busse, R.; Winter, Y.; Spedding, G.R.; Hedenstrm, A. "The near and far wake of Pallas' long tongued bat (Glossophaga soricina)", *The Journal of Experimental Biology*, vol. 211, pp. 2909-2918, (2008)

[34] Schmidt, W. "Die Wellpropeller, ein neuer Antrieb fuer Wasser-, Land-, und Luftfahrzeuge", *Zeitschrift fur Flugwiss*, vol. 13, pp. 472-479, (1965)

[35] Tuncer, I.H.; Platzer, M.F. "Thrust Generation due to Airfoil Flapping", *AIAA Journal*, vol. 34, pp. 324-331, (1996)

[36] Aziz, H.; Mukherjee, R. "Unsteady Aerodynamics of Multiple Airfoils in Configuration", *29th AIAA Applied Aerodynamics Conference*, AIAA 2-11-3523, (2011)

[37] Ellington, C.P.; Van den Berg, C.; Willmott, A.P.; Thomas, A.L.R. "Leading-edge vortices in insect flight", *Nature*, vol. 384, pp. 626-630, (1996)

[38] de Croon, G.C.H.E.; de Clercq, K.M.E.; Ruijsink, R.; Remes, B.; Wagter, C. "Design, aerodynamics, and vision-based control of the DelFly", *IMAV*, (2006)

[39] Shyy, W.; Aono, H.; Chimakurthi, S.K.; Trizila, P.; Kang, C.-K.; Cesnik, C.E.S.; Liu, H. "Recent progress in flapping wing aerodynamics and aeroelasticity", *Progress in Aerospace Sciences*, vol. 46, pp. 284-327, (2010)

[40] Raffel, M.; Willert, C.E.; Wereley, S.T.; Kompenhans, J. "Particle Image Velocimetry, A Practical Guide", 2nd edition, *Springer-Verlag Berlin*, Heidelberg, (2007)

[41] Scarano, F. "Experimental Aerodynamics",*Delft University of Technology Course notes*, Chapter 9 PIV, pp 107-133, (2007)

[42] Westerweel, J. "Efficient detection of spurious vectors in particle image velocimetry data",*Experiments in Fluids*,vol. 16, pp. 236-247,(1994)

[43] Westerweel, J.; Scarano, F. "Universal outlier detection for PIV data",*Experiments in Fluids*,vol. 6, pp. 1096-1100,(2005)

[44] Wikle, C.K.; Berliner, L.M. "A Bayesian tutorial for data assimilation",*Physica D: Non linear Phenomena*,vol. 230, pp. 1-16, (2007)

[45] Morel, T. "Comprehensive Design of Axisymmetric Wind Tunnel Contractions",*Journal of Fluids Engineering, Transactions of the ASME*,pp. 225-233,vol. 97 ,(1975)

[46] Maikhail, M.N.; Rainbird, W.J. "Optimum desing of wind tunnel contractions",*Aerodynamic Testing Conference, 10th*,California, pp: 376-384,(1978)

[47] Anderson, J.D. "Fundamentals of Aerodynamics", 4th edition, *McGraw-Hill*, New York, (2005)

[48] Jones, D.R. "A Taxonomy of Global Optimization Methods Based on Response Surface",*Journal of Global Optimization*, vol. 21, pp. 345-383, (2001)

[49] Forrester, A.I.J.; Keane, A.J.; Bressloff, N.W. "Design and Analysis of "Noisy" Computer Experiments", *AIAA Journal*, vol. 44, pp. 2331-2339,(2006)

[50] Percin, M.; Hu, Y.; van Oudheusden, B.W.; Remes, B.; Scarano, F. "Wing flexibility effects in clap-and-fling", *Proceedings of the International Micro Air Vehicles conference*, (2011)

APPENDIX A

Specifications Nano 17

Specifications		
Manufacturer	ATI Industrial Automation	
Type	Nano 17	
Material	Stainless steel	
Weight	0.00907	[kg]
Diameter	17	[mm]
Height	15	[mm]
Ranges, SI-12-0.12		
$F_{x,y}$	12	[N]
F_z	17	[N]
$T_{x,y}$	120	[Nmm]
T_z	120	[Nmm]
Resolutions, SI-12-0.12		
$F_{x,y}$	1/320	[N]
F_z	1/320	[N]
$T_{x,y}$	1/64	[Nmm]
T_z	1/64	[Nmm]
Single-Axis Overload		
$F_{x,y}$	± 250	[N]
F_z	± 480	[N]
$T_{x,y}$	± 1.6	[Nm]
T_z	± 1.8	[Nm]
Stiffness (Calculated)		
X-axis & Y-axis forces (K_x, K_y)	$8.2 \cdot 10^6$	[N/m]
Z-axis force (K_z)	$1.1 \cdot 10^7$	[N/m]
X-axis & Y-axis torque (K_{tx}, K_{ty})	$2.4 \cdot 10^2$	[Nm/rad]
Z-axis torque (K_{tz}, K_{ty})	$3.8 \cdot 10^2$	[Nm/rad]
Resonant Frequency (Measured)		
F_x, F_y, T_z	7200	[Hz]
F_z, T_x, T_y	7200	[Hz]

Table A.1 – *Specifications Nano 17, six component force balance*

78

TOOL SIDE

ISOMETRIC VIEW

SIDE VIEW

MOUNTING SIDE

(2) Ø 2.0
Slip Fit ▽ 3.0
(B.C. Ø 12.5)

(3) M2-.40 ▽ 3.5
Equally Spaced
B.C. Ø 12.5
Customer Interface
(See Note 5)

Sensing Reference
Frame Origin

5.411±0.025

6.248±0.025

9.373±0.025

+X

-X

+Y

-Y

Tool Adapter

Sensing Reference
Frame Origin

Ø 17

+Z

-Z

14.5

Mounting
Adapter

1.085±0.025

(2) Ø 2.0
Slip Fit ▽ 3.0
(B.C. Ø 12.5)

(3) M2-.40 ▽ 3.5
Equally Spaced
B.C. Ø 12.5
Customer Interface
(See Note 5)

6.957±0.025

6.153±0.025

8.291±0.025

+X

-X

+Y

-Y

5°

48°

Ø 5.3

17.6

15.5

79

Notes:
1. Tool and mounting adapter made of aluminum.
2. Tool and mounting adapter have M2 tapped holes and
   2.0mm dowel pin holes for customer interface.
3. Connector (not shown) has a 17mm diameter and
   is 67.5mm long.
4. **WARNING--DO NOT LOOSEN OR REMOVE INTERFACE
   PLATES DUE TO POTENTIAL DAMAGE.**
5. **DO NOT EXCEED INTERFACE DEPTH--MAY CAUSE DAMAGE**

NOTES: UNLESS OTHERWISE SPECIFIED

DO NOT SCALE DRAWING. DRAWN IN SOLIDWORKS.
ALL DIMENSIONS ARE IN MILLIMETERS.

3rd ANGLE PROJECTION

1031 Goodworth Drive, Apex, NC 27539, USA
Tel: +1.919.772.0115   Email: info@ati-ia.com
Fax: +1.919.772.8259   www.ati-ia.com
ISO 9001 Registered Company

ATI INDUSTRIAL AUTOMATION

DRAWN BY: P. Fusco 3/8/07
CHECKED BY: D. Swanson 3/9/07
WEIGHT LBS:
ASSEMBLY REF:

TITLE
NANO17-E TRANSDUCER

SCALE
3:1

SIZE
B

DRAWING NUMBER
9230-05-1311-02

SHEET 1 OF 1

PRODUCT RELEASE #   DATE:

Rev.	Description	Initiator	Date
01	Initial Drawing	PPF	3/8/2007
02	Updated dimensions from strain relief to center of part	PPF	5/27/2008

APPENDIX B

Specifications DelFly

Parameter	Value	Unit
Specifications		
Mass	17	$[g]$
Flapping frequency	11-14	$[Hz]$
Wing span (b)	280	$[mm]$
Wing area (S)	22,390	$[mm^2]$
Mean chord length $(\bar{c})$	79.96	$[mm]$
Wing dihedral angle (ψ)	12	$[deg]$
Maximum stroke amplitude (ϕ)	44	$[deg]$
Similarity parameters		
Reynolds number (Re)[1]	5,500-22,000	$[-]$
Advance ratio (J)	0.85-3.4	$[-]$
Strouhal number (St)	0.59-0.15	$[-]$
Reduced frequency (k)	0.69-0.17	$[-]$

Table B.1 – *Specifications and similarity parameters of the DelFly*

Technical drawings nozzle W-tunnel

Left view
Scale: 1:15

1386
1166
110
110
110
1166
1386

Isometric view
Scale: 1:15

Front view
Scale: 1:15

1386
40

83

DASSAULT SYSTEMES

DRAWING NUMBER
FrameContraction1

SHEET 1/1

SIZE A3
WEIGHT (kg) 0,00
SCALE 1:15

I	-	-
H	-	-
G	-	-
F	-	-
E	-	-
D	-	-
C	-	-
B	-	-
A	-	-

Section cut A-A
Scale: 1:2

18

84.64

94.81

Left view
Scale: 1:10

940.37

960.71

960.71

940.37

1130

A

A

Isometric view
Scale: 1:10

Front view
Scale: 1:10

18

84

1130

DASSAULT SYSTEMES

DRAWING NUMBER
Frame2

SIZE	SCALE	WEIGHT (kg)	SHEET
A3	1:10	0,00	1/1

I	–
H	–
G	–
F	–
E	–
D	–
C	–
B	–
A	–

Isometric view
Scale: 1:10

Front view
Scale: 1:10

40

772

Right view
Scale: 1:10

78

772

170

616

616

78

125

772

78

Φ10

85

I	–	–
H	–	–
G	–	–
F	–	–
E	–	–
D	–	–
C	–	–
B	–	–
A	–	–

Isometric view
Scale: 1:5

Bottom view
Scale: 1:5

520

75

75

Front view
Scale: 1:5

520

18

DASSAULT SYSTEMES

Rib1

SHEET 1/1

DESIGNED BY:
Jerke Eisma Administ
DATE: 5-10-2011
CHECKED BY: XXX
DATE: XXX

DRAWING NUMBER

SIZE A3

SCALE 1:5

WEIGHT (kg) 0,70

This drawing is our property; it can't be reproduced or communicated without our written agreement.

I	–	–
H	–	–
G	–	–
F	–	–
E	–	–
D	–	–
C	–	–
B	–	–
A	–	–

Isometric view
Scale: 1:5

Bottom view
Scale: 1:5

802

75

Front view
Scale: 1:5

802

18

87

DESIGNED BY:
Jerke Eisma Administ
DATE: 5-10-2011

CHECKED BY: XXX
DATE: XXX

DASSAULT SYSTEMES

DRAWING NUMBER
Rib2

SIZE A3

SCALE 1:5

WEIGHT (kg) 1,08

SHEET 1/1

I	–	–
H	–	–
G	–	–
F	–	–
E	–	–
D	–	–
C	–	–
B	–	–
A	–	–

Isometric view
Scale: 1:10

Left view
Scale: 1:10

Bottom view
Scale: 1:10

45°

9

400

612

600

Front view
Scale: 1:10

Right view
Scale: 1:10

88

DASSAULT SYSTEMES

Plate test section

DRAWING NUMBER
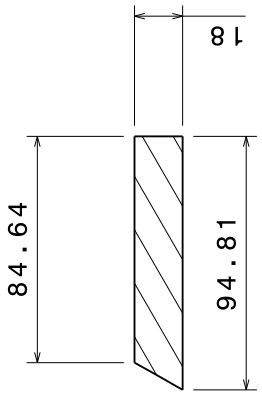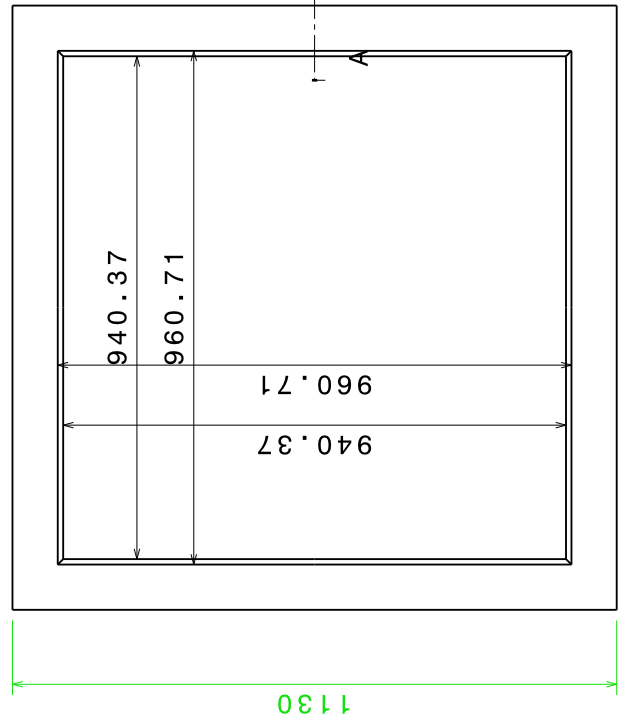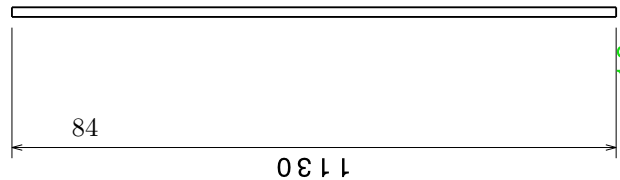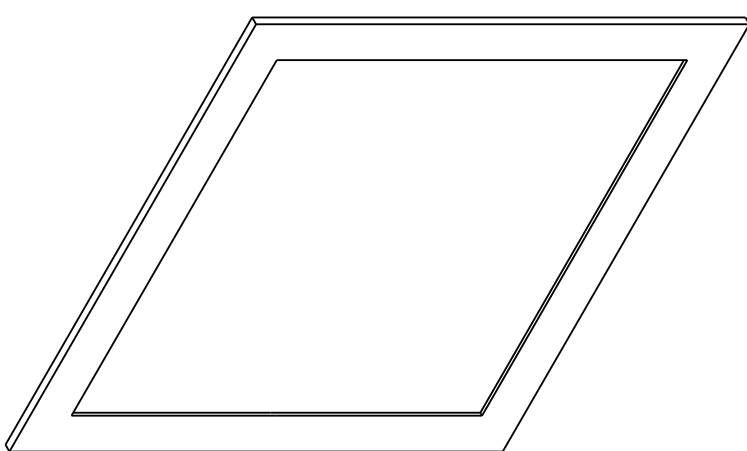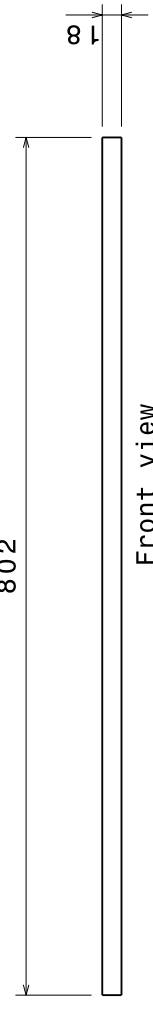
DESIGNED BY:
Jerke Eisma Administ
DATE: 4-10-2011

CHECKED BY: XXX
DATE: XXX

SIZE
A3

WEIGHT (kg)

SCALE
1:10 0,80

SHEET
1/1

I	–
H	–
G	–
F	–
E	–
D	–
C	–
B	–
A	–

Isometric view
Scale: 1:10

Front view
Scale: 1:10

600

1465.66

89

1150

DASSAULT SYSTEMES

ContractionThick

DRAWING NUMBER

SHEET 1/1

DESIGNED BY:
Jerke Eisma Administ
DATE: 5-10-2011

CHECKED BY:
DATE:

XXX
XXX

WEIGHT (kg)

SIZE A3

SCALE 1:10 50,08

I	–
H	–
G	–
F	–
E	–
D	–
C	–
B	–
A	–

Wing deformations for flapping DelFly
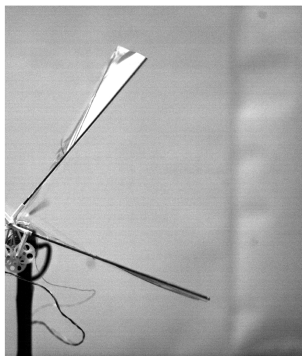
(a) $\tau = 0.17$
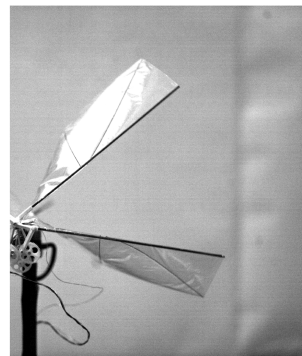
(b) $\tau = 0.26$
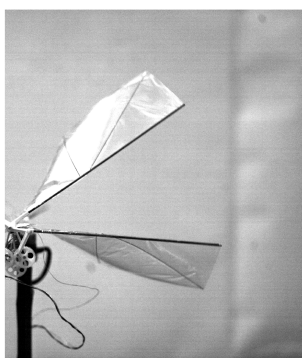
(c) $\tau = 0.31$
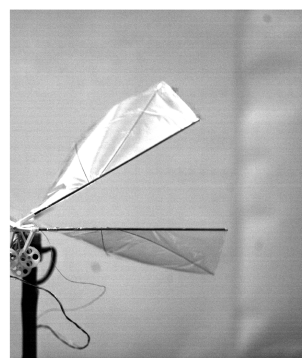
(d) $\tau = 0.33$

Figure D.1 – *Impression of the wing deformation of the DelFly put in front of a high speed camera at different time instances in the flap cycle.*
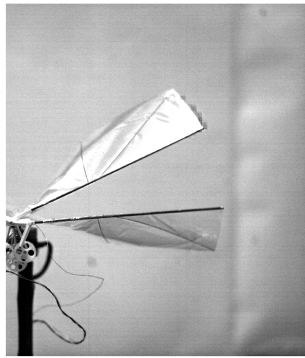
(a) $\tau = 0.37$
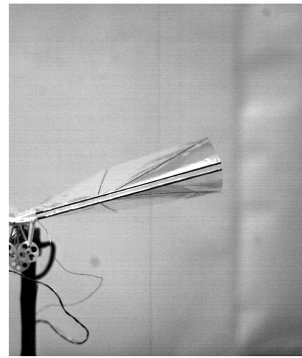
(b) $\tau = 0.50$
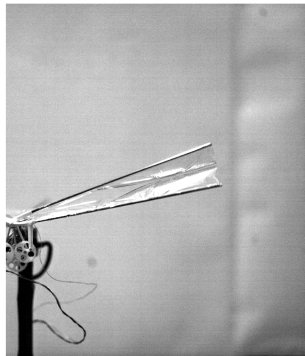
(c) $\tau = 0.63$
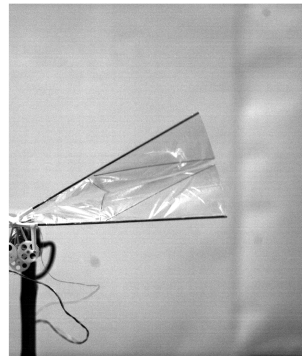
(d) $\tau = 0.72$

Figure D.2 – *Impression of the wing deformation of the DelFly put in front of a high speed camera at different time instances in the flap cycle.*
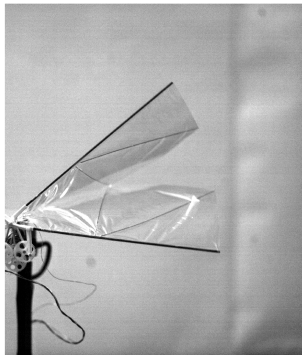
(a) $\tau = 0.80$
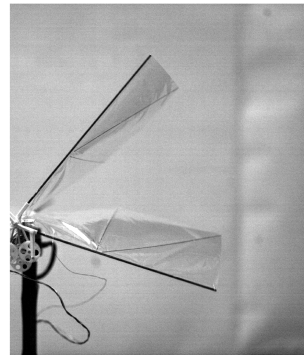
(b) $\tau = 0.86$
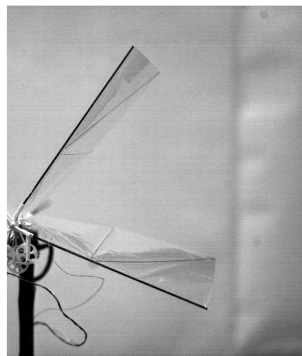
(c) $\tau = 0.92$

Figure D.3 – *Impression of the wing deformation of the DelFly put in front of a high speed camera at different time instances in the flap cycle.*